Functional MR Imaging for focal radiotherapy of prostate cancer

Greetje Groenendaal

Colophon

This text was set using the freely available LaTeX 2_ε typesetting and text formatting system.

ISBN: 978-90-393-5650-0
Print: Printsupport4u

Functional MR Imaging for focal radiotherapy of prostate cancer

Functionele MRI voor focale radiotherapie van prostaat kanker

(met een samenvatting in het Nederlands)

Proefschrift

ter verkrijging van de graad van doctor aan de
Universiteit Utrecht
op gezag van de rector magnificus, prof.dr. G.J. van der Zwaan,
ingevolge het besluit van het college voor promoties
in het openbaar te verdedigen
op vrijdag 18 november 2011 des middags te 2.30 uur

door
Greetje Groenendaal
geboren op 19 oktober 1981 te Son en Breugel

Promotor:	Prof.dr.ir. J.J.W. Lagendijk
Co-promotoren:	Dr. U.A. van der Heide
	Dr. M. van Vulpen

Het beschreven werk werd mede mogelijk gemaakt door een subsidie van KWF Kankerbestrijding (UU 2009-4310). Deze uitgave is tot stand gekomen met financiële steun van Philips, Elekta, Nucletron, Bayer B.V. en Röntgen Stichting Utrecht.

Contents

CHAPTER 1

Introduction

1.1 Radiotherapy for prostate cancer

The radiotherapy treatment of prostate cancer has improved substantially over the last years. First of all, the improvement of the position verification of the prostate has contributed significantly to the precision of the treatment. In the past, the bony anatomy was used to align the prostate prior to treatment. The bony anatomy appeared not representative for the position of the prostate. Therefore, fiducial markers are now commonly used as a surrogate for the prostate. In this way both the inter- and intrafraction motion can be identified and corrected for [1, 2, 3, 4, 5]. The introduction of intensity modulated radiation therapy (IMRT) is considered another important development [6, 7]. Using this technique, small radiation beams are combined to create complex dose distributions that fit the shape of the target. The combination of IMRT and fiducial markers enables dose escalation in the prostate, while limiting the dose to the surrounding healthy tissue. In this way an increase in treatment-related toxicity and a clinically relevant deterioration in quality of life can be avoided [8, 9].

Nevertheless, while the treatment of prostate cancer has improved, there are still patients dying from the disease (2421 patients in the Netherlands in 2008 [10]). In the current radiotherapy practice, the whole prostate is treated with a homogeneous dose, even though the prostate only partly contains tumor tissue. In other types of cancer, usually a distinction is made between gross tumor volume (GTV) and the microscopic spread of the disease. A margin around the GTV is used to include the microscopic spread, which is invisible using clinical imaging. The GTV plus margin is called the clinical target volume (CTV). Since the delineation of tumors inside the prostate has long been impossible, in the standard treatment no distinction is made based on different prostate (tumor) characteristics.

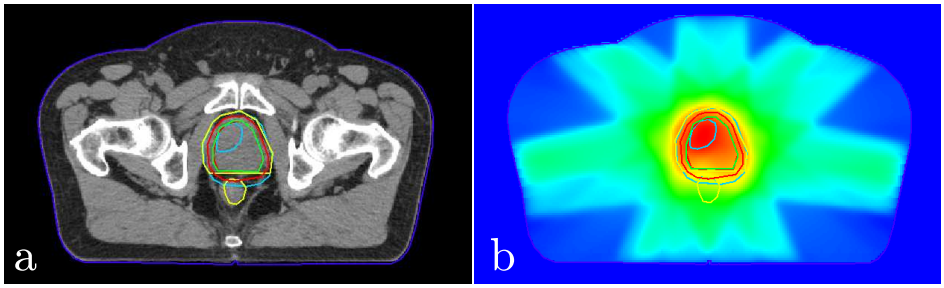

Figure 1.1: Patient example a. Planning CT scan b. Dose plan with 95 Gy microboost to GTV inside the prostate

Increasing the radiation dose to the entire prostate decreases the probability of biochemical failure in prostate cancer patients [11, 12, 13, 14]. Evidence is emerging that the dose should be even further escalated, since local recurrences are mostly found at the location of the primary tumor [15, 16]. However, in particular at the dorsal side of the prostate, such a dose escalation is in conflict with the constraints required to limit rectum toxicity. For this reason, several groups proposed to limit the boost of the radiation dose to the visible dominant lesion inside the prostate (focal boost strategies) [17, 18].

1.2 Functional MRI techniques for prostate tumor delineation

While it is at present well possible to accurately plan and deliver a focal boost to the prostate, the determination of the precise position and shape of this focal boost is much more challenging. Next to T2 weighted (T2w) imaging, the functional magnetic resonance (MR) techniques diffusion weighted imaging (DWI) and dynamic contrast-enhanced (DCE) MRI are potential candidates to guide tumor delineation in the prostate. These techniques show high sensitivities and specificities for prostate cancer detection. Sensitivity levels range from 54-84% and from 59-87% for DWI and DCE-MRI respectively. Specificity values for DWI and DCE-MRI range from 74-100% and from 74-84% [19, 20, 21, 22, 23]. DWI reflects the random translational motion of water molecules. In tumors, the increased cellularity restricts water motion in a reduced extracellular space, thus causing a reduction of the apparent diffusion coefficient (ADC).

Prior to the DCE-MRI exam, contrast agent is injected into the patient. The angiogenesis in tumors results in an increase in micro-vessel density, but also a highly disorganized capillary network. This is reflected in the different contrast uptake curves in prostate tumors and healthy tissue. These curves can be fitted with pharmacokinetic models. The most common tracer kinetic model for the prostate is the Tofts model. In this two-compartment model two parameters are estimated: K^{trans}, which is the extraction fraction of contrast agent from the blood vessels to the prostate tissue and v_{e}, which is the extracellular extravascular space. Tumor tissue is associated with elevated levels of K^{trans}. In figure 1.2 an H&E stained section of a prostate slice

is shown as well as a T2w image, ADC map and K^{trans} map of the same prostate slice. A decreased ADC and elevated K^{trans} can be appreciated at the tumor location.

1.3 Central gland and peripheral zone

Three important regions can be distinguished in the prostate based on histopathological characteristics: the peripheral zone (PZ), the transitional zone and the central zone. On MR the transitional zone cannot be distinguished from the central zone. These two zones are together considered the central gland (CG). Tumor tissue arises in ∼70% of the cases in the PZ. Prostate cancer detection and delineation is complicated by two other common pathological conditions that can arise in the prostate: prostatitis and benign prostate hyperplasia (BPH). Prostatitis is an inflammation of the prostate gland. BPH is an enlargement of the tissue surrounding the urethra. BPH is very common. Its prevalence is 50% amongst 50-year old men. This is so high, that it can almost be regarded as a normal aging process [24]. BPH is hard to distinguish from tumor tissue using DCE-MRI. This makes tumor detection in the CG more challenging compared to the PZ. Nevertheless, promising results have been published regarding tumor detection in the CG using functional MR imaging [25].

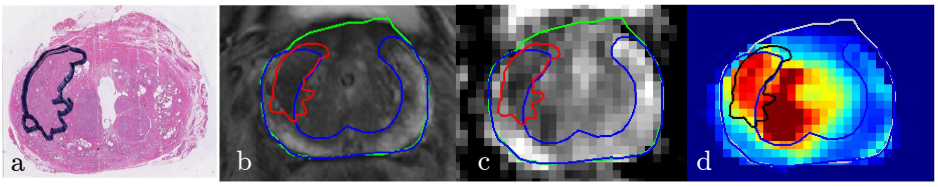

Figure 1.2: Patient example a. hematoxylin and eosin stained section with tumor delineation created by a pathologist b. T2w image. The tumor delineation is copied to the MR image (red). Furthermore, the peripheral zone is delineated (blue) c. ADC map d. K^{trans} map

1.4 Challenges for prostate tumor delineation prior to radiotherapy

The application of functional MRI techniques for tumor delineation in the prostate poses specific challenges, compared to the diagnostic setting. The question in a diagnostic setting is whether or not a patient suffers from prostate cancer. This question is already answered when a patient enters the radiotherapy department. For the planning of an additional boost dose to the dominant tumor lesion, the tumor needs to be delineated. Therefore, for each voxel inside the prostate it needs to be investigated whether or not it contains tumor tissue. This requires information on a much higher resolution compared to the diagnostic setting.

Furthermore, another difference with the diagnostic setting is that patients scheduled for radiotherapy are often treated with androgen deprivation therapy. This treatment affects the prostate (tumor) tissue. This in turn may affect the conspicuity of tumor

tissue on the MR images. For this reason in patients treated with hormonal ablation possibly a different delineation approach is required.

The goal of this thesis is to investigate how functional MR imaging techniques can be used in a radiotherapy treatment setting in order to obtain robust tumor delineations inside the prostate. Methods will be proposed on how to translate functional MR images into tumor delineations, which can serve as an input for dose planning.

1.5 Thesis outline

The reported sensitivity and specificity levels for DWI and DCE-MRI are quite high. However, there is uncertainty about the precise threshold values that distinguish tumor from healthy tissue [26, 27, 28, 19, 29, 30, 31] and therefore how these techniques should be used for tumor delineation. Furthermore, DWI is associated with cell density and DCE-MRI is believed to reflect the tissue's vasculature. It is quite possible that these properties are less strongly correlated with the presence of tumor in the tissue. High cell densities may be found outside tumor tissue, whereas parts of the tumor may have cell densities associated with healthy tissue. A similar reasoning can be given for the tissue vasculature. As a consequence, combining two imaging modalities may lead to conflicting information. This has important consequences for tumor delineation. In chapter 2, it is investigated if the two imaging modalities DWI and DCE-MRI give inconsistent information about the presence of tumor on a voxel level. Furthermore, in this chapter pragmatic approaches are given on how to deal with inconsistencies in images.

Many of the radiotherapy patients are scheduled for hormonal treatment. This treatment affects the prostate (tumor) tissue and in this way also the DCE-MRI images [32, 33]. For radiotherapy treatment planning three questions are important regarding patients using this hormonal treatment. First, does prolonged hormonal treatment affect the conspicuity of tumor tissue (tumor signal relative to background) on DWI and DCE-MRI images? Is tumor delineation possible in patients using hormonal treatment? And can we identify specific imaging thresholds for tumor delineation in patients after prolonged androgen deprivation? In chapter 3 these questions are addressed by retrospectively investigating the DWI and DCE-MRI data from patients that have undergone androgen deprivation therapy for different periods of time.

Whole-mount section histopathology is important to understand the meaning of DWI and DCE-MRI images and to validate tumor delineations created by the functional MR images. For a voxel-wise comparison between MR images and the gold standard histopathology, an accurate registration between the two is required. In chapter 4 a registration method is presented on how to compare MR images with histopathology. This method yields an average registration error between the MR images and the whole-mount histopathological data of 2-3 mm. This makes the validation of MR based tumor delineations possible.

At present, tumor delineation is a manual procedure, where a radiation oncologist and radiologist decide what to include in the target based on the available images

and clinical information. For a more widespread application, relatively simple methods to deal with this inconsistency between imaging modalities, such as presented in chapter 2, need to be improved by using automated methods to translate multiparametric data into appropriate segmentations. In chapter 5 a model is presented, which can be used to predict the presence of tumor in the PZ on a voxel level. This model is based on a radiotherapy patient group, but validated on prostatectomy patients.

The sensitivity and specificity of this model are high (chapter 5). Therefore, it has a high diagnostic value. Nevertheless, parts of the tumor are still missed using the model. The explanation for this may be found in the MR techniques underlying the model. Rather, than reflecting the presence of tumor, the MR techniques DWI and DCE-MRI are believed to reflect the tissue's cell density and microvasculature [34, 35, 36, 37, 38]. Tumor tissue can be highly heterogeneous on these characteristics, which affects the detectability [39]. In chapter 6 is investigated if the limitations in the sensitivity of the logistic regression model can be explained by heterogeneity of the tumor on a tissue level.

CHAPTER 2

Simultaneous MRI diffusion and perfusion imaging for tumor delineation in prostate cancer patients

A version of this chapter has been published as
G. Groenendaal, C.A.T. van den Berg, J.G. Korporaal, M.E.P. Philippens, P.R. Luijten, M. van Vulpen and U.A. van der Heide 2010 Simultaneous MRI diffusion and perfusion imaging for tumor delineation in prostate cancer patients *Radiotherapy and Oncology* **95** 185–190

Abstract
Background and Purpose: A study was performed to investigate if we can quantify if the two imaging modalities Diffusion Weighted Imaging (DWI) and Dynamic Contrast-Enhanced (DCE)-MRI are consistent in what voxels they determine as being suspicious of tumor tissue.
Material and Methods: Twenty-one patients with biopsy proven prostate cancer underwent a DWI and DCE-MRI scan. These scans were compared using a receiver operating curve (ROC) analysis, where either one of the two imaging modalities was thresholded and taken as a reference. The resulting area under the curve (AUC) reflects the consistency between target delineations based on the two imaging techniques. This analysis was performed for the complete prostate and the peripheral zone (PZ).
Results: Consistency between DWI and DCE-MRI parameter maps varied greatly between patients. Values of the AUC up to 0.90 were found. However, on average AUC values were 0.60. The AUC values were related to the patient's PSA and clinical stage.
Conclusions: Large variation in consistency between the two imaging modalities was found. This did not depend on the precise thresholds used. For making decisions on dose painting in the prostate, the knowledge about the inconsistency must be taken into account.

2.1 Introduction

The increase of radiation dose to the entire prostate has been shown to decrease the probability of biochemical failure in prostate cancer patients [11, 12, 13, 14]. Evidence is emerging that intraprostatic failures are mostly found at the location of the primary tumor [15, 16]. This suggests that an additional boost dose to the primary tumor may improve clinical outcome. To minimize the irradiation of healthy tissue, a focal boost to the gross tumor volume (GTV) inside the prostate has been proposed [17, 18, 40]. Such an approach requires a proper delineation of the GTV.

T2w magnetic resonance imaging (MRI) has a low specificity for tumor detection, since the signal pattern of tumor tissue is quite similar to that of benign prostatic hyperplasia (BPH), prostatitis and post-biopsy hemorrhage [23, 41, 42]. However, MRI techniques such as MR spectroscopy (MRS), Diffusion Weighted Imaging (DWI) and Dynamic Contrast-Enhanced (DCE) MRI added to T2w imaging have been shown to increase the sensitivity and specificity of the detection of prostate cancer relative to T2w imaging alone.[43, 19, 20, 21, 22, 23]. MRS has a high specificity. However, a drawback for tumor delineation is the low spatial resolution. Imaging with a higher spatial resolution is feasible with DWI and DCE-MRI.

DWI and DCE-MRI measure different properties of the underlying tissue. With DWI, the mobility of water molecules is measured. Several studies have shown that tumor tissue is associated with a reduced water diffusion [26, 27, 28, 22, 21]. This is attributed to a reduction of the extracellular volume in tumors. Sensitivity and specificity levels of 81% and 84% are reported when DWI is combined with T2w imaging [44]. Miao et al. reported an area under the ROC curve of 0.89 for DWI alone [23].

With DCE-MRI, a contrast agent is injected into the patient. The signal enhancement due to the concentration increase of contrast agent can be measured over time for each voxel in the tissue. Fitting a tracer kinetic model to the enhancement curves allows the characterization of the tissue vasculature. This technique can be used for the detection of tumors in the prostate, as tumors tend to contain a higher density of leaky blood vessels [20, 19, 45, 46]. Fütterer et al. reported sensitivity and specificity values of 87% and 87%, respectively for tumor detection using DCE-MRI [20]. Kozlowski et al. found values of 59% and 74%, respectively [30]. The latter study found for the combination of DWI and DCE-MRI a sensitivity and specificity of 87% and 74%, respectively [30], when they considered a volume to contain tumor if one of the two imaging modalities identified it as being suspicious.

Even though these reported sensitivity and specificity levels are quite high, there is uncertainty about the precise threshold values that distinguish tumor from healthy tissue [26, 27, 28, 19, 29, 30, 31]. Even within single institutes, distributions of parameter values for healthy tissue and tumor tend to be quite broad and overlapping. This may be caused by a limited measurement precision of tissue properties such as extracellular volume and microvessel permeability. Also, it is quite possible that these properties are less strongly correlated with the presence of tumor in the tissue. High cell densities might be found outside tumor tissue, whereas parts of the tumor may have cell densities associated with healthy tissue. A similar reasoning can be given

for the tissue vasculature. As a consequence, combining two imaging modalities may lead to conflicting information.

For delineation of the gross tumor volume for radiotherapy treatment planning, the problem arises how to benefit optimally from these imaging techniques. In a radiotherapy setting decisions need to be made on a voxel level. Whole-mount section histopathology is the gold standard for validation of imaging techniques. However, to address the question if DCE-MRI and DWI provide consistent information on a voxel level, validation with whole-mount section pathology is not essential. For this purpose, we adopted the Receiver Operating Curve (ROC) analysis. In this way we determine the agreement between the two imaging modalities. While this approach does not yield a validation with the ground truth of pathology, it does show if the two imaging modalities are consistent or provide complementary information.

2.2 Methods and Materials

2.2.1 Patients

Twenty-one patients (age 56-76) with biopsy proven prostate cancer, scheduled for intensity modulated radiotherapy (IMRT) were included. Patient characteristics are summarized in table 2.1. Patients receiving adjuvant hormonal therapy at the time of the MR scans, were not included. The patients were treated between March and November 2008.

2.2.2 Imaging

On all patients a DWI and DCE-MRI exam was performed using a 3T Philips Achieva MR scanner. The prostate and the peripheral zone (PZ) were delineated by a radiation oncologist using a T2w image and an SSFP balanced Turbo Field Echo (bTFE) scan. T2w images were acquired with a fast spin-echo sequence, TR/TE = 8396/120 ms, EPI-factor = 47, echo train length 13, acquisition matrix 256x256, FOV = 20 cm, slice thickness 3 mm, intersection gap 1 mm. bTFE: TR/TE = 2.85/1.43 ms, echo train length = 40, acquisition matrix 192x249, FOV = 25 cm, slice thickness = 2 mm. A 6-element phased array coil (sense cardiac) was used as receive coil during the scans.

DWI scans were performed using a multislice single shot SE-EPI sequence (FOV = 38 cm, slice thickness = 3 mm, intersection gap = 1 mm, TR/TE=5000/54 ms, acquisition matrix = 152 x 107, 9 averages, sense factor = 2 in AP direction, phase encoding direction = PA, b values = 300, 500, 1000 s/mm^2). The b value of 0 s/mm^2 was not taken into account in order to avoid sensitivity to perfusion effects [47]. The ADC maps were resampled to a resolution of 2.5x2.5x3 mm^3 to be compared with the DCE-MRI parameter maps.

The DCE-MRI protocol used consisted of a 3D spoiled gradient echo sequence (20 transverse partitions, 2.5 mm section thickness, TR/TE=4/1 ms, flip angle 8°, FOV = 40 cm, acquisition matrix = 160 x 160). Scans were repeated 120 times at 2.4s interval. A concentration of 0.1 ml/kg of Gadubutrol (1.0M)(Gadovist, Schering AG, Berlin,

Table 2.1: Patient characteristics

Patient Number	PSA [ng/ml]	Gleason grade	clinical stage	biopsy result (tumor tissue found)		Volume of MR based ROI [cc]	
				Left	Right	Left	Right
1	19.6	7	T1c	some	none	0.84	0
2	48	7	T3	some	possibly	1.21	0
3	14.3	8	T3	cells in TURP		-	-
4	9.6	6	T1c	some	some	0	0.53
5	57	7	T3	a lot	a lot	0.44	0.44
6	7.4	6	T2b	none	a lot	0	0.87
7	16	7	T2b	location unknown		-	-
8	8.4	6	T3	none	a lot	0	1.43
9	7.9	6	T1b	cells in TURP		-	-
10	34.2	7	T1a	little	none	0.55	0
11	25	7	T2a	none	some	0	1.95
12	43.5	7	T1c	little	a lot	0	2.44
13	26	6	T2	little	little	0	0.68
14	4.6	6	T3	a lot	little	0.44	0
15	30	7	T3	none	a lot	0	1.77
16	10	6	T2	a lot	a lot	0.18	0.13
17	26.4	7	T2b	some	little	0	0.64
18	13	6	T3	little	a lot	0	1.16
19	10	8	T3	some	some	20	10
20	7	7	T3	none	a lot	0	4.42
21	38.5	7	T3a	little	none	0.40	0

Germany) contrast was injected with 2 ml/s, followed by a saline flush. Gadubutrol (1.0M) has been registered in Europe for use in MR angiography, imaging of the brain and spine. Off-label use for DCE-MRI is chosen as standard practice in our clinic, because of its advantage over the use of the approved DCE-MRI contrast agents, such as Magnevist, with respect to nephrogenic systemic fibrosis (NSF). This is based on the ESUR Guideline of 17th July 2007. Other applications of gadovist in DCE-MRI are described by Pauls et al. and Palmowski et al. [48, 49]. Concentration of the contrast agent was calculated from the MR signal using preceding small flip angle scans with 3 flip angles (6°, 16° and 32°, TR/TE=50/1.1 ms) [50]. If the edges of the prostate did not match within a distance of 2.5 mm during the prescans or time series, rigid registration on the prostate was applied. This was done with a rigid image registration algorithm [51]. Before applying the tracer kinetics model, a moving average filter of 3x3 voxels in the x and y direction was used to smooth spatial fluctuations for each time point. The Arterial Input Function (AIF) was obtained for each patient from the most caudal slices to minimize inflow artifacts. We used the left artery to determine the AIF. We found consistently that due to local deviations in the B_1 field, the intended flip angle could not be reached in the artery located on the right side. The concentration of contrast agent was calculated from the relative signal enhancement. The $T_{1,0}$ of blood was set to 1660 ms and relaxivity values to $r_1 = 5/\mathrm{mM/s^{-1}}$ and $r_2 = 7.1/\mathrm{mM/s^{-1}}$ [52].

Then, for each voxel the measured concentration-time curves were analyzed with the Generalized Kinetic Model [53], using the linear least-squares method published by Murase [54]. This yielded 3D maps of the volume transfer constant K^{trans}. The voxels of the K^{trans} maps were resampled to be compared to the ADC maps to a size of 2.5x2.5x3 mm^3. However, due to use of a moving average kernel in each single voxel also the information of the eight neighboring voxels was represented.

2.2.3 Analysis

The purpose of this study was to quantify if DWI and DCE-MRI provide consistent information about the delineation of a target. A simple approach would be to define regions as suspect based on thresholding. However, there is uncertainty about the precise threshold values that distinguish tumor from healthy tissue. A calculation of the consistency of two imaging modalities might therefore be biased by the specific thresholds applied.

For this reason, we have carried out the analysis of the consistency of DWI and DCE-MRI for a wide range of possible threshold values. We adopted the ROC analysis, used regularly to compare the diagnostic value of an imaging modality with a gold standard such as histopathology. Here, we used the ROC analysis to compare one imaging modality with the other. A reference map was generated that identified a voxel as target for irradiation if its ADC was below a given threshold and as healthy otherwise. Similarly, a mask is generated from the corresponding K^{trans} map that identifies if a voxel lies above a given threshold. In a voxelwise comparison, the agreement between the K^{trans} mask and the reference target map was determined, from which a sensitivity and specificity was calculated. This is illustrated in figure 2.1. By repeating

this procedure for a range of threshold levels between 0 and 2 min^{-1} for K^{trans} a ROC curve was obtained and an area under the curve (AUC) was calculated. A high AUC indicates that the K^{trans} image is consistent with the ADC reference map. This procedure was repeated for three reference maps based on different values for the ADC threshold. Similarly, the AUC was calculated using the K^{trans} map as a basis for a reference map and varying the ADC thresholds in a range between 0 and $10{\cdot}10^{-3}$ mm^2/s. Here, also three reference maps were used, based on three values for the K^{trans} threshold. For each patient, this analysis was performed on the entire prostate and on the PZ separately, to avoid the influence of benign prostatic hyperplasia (BPH) that is frequently present in the central gland.

While the precise threshold values used for the reference maps are not critical in this approach, it makes sense to choose values that are reasonable. In order to establish a reasonable range of threshold values, a radiation oncologist (MvV) with over three years experience in delineating prostate tumors, identified regions which were suspected matching all following criteria a hypo-intense T2, a low value of the ADC and a high value of K^{trans}, the rectal exam and the location of positive biopsy results. In 18 prostates at least one suspicious region was delineated. The side of the delineated region was always consistent with the reported tumor side in the pathology report (table 2.1). From three patients no information about the tumor location could be obtained from the biopsy results. In these patients, no suspicious regions were delineated. The volume of the regions of interest are listed in 2.1. Similarly, we identified regions that were considered healthy.

2.3 Results

Figure 2.2 shows a T2w image, a K^{trans} map and an ADC map. On the left side of the PZ a hypointense signal is found on the T2w image and the ADC map. Also, an elevated K^{trans} can be seen on this location. All three imaging modalities indicate this area as suspicious for being tumor. Similarly, a region could be identified as normal tissue (not present in the slice shown in figure 2.2). For all patients, we determined for these regions of interest the average ADC and K^{trans}. The mean value for all patients and the range over the patient group is listed in table 2.2. These values were compared with literature values (table 2.2). The average parameter values found in our study fall within the ranges reported in the literature, although for the ADC our values are on the lower side of the range.

Based on our data, we defined three reference maps for both the ADC and K^{trans}, using threshold values in between the mean values for suspicious and non-suspicious regions. The following ADC and K^{trans} thresholds were chosen: $0.96{\cdot}10^{-3}$, $1.07{\cdot}10^{-3}$, $1.19{\cdot}10^{-3}$ mm^2/s and 0.65, 0.80, 0.94 min^{-1}, respectively.

These thresholds are used to threshold the ADC and K^{trans} map shown in figure 2.2. The result of thresholding on the images shown in figure 2.2b and c is shown for all nine combinations in figure 2.3. The overlap volume increases for increasing ADC thresholds and decreasing K^{trans} thresholds. However, for none of the threshold

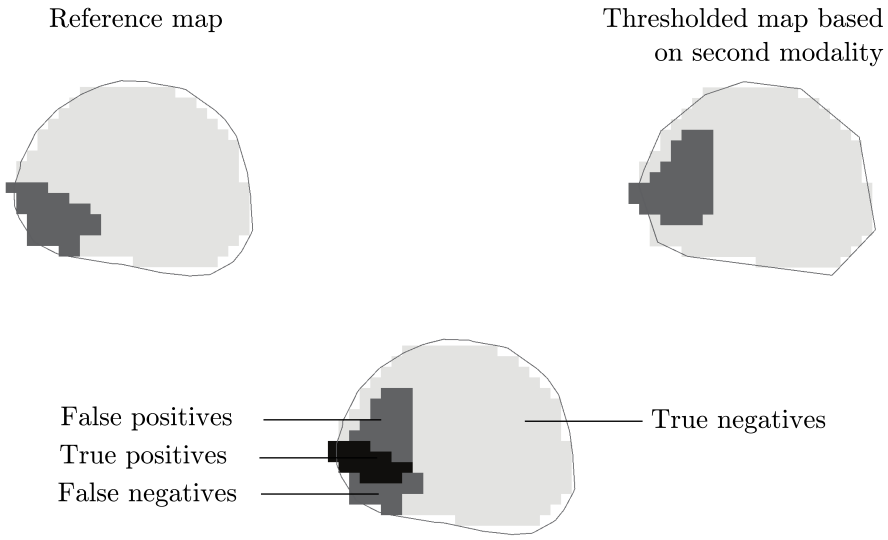

Figure 2.1: A reference map is created by thresholding one of the imaging modalities, e.g. the ADC map. Then the parameter map of the other imaging modality (e.g. the K^{trans} map) is thresholded and compared with the reference map. In this way sensitivity and specificity values can be calculated. By varying the thresholds of the second imaging modality (the K^{trans} map), an ROC curve can be obtained.

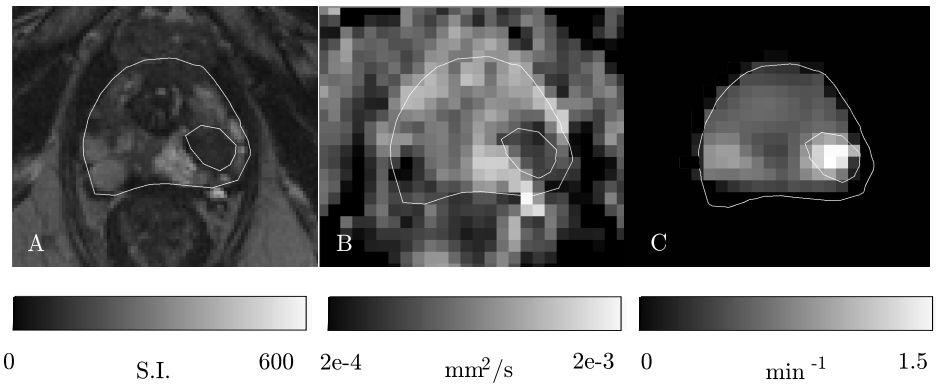

Figure 2.2: a.T2w image b. ADC map c. K^{trans} map of the same patient

Table 2.2: ADC and K^{trans} values found in suspicious and non suspicious regions compared with literature values.

	suspicious	**non suspicious**
ADC [mm^2/s]		
Hosseindzadeh et al. [21]	$1.27 \pm 0.37{\cdot}10^{-3}$	$1.34 \pm 0.38{\cdot}10^{-3}$
Sato et al. [22]	$1.11 \pm 0.41{\cdot}10^{-3}$	$1.68 \pm 0.4{\cdot}10^{-3}$
Pickles et al. [26]	$1.38 \pm 0.38{\cdot}10^{-3}$	$1.95 \pm 0.5{\cdot}10^{-3}$
This study	$0.9{\cdot}10^{-3}$ ($0.5{\cdot}10^{-3}$ - $1.3{\cdot}10^{-3}$)	$1.3{\cdot}10^{-3}$ ($0.9{\cdot}10^{-3}$ - $1.7{\cdot}10^{-3}$)
K^{trans} **[min^{-1}]**		
Van Dorsten et al. [19]	0.59 ± 0.31	0.34 ± 0.17
Ocak et al. [31]	0.47 ± 0.57	0.23 ± 0.25
Kozlowski et al. [30]	1.26 ± 0.54	0.60 ± 0.56
This study	1.09 (0.46 - 1.97)	0.50 (0.2 - 0.82)

combinations we found complete overlap between thresholded ADC and thresholded K^{trans} regions.

To quantify the correspondence between target delineations based on the three ADC thresholds and the K^{trans} threshold over a range from 0 to 2 min^{-1} we used the ROC analysis. Similarly, we compared the delineations based on the three K^{trans} thresholds with the ADC threshold over a range from 0 to $10{\cdot}10^{-3}$ mm^2/s. For the patient shown in figures 2.2 and 2.3, the ROC curves for the entire prostate are shown in figure 5.2. The area under the curve (AUC) values for ADC images thresholded at $0.96{\cdot}10^{-3}$, $1.07{\cdot}10^{-3}$ and $1.19{\cdot}10^{-3}$ mm^2/s were respectively 0.62, 0.63 and 0.65. For the thresholded K^{trans} images we found AUC values of 0.65, 0.67 and 0.67, when thresholded at 0.65, 0.80 and 0.94 min^{-1}, respectively. The results of all the patients are listed in table 2.3. In this table the mean AUC and ranges of the entire group of patients is given for both the complete prostate as well as for the PZ only. In some patients no voxels existed where the K^{trans} values were higher than 0.80 and 0.94 min^{-1}. The number of patients that did have voxels with K^{trans} up to these values, is given in table 2.3.

On average, the mean AUC values are classified as intermediate, although AUC values up to 0.90 are found for individual patients. This spread in AUC values is highlighted in figure 2.5. In this example, which is created with a K^{trans} reference map, thresholded at 0.94 min^{-1}, can be seen that for these settings AUC values vary between 0.44 and 0.90. We performed a multivariate regression analysis to investigate if the AUC values found are related to PSA, clinical stage and Gleason grade. We found that the maximum AUC increases with clinical stage and PSA. The AUC values in T2 and T3 patients are on average respectively 0.09 and 0.15 higher than in T1 patients. The maximum AUC values increase on average 0.03 per 10 ng/ml PSA. The effect of Gleason grade on the maximum AUC appeared not to be significant.

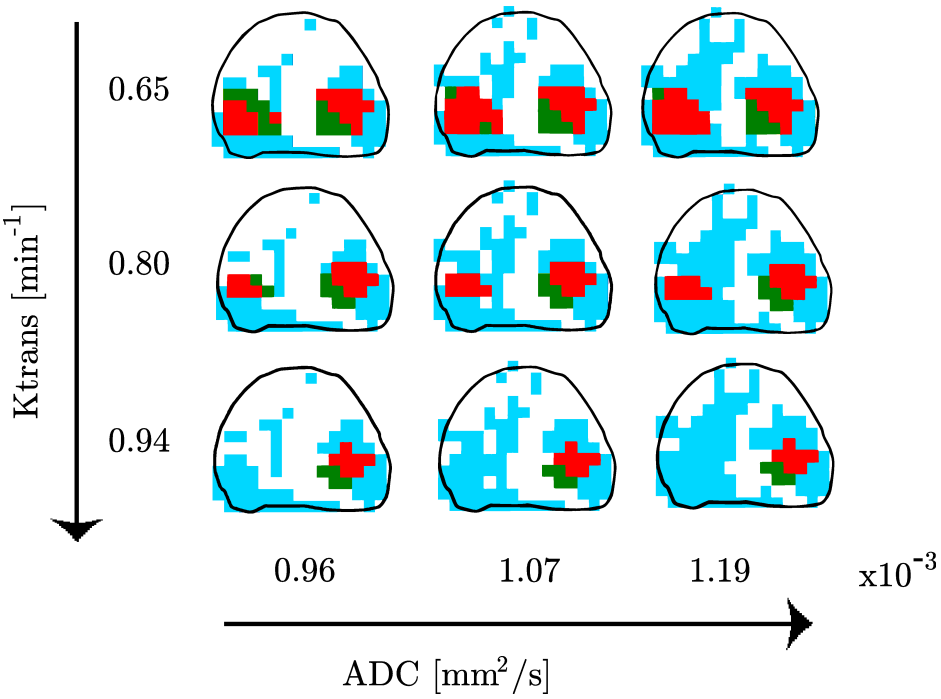

Figure 2.3: The thresholded ADC (blue), the thresholded K^{trans} (green) and the overlap (red) of the thresholded regions for 9 different threshold combinations

2.4 Discussion

MRI techniques such as DWI and DCE-MRI can play an important role in the delineation of gross tumor volume in the prostate for radiotherapy treatment planning. The sensitivity and specificity of these techniques for diagnosing prostate cancer is high [44, 23, 20, 30]. However, data about the sensitivity and specificity of small voxels are not available. This poses a problem for GTV delineation, since delineation implies that for each voxel the decision is made if it is part of the target volume or not. In this study, we investigated if two commonly used MRI techniques, DWI and DCE-MRI, provide consistent information about the presence of tumor in a voxel in patients scheduled for radiotherapy.

The ADC values we found in our study were on the lower side of the range found in the literature. In many studies a b value of 0 s/mm^2 is taken into account for calculating the ADC [21, 22, 26]. The increased sensitivity to perfusion effects in these cases will lead to a higher ADC value. Another explanation for the difference in ADC values between this study and the values found in table 2.2 is that b values depend on both the duration of the diffusion gradients (δ) and the time in between the diffusion gradients ($\triangle$). Differences in choices for these parameters might influence the ADC value [55]. Although the differences in scan procedures might influence the

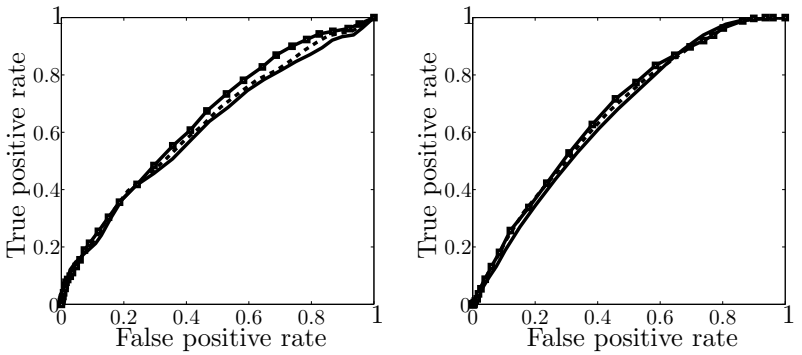

Figure 2.4: ROC curves of the prostate with ADC map (left) and K^{trans} map (right) taken as reference. In the left image the following thresholds have been used to create the reference targets maps: $0.96{\cdot}10^{-3}$ (solid line), $1.07{\cdot}10^{-3}$ (dashed line), $1.19{\cdot}10^{-3}$ mm^2/s (line with squares). For the right image these thresholds were: 0.65 (solid line), 0.80 (dashed line) and 0.94 (line with squares) min^{-1}.

ADC and K^{trans} map in a quantitative way, due to the large range of threshold values investigated we do not expect that this influences the result of this study.

Although the sensitivity of tumor detection is large for DWI and DCE-MRI, in some patients the overlap was limited (figure 2.3). On the other hand, we found in three patients for at least one reference target map an AUC larger than 0.8. This is an indication of a good consistency between the two techniques about the location and extent of the suspicious tissue. In patients where we found a low consistency between the ADC and K^{trans} maps, we have to examine what the cause was of this low consistency. A limitation of this study is the lack of histopathological reference. Therefore, we do not know the cause of the low consistency found in some regions.

First, it could be the result of artifacts, e.g. motion or EPI artifacts, especially in the presence of air cavities. The magnitude of EPI artifacts can be estimated by the acquisition of a B_0 map. We did this for 3 patients and found that in 90% of all voxels the displacement was less than 2.4 mm. In the regions suspected of containing tumor tissue the deformations remained below 2.4 mm. This was consistent with the observation that for 20 out of 21 patients the edges of the prostate on a DWI were shifted less than a single voxel (2.5 mm) with respect to the T2w image. In one patient a shift of about 2 voxels was found in some slices, due to rectal motion.

Secondly, it is quite possible that the characteristics which were probed by DWI and DCE-MRI do not co-localize well in all patients. ADC essentially reflects the density of cells and the extra-cellular extra-vascular space, whereas K^{trans} reflects the micro-vessel density and permeability of the vasculature. Both these properties are associated with the presence of tumor, but the correlation may be less than perfect. Langer et al. found higher ADC values in 'sparse' than in 'dense' tumors [39]. This

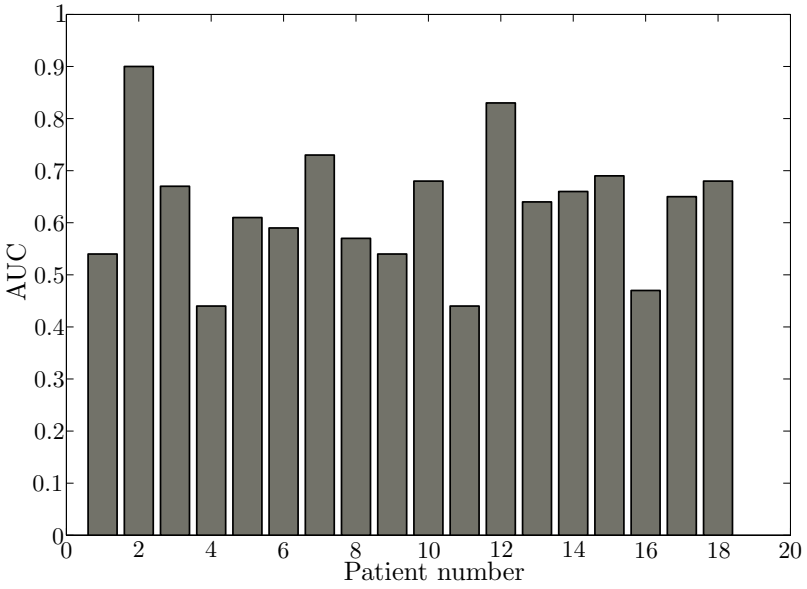

Figure 2.5: AUC values from all patients. As a reference map the K^{trans} map in the PZ is used. This map was thresholded at 0.32 min^{-1}.

could be an explanation for the sometimes low consistency between ADC and K^{trans} maps.

A detailed answer to the cause of the limited consistency in target volumes derived from the two techniques can only be provided by whole-mount histopathology, as this is the gold standard for validation of these imaging techniques. However, it is important to realize that for this purpose, the validation must be done on a voxel level. The process of correlating hematoxylin-eosin stained sections with MR images requires a highly accurate registration between the two. Because this is problematic, commonly, larger regions in the prostate are correlated with histopathology [20, 19, 30]. While some recent studies showed that registrations on a higher resolution were feasible, it is not clear if this is sufficient to warrant a voxelwise validation of the images [56]. The second problem lies in the difference in patient characteristics of patients scheduled for prostatectomy and external-beam radiotherapy. Generally, patients with T3 stage prostate cancer do not qualify for prostatectomy. Thus, data obtained from whole-mount section validation, will be biased towards the lower stages.

We have to find an approach how to deal with this for delineating the GTV. In patients where the two imaging modalities give consistent information, the delineation of a target can be straightforward: there is a high probability that regions identified by both modalities contain tumor tissue. When the two imaging modalities give inconsistent information, the probability that tumor is present is smaller. A practical approach could be to treat the voxels on which the two modalities agree as the GTV.

Table 2.3: mean AUC values of ROC analysis.

Reference modality	Threshold used to define suspicious region	AUC prostate	AUC PZ
ADC	$0.96{\cdot}10^{-3}$	**0.58** (0.31 - 0.79)	**0.60** (0.46 - 0.79)
ADC	$1.07{\cdot}10^{-3}$	**0.58** (0.35 - 0.75)	**0.60** (0.46 - 0.79)
ADC	$1.19{\cdot}10^{-3}$	**0.59** (0.39 - 0.75)	**0.61** (0.49 - 0.81)
K^{trans}	0.65	**0.60** (0.38 - 0.82)	**0.62** (0.52 - 0.82)
K^{trans} (n=19)	0.80	**0.60** (0.35 - 0.88)	**0.63** (0.49 - 0.90)
K^{trans} (n=18)	0.94	**0.60** (0.35 - 0.88)	**0.63** (0.44 - 0.90)

AUC values are the mean values over all patients

In case only one of the two modalities indicates a voxel as suspicious, the region could be considered a 'high-risk CTV'. One could choose not to boost these regions, but in any case safe margins should be applied around these regions.

This approach can already be used to date. However in the longer term, we might go a step further. Instead of looking in a binary way to the tissue as either being healthy or tumor, it is also possible to consider it as a continuum from healthy tissue to poorly differentiated tumor tissue. This will change the decision from to boost a certain volume or not, to a dose-painting by numbers approach [57]. In this way voxels with a lower ADC and a higher K^{trans} would receive a higher radiation dose. Since a significant negative correlation exists between ADC and cell density [36], one could speculate that regions with lower ADC values need a higher radiation dose to kill all tumor cells. K^{trans} is expected to be associated with microvessel density. In turn, microvessel density appears to be a prognostic factor in many cancers. This property is associated with tumor growth and metastases [58]. Future research should focus on how ADC and K^{trans} correlate with tumor aggressiveness in the prostate and what dose is necessary to control different types of tumors.

In conclusion, in a group of 21 patients we quantified if DWI and DCE-MRI provide consistent information about the delineation of the tumor inside the prostate. We found a large variation between patients. Some patients showed a good consistency between the two imaging modalities, whereas others showed poor overlap between regions identified as suspicious. The result did not depend on the precise thresholds used. For making decisions on dose painting in the prostate, the knowledge about the inconsistency must be taken into account.

CHAPTER 3

The effect of hormonal treatment on conspicuity of prostate cancer: Implications for focal boosting radiotherapy

This chapter has been submitted as
G. Groenendaal, M. van Vulpen, S.R. Pereboom, D. Poelma-Tap, J.G. Korporaal, E. Monninkhof and U.A van der Heide 2010 The effect of hormonal treatment on conspicuity of prostate cancer: Implications for focal boosting radiotherapy

Abstract
Background and purpose: For focal boosting of prostate tumors, three questions are important regarding the use of hormonal therapy. Does prolonged hormonal treatment affect the conspicuity of tumor tissue on DWI and DCE-MRI images? Is tumor delineation possible in patients using hormonal treatment? Can we identify specific imaging thresholds for tumor delineation in patients after prolonged androgen deprivation?
Materials and methods: 96 patients were included. Using multivariate linear regression analyses, we investigated if DWI and DCE-MRI parameter maps are different in patients using the hormonal treatment 0-3 or >3 months. Furthermore, logistic regression was performed to obtain specific imaging thresholds for tumor tissue for the two patient groups.
Results: Tumor tissue in the >3 months hormonal treatment group showed a significant higher diffusion and lower perfusion compared to the 0-3 group. This resulted in lower tumor conspicuity. Nevertheless, in 18/21 of the patients in the >3 months treatment group, a suspicious lesion could be defined based on the MR images. Based on logistic regression, different imaging thresholds should be set for tumor detection in the two treatment groups.
Conclusions: Prolonged androgen deprivation decreases tumor conspicuity. Different imaging thresholds need to be set to delineate tumor in patients who have used prolonged hormonal treatment.

3.1 Introduction

As evidence is emerging that local recurrences of prostate tumors are often seen at the original tumor location [15, 16], an additional boost dose to this tumor could improve the tumor control probability. By limiting the boost to the visible tumor, the toxicity to the organs at risk may be kept at a minimal level [17, 18, 40, 59].

Magnetic resonance imaging (MRI) techniques such as diffusion weighted imaging (DWI) and dynamic contrast enhanced (DCE) MRI have a high sensitivity and specificity for tumor detection inside the prostate [26, 27, 28, 22, 21]. Therefore, potentially they are good candidates to guide tumor delineation in the prostate [60]. However, the range of values of the functional parameters derived from DWI and DCE-MRI is quite large and overlaps partly for tumor and healthy tissue. In an earlier study, we addressed the problem of how to deal with conflicting information from DWI and DCE-MRI [61]. Also, approaches were proposed to deal with uncertainties within the parameter maps [62]. A more robust approach to tumor delineation would use thresholds for the functional parameter maps. However, the large range of values observed, results in a gradual change in tumor probability, rather than a sharp threshold. Understanding the causes of the variation in parameter values, we may refine this approach and develop threshold values for specific groups of patients.

Hormonal withdrawal is one of the factors influencing prostate tumor tissue. Previous studies have shown that these changes affect the parameters measured with DCE-MRI [32, 33]. Furthermore, androgen withdrawal triggers the apoptotic pathway in androgen-dependent prostate cancer cells [63]. Since, the apparent diffusion coefficient (ADC) measured with DWI is correlated with cell density [34, 35, 36], we must take into consideration that androgen deprivation also affects the ADC.

For radiotherapy treatment planning three questions are important regarding patients using this hormonal treatment. First, does prolonged hormonal treatment affect the conspicuity of tumor tissue (tumor signal relative to background) on DWI and DCE-MRI images? Is tumor delineation possible in patients using hormonal treatment? And can we identify specific imaging thresholds for tumor delineation in patients after prolonged androgen deprivation? In this study we address these questions by retrospectively investigating the DWI and DCE-MRI data from patients that have undergone androgen deprivation therapy for different periods of time.

3.2 Methods and Materials

3.2.1 Patients

96 patients with biopsy proven prostate cancer, scheduled for intensity-modulated radiotherapy (IMRT) and 125-I brachytherapy were included. Patient characteristics are summarized in table 3.1. All patients were treated between January 2008 and July 2010 and were candidates for hormonal treatment. However, the periods of treatment time at the time of the MR exam differed between patients. The patients were divided in two groups based on the duration of the hormonal treatment: 0-3 months and >3 months. Patients scheduled for brachytherapy are treated with hormonal therapy,

Table 3.1: Patient characteristics at time of MR scans

	Number of patients 0-3 months hormonal therapy	>3 months hormonal therapy
Total	75	21
Primary tumor stage		
Tx	1 (1%)	0 (0%)
T1	6 (8%)	5 (24%)
T2	12 (16%)	6 (29%)
T3	54 (72%)	10 (48%)
T4	2 (3%)	0 (0%)
Gleason score		
5	1 (1%)	0 (0%)
6	5 (7%)	9 (43%)
7	23 (31%)	6 (29%)
8	33 (44%)	3 (14%)
9	11 (15%)	2 (10%)
10	2 (3%)	1 (5%)
PSA level [ng/ml]	15.1 (3.3-77)	11.4 (3.5-50)
Age [years]	68 (47-83)	69 (60-79)
IMRT	68 (91%)	9 (43%)
125-I	7 (9%)	12 (57%)

when the prostate is considered too large for proper dose coverage with the 125-I seeds. In IMRT patients hormonal treatment is prescribed to improve treatment outcome [64]. The distribution of brachytherapy and IMRT patients over the two groups is shown in table 3.1.

3.2.2 Imaging

On all patients a T2 weighted (T2w), balanced TFE, DWI and DCE-MRI exam were performed using a 3T Philips Achieva MR scanner. A 6-element phased array coil (sense cardiac) was used as receive coil during the scans. T2w images were acquired with a fast spin-echo sequence, TR/TE = 8396/120 ms, echo train length 13, acquisition matrix 256x256, FOV = 20 cm, slice thickness 3 mm, intersection gap 1 mm. balanced TFE: TR/TE = 2.85/1.43 ms, echo train length = 40, acquisition matrix 192x249, FOV = 25 cm, slice thickness = 2 mm.

DWI scans were performed using a multislice single shot SE-EPI sequence (FOV = 38 cm, slice thickness = 3 mm, EPI-factor = 47, intersection gap = 1 mm, TR/TE=5000/54 ms, acquisition matrix = 152 x 107, 9 averages, sense factor = 2 in AP direction, phase encoding direction = PA). b values 300, 500 and 1000 s/mm^2 were used to calculate the apparent diffusion coefficient (ADC).

The DCE-MRI protocol used consisted of a 3D spoiled gradient echo sequence (20 transverse partitions, 2.5 mm section thickness, TR/TE=4/1 ms, flip angle 8°, FOV = 40 cm, acquisition matrix = 160 x 160). Scans were repeated 120 times at 2.4s interval. A concentration of 0.1 ml/kg of Gadubutrol (1.0M)(Gadovist, Schering AG, Berlin, Germany) contrast was injected with 2 ml/s, followed by a saline flush. The tracer kinetics data was analyzed as described in [60]. Due to the extent of the measurement errors on the patient specific input functions, a generic arterial input function (AIF) was used for all patients.

3.2.3 Analysis

In all patients the prostate and the peripheral zone (PZ) were delineated using the T2w image and bTFE scan. The PZ was analyzed separately to be insensitive to BPH. To quantitatively study the effect of androgen deprivation on MR parameter values inside the tumor we calculated for each patient the lowest mean ADC and the highest mean K^{trans} in a 5x5x5 mm^3 kernel inside both the prostate and PZ. These values were assumed to be representative for ADC and K^{trans} values in tumor tissue. At the same time the median ADC and the median K^{trans} inside the prostate and PZ were assumed to be representative for healthy tissue (figure 3.1).

We used linear regression analysis to study the effect of the duration of the hormonal treatment prior to the MR scan on the lowest mean ADC, highest mean K^{trans} and median ADC and K^{trans} values. IMRT and 125-I brachytherapy patients are scheduled for hormonal treatment for different reasons. Since IMRT and I-125 brachytherapy patients are not equally distributed in the two hormonal treatment groups, the two groups may not be comparable. For this reason we adjusted for the effect of potential confounding factors. The following factors, which might be associated with both the duration of the hormonal treatment and the MR parameters, were considered as confounders: patient age, PSA, Gleason score (GS) (in three categories: GS<7, GS=7, GS>7), T stage (in three categories T stage<2, T stage=2, T stage >2), size of prostate and PZ.

First, we assessed the crude relation between the duration of hormonal treatment and MR parameters. Second, we added all potential confounders and removed them singly using manual backwards elimination. A factor was considered as a relevant confounder when it changed the regression coefficient by more than 10%.

To identify if we can develop threshold values for specific groups of patients, we fitted a logistic regression model through our ADC and K^{trans} data for both the 0-3 months and >3 months hormonal treatment group. To this end we assumed that the lowest mean ADC and highest mean K^{trans} values in a 5x5x5 mm^3 adjacent kernel are representative for tumor values, whereas median ADC and K^{trans} values are representative for values in healthy tissue. Similar as done by Korporaal et al. [62] we looked for thresholds for the ADC and K^{trans} for which a tumor probability of 95% was predicted according to the logistic regression model. Voxels inside the prostate exceeding this threshold could be considered as gross tumor volume [62]. Threshold values were established for both the 0-3 months and >3 months hormonal treatment group.

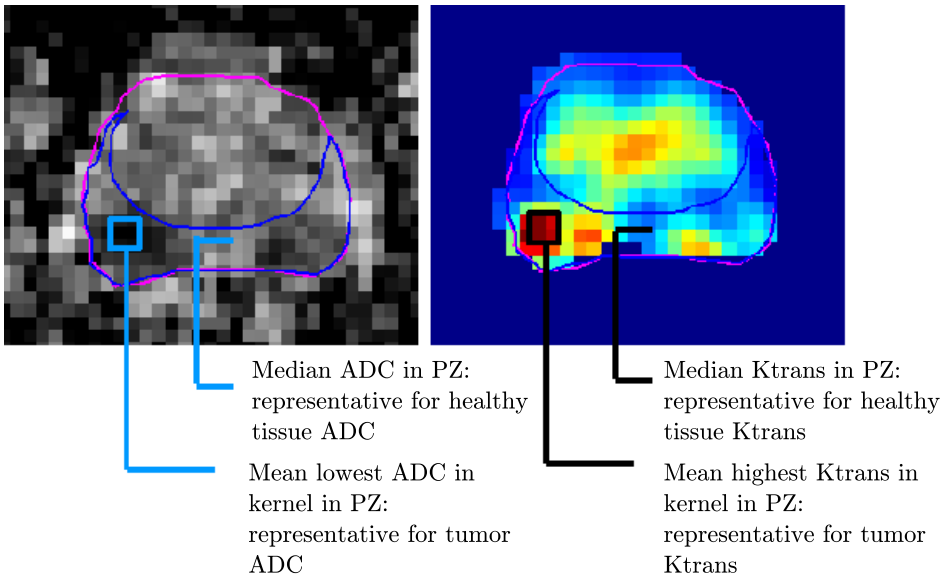

Figure 3.1: To be insensitive to interobserver variations, in this paper, we assumed that median values of ADC and K^{trans} inside the prostate and PZ are representative for healthy tissue. The lowest mean ADC and highest mean K^{trans} in a 5x5x5 mm^3 kernel were assumed to be representative for tumor tissue.

For statistical analyses we used SPSS 16.0.

3.3 Results

The duration of hormonal treatment was correlated with both the mean lowest ADC and mean highest K^{trans} (Pearson correlation = 0.32 and -0.35 respectively, with p values 0.002 and 0.001). Increasing ADC values and decreasing K^{trans} values were found for increasing treatment times. Nevertheless, a large spread in the data can be appreciated (figure 3.2(a) and 3.2(b)).

The mean lowest ADC and mean highest K^{trans} values for the different hormonal treatment duration periods as well as the regression coefficients (β) and the corresponding p values are given in table 3.2. In assessing the relation between the functional MR values between the two hormonal therapy groups, GS>7 was identified as a confounding factor in the relation between duration of hormonal treatment and the mean lowest ADC values. GS>7 was associated with lower values of tumor ADC. The difference in mean lowest ADC values between the two hormonal treatment groups can be partly described by GS. By taking the effect of GS into account we found slightly smaller associations between duration of hormonal treatment and mean lowest ADC values (table 3.2).

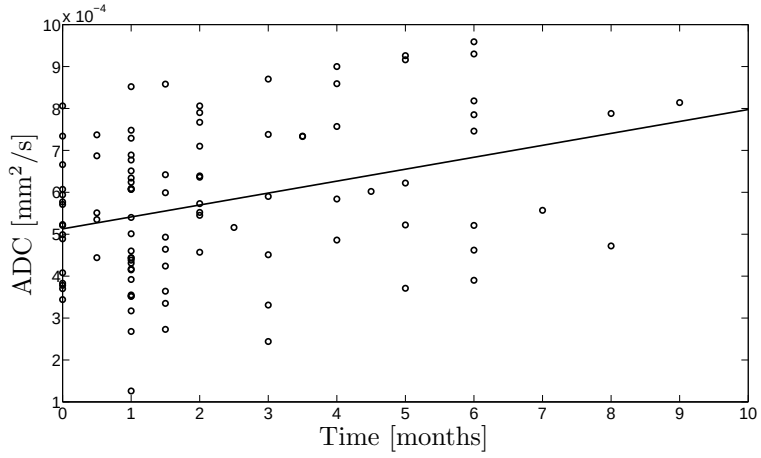

(a)

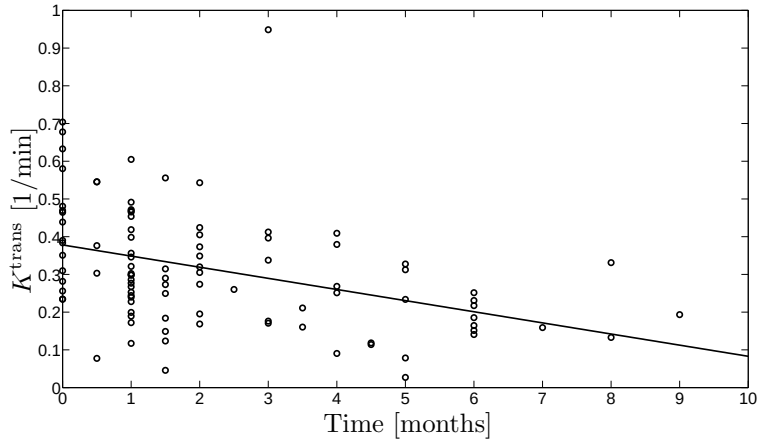

(b)

Figure 3.2: The effect of the duration of hormonal therapy at the time of the MR scan on the mean lowest ADC and mean highest K^{trans}. Pearson correlation was 0.32 for the relation between hormonal treatment time and ADC and -0.35 for the relation between hormonal treatment time and K^{trans}, with p values 0.002 and 0.001

No confounding factors could be identified for the relation between the duration of hormonal treatment and the K^{trans} values.

A significant difference was found between the mean lowest ADC and the mean highest K^{trans} between the 0-3 months and >3 months hormonal therapy groups. In the total prostate the mean lowest ADC is on average $1.2{\cdot}10^{-4}$ mm^2/s higher and the mean highest K^{trans} 0.14 min^{-1} lower in the >3 months treatment group. At the same time, the median ADC, assumed to be representative for healthy tissue, was not affected by the duration of the hormonal treatment (p = 0.97 and p = 0.68 for the prostate and PZ respectively). The median K^{trans} values were only slightly affected by the duration of the hormonal treatment (β = -0.03, p = 0.07 and β = -0.03, p = 0.045 for both the prostate and PZ, respectively. Table 3.2). Since tumor tissue is much more affected by the hormonal treatment than healthy tissue, increasing hormonal treatment times decrease the conspicuity of suspicious regions inside the prostate.

Even though the conspicuity of suspicious volumes is smaller in patients who had used hormonal treatment for a longer period of time, in 18/21 of the patients, who had used hormonal treatment longer than 3 months at the time of the MR exam, a suspicious volume could be defined based on qualitative assessment of the ADC and K^{trans} images. In figure 3.3 the ADC and K^{trans} maps of two typical patients are shown. Patient 1 (1a and 1b) had used hormonal treatment less than 3 months at the time of the MR exam. Patient 2 (2a, 2b, 2c and 2d) had used the hormonal treatment for more than 3 months at the time of the MR exam. In both patients a suspicious volume is found on the right side of the PZ. However, the conspicuity of the suspicious lesion is considerably larger in patient 1. Adjustment of the window/level settings nevertheless allows identification of the suspicious lesion in patient 2 (2c and 2d). This suggests that different threshold values need to be chosen to define tumor tissue after prolonged hormonal treatment.

To assess imaging threshold values for ADC and K^{trans} maps, we performed logistic regression. Before calculating the tumor probability functions based on ADC values, the mean lowest ADC values were adjusted for GS. The duration of hormonal therapy affects the tumor probability functions based on K^{trans} and ADC values in the PZ (figure 3.4(a) and 3.4(b)). Based on figure 3.4(a), for a tumor probability of 95%, ADC thresholds should be set at $7.8{\cdot}10^{-4}$ mm^2/s and $6.7{\cdot}10^{-4}$ for the patients who used the hormonal treatment longer than 3 months and patients who used the treatment 0-3 months, respectively. For the same tumor probability the K^{trans} maps should be thresholded at 0.25 or 0.35 min^{-1} for the patients who used the hormonal treatment longer than 3 months and patients who used the treatment 0-3 months, respectively (figure 3.4(b)).

3.4 Discussion

In this study, we retrospectively investigated the relation between the duration of androgen deprivation and DWI and DCE-MRI parameters. We found that tumor ADC values are associated with prolonged use of androgen deprivation. Tumor ADC values are considerably larger for longer hormonal treatment periods. After adjusting

Table 3.2: ADC and K^{trans} values for patients using hormonal treatment 0-3 months and longer than 3 months at the time the MR exam was performed.

	n	mean	standard deviation	β	p	β adjusted for confounders	p
Values for tumor tissue							
Mean lowest ADC$_{prostate}$* [mm^2/s]							
0-3 months	75	$4.7{\cdot}10^{-4}$	$1.7{\cdot}10^{-4}$	reference			
>3 months	21	$6.0{\cdot}10^{-4}$	$1.9{\cdot}10^{-4}$	$1.3{\cdot}10^{-4}$	0.001	$1.2{\cdot}10^{-4}$*	0.003
Mean lowest ADC$_{PZ}$* [mm^2/s]							
0-3 months	75	$5.4{\cdot}10^{-4}$	$1.4{\cdot}10^{-4}$	reference			
>3 months	21	$7.0{\cdot}10^{-4}$	$1.5{\cdot}10^{-4}$	$1.5{\cdot}10^{-4}$	0.001	$1.3{\cdot}10^{-4}$*	0.008
Mean highest $K^{\text{trans}}{}_{prostate}$ [min^{-1}]							
0-3 months	75	0.46	0.21	reference			
>3 months	21	0.32	0.13	-0.14	0.009		
Mean highest $K^{\text{trans}}{}_{PZ}$ [min^{-1}]							
0-3 months	75	0.35	0.16	reference			
>3 months	21	0.22	0.10	-0.13	0.001		
Values for healthy tissue							
Median ADC$_{prostate}$ [mm^2/s]							
0-3 months	75	$11{\cdot}10^{-4}$	$1.5{\cdot}10^{-4}$	reference			
>3 months	21	$11{\cdot}10^{-4}$	$1.4{\cdot}10^{-4}$	$0.02{\cdot}10^{-4}$	0.97		
Median ADC$_{PZ}$ [mm^2/s]							
0-3 months	75	$11{\cdot}10^{-4}$	$1.8{\cdot}10^{-4}$	reference			
>3 months	21	$11{\cdot}10^{-4}$	$1.5{\cdot}10^{-4}$	$0.2{\cdot}10^{-4}$	0.68		
Median $K^{\text{trans}}{}_{prostate}$ [min^{-1}]							
0-3 months	75	0.16	0.06	reference			
>3 months	21	0.13	0.06	-0.03	0.07		
Median $K^{\text{trans}}{}_{PZ}$ [min^{-1}]							
0-3 months	75	0.15	0.06	reference			
>3 months	21	0.12	0.05	-0.03	0.045		

* Adjusted for Gleason score

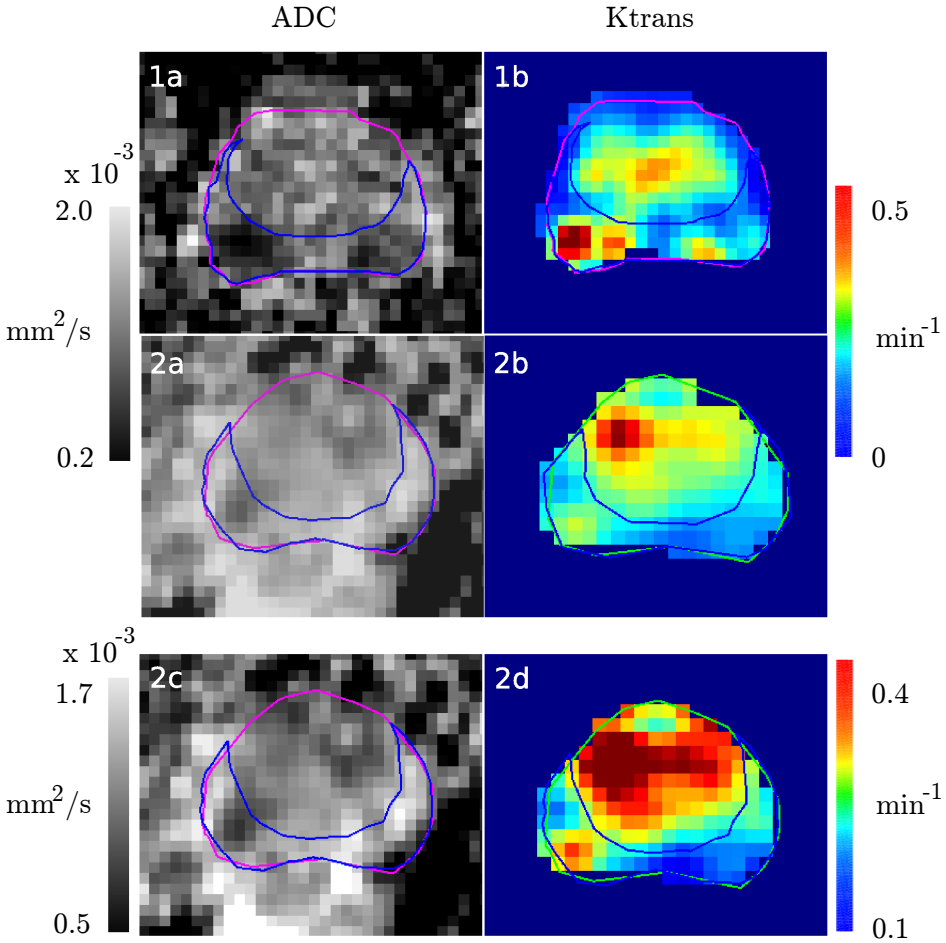

Figure 3.3: ADC and K^{trans} maps of two patients. Patient 1 (1a and 1b) had used hormonal treatment less than 3 months at the time of the MR exam. Patient 2 (2a, 2b, 2c and 2d) had used the hormonal treatment for more than 3 months at the time of the MR exam. In both patients a suspicious volume is found on the right side of the PZ. However, the conspicuity of the suspicious lesion is larger for patient 1. Adjustment of the window/level settings improves the visibility of the suspicious lesion in patient 2 (2c and 2d).

for GS, the mean lowest ADC in the PZ is $1.3{\cdot}10^{-4}$ higher in the 3 months group, than in the 0-3 months group. ADC is correlated with cell density [34, 35, 36]. Since, androgen withdrawal triggers the apoptotic pathway in androgen-dependent prostate cancer cells [63], this may explain the higher ADC values in patients with longer androgen deprivation periods.

We showed a decrease in K^{trans} values for increasing duration of the androgen deprivation treatment. On average the mean highest K^{trans} is 0.13 min^{-1} lower in the PZ in the >3 months hormonal therapy group, compared to the 0-3 months group. This is considerable given the spread in the data and the difference between healthy and tumor tissue. Since K^{trans} is associated with the number of leaky blood vessels, the decreased K^{trans} values after hormonal treatment suggest a decrease in tumor microvasculature. This result is in agreement with what was found by Alonzi et al [32].

The duration of hormonal therapy did not have a large effect on healthy tissue. Therefore, the conspicuity of tumor tissue is smaller in patients that had used hormonal treatment for a longer period. Nevertheless, in 18/21 patients it was still possible to define a suspicious region inside the PZ by qualitative assessment of the images.

Since the conspicuity of tumor tissue is smaller in patients with prolonged hormonal treatment use, ideally patients would start this treatment after the MR exam. However, many of the patients coming to a radiotherapy department are already using androgen deprivation. Therefore, when choosing a quantitative approach for tumor delineation it is of high importance to incorporate the knowledge on the effect of the duration of hormonal treatment on the MR scans. In this way, patient group specific imaging thresholds can be defined (figure 3.4(a) and 3.4(b)). However, the duration of hormonal treatment only partly explains the variation we find in ADC and K^{trans} values for different patients. The causes of this variation in ADC and K^{trans} values between patients need to be studied further. Understanding the causes of variation could increase the voxel based sensitivity and specificity of DWI and DCE-MRI by the definition of more specific thresholds for the individual patient.

IMRT and 125-I brachy patients are scheduled for hormonal treatment for different reasons. Patients scheduled for brachytherapy are treated with hormonal therapy, when the prostate is considered too large for proper dose coverage with the 125-I seeds. In IMRT patients hormonal treatment is prescribed to improve treatment outcome [64]. Since the IMRT and 125-I brachy patients are not equally distributed over the two groups investigated, we investigated if we could identify confounding factors for the duration of hormonal treatment and ADC and K^{trans} values. GS>7 was identified as a confounding factor in the relation between duration of hormonal treatment and the mean lowest ADC. So, part of the difference in ADC values in the two hormonal treatment groups can be explained by the larger number of patients with high GS in the 0-3 months hormonal treatment group (table 3.2). The found effect of GS on ADC is in agreement with literature. Lower ADC values have been reported for higher GS [65, 66, 67].

This study has several limitations. First, we used the mean lowest ADC and the mean highest K^{trans} in a 5x5x5 mm^3 kernel inside the prostate and PZ as a measure

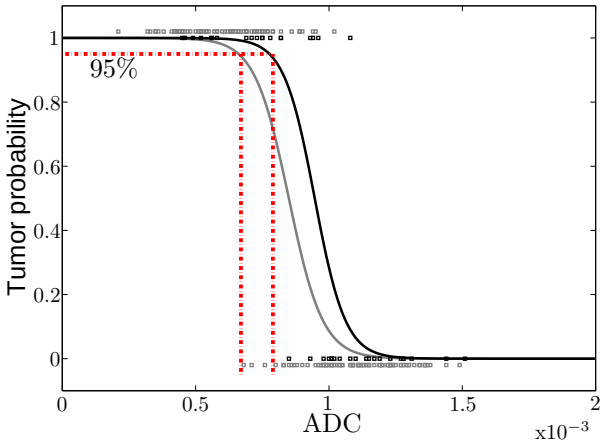

(a)

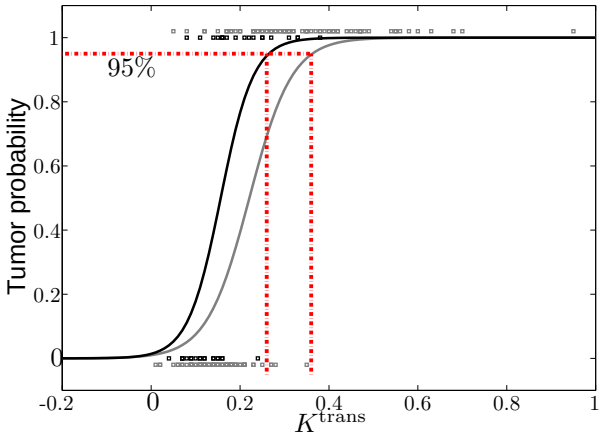

(b)

Figure 3.4: Tumor probability for different duration of hormonal treatment. The gray line represents the tumor probability function for patients who used hormonal treatment 0-3 months at the time of the MR exam. The black line represents the tumor probability function for patients using the hormonal treatment longer than 3 months at the time of the MR exam. In this situation, when one decides to boost only voxels with a tumor probability larger than 95% the K^{trans} maps should be thresholded at 0.25 or 0.35 min^{-1} for the patients who used the hormonal treatment longer than 3 months and patients who used the treatment 0 -3 months, respectively. For a the same tumor probability ADC maps should be thresholded at $6.7{\cdot}10^{-4}$ and $7.8{\cdot}10^{-4}$ mm^2/s for the patients who used the hormonal treatment longer than 3 months and patients who used the treatment 0-3 months, respectively.

for tumor tissue. This assumption may not be valid in all patients. However, since pathological validation is not possible in these patients, we prefer this measure because of its insensitivity to interobserver variations. We decided to choose a small kernel, to increase the chance that all voxels inside the kernel contain tumor tissue. In this way we only take the lowest ADC and the highest K^{trans} in a tumor into account. For this reason the reported tumor ADC values are lower than the average tumor ADC, whereas the reported K^{trans} values are higher than the average tumor K^{trans}.

Furthermore, we retrospectively included patients with different start dates of the hormonal treatment to study the effect of duration of androgen deprivation on MR parameters rather than performing a longitudinal study. In this way it was possible to include a large patient number. However, this study approach may dilute the effect of duration of hormonal treatment on ADC and K^{trans}. Furthermore, it is not possible to model the effect of hormonal treatment on the individual patient.

Despite these limitations, we could answer the relevant questions regarding the use of hormonal treatment in radiotherapy patients. Although, hormonal treatment affects tumor conspicuity in the prostate, the majority of hormonal treatment patients can be treated with a focal boost to a suspicious region inside the prostate. However, different imaging thresholds should be chosen depending on the duration of the hormonal treatment. Using this kind of clinical information for tumor delineation in the prostate, radiotherapy treatment could be further optimized for each individual patient.

3.5 Acknowledgement

This research is financially supported by the Dutch Cancer Society Grant No. UU-2009-4310.

CHAPTER 4

Validation of functional imaging with pathology for tumor delineation in the prostate

A version of this chapter has been published as
G. Groenendaal, M.R. Moman, J.G. Korporaal, P.J. van Diest, M. van Vulpen, M.E.P. Philippens and U.A. van der Heide 2010 MR - pathology registration *Radiotherapy and Oncology* **94** 145–150

Abstract
Introduction: A study was performed to validate magnetic resonance (MR) based prostate tumor delineations with pathology.
Material and Methods: Five patients with biopsy proven prostate cancer underwent a T2 weighted (T2w), Diffusion Weighted MRI (DW-MRI) and Dynamic Contrast-Enhanced MRI (DCE-MRI) scan before prostatectomy. Suspicious regions were delineated based on all available MR information. After prostatectomy whole-mount hematoxylin-eosin stained (H&E) sections were made. Tumor tissue was delineated on the H&E stained sections and compared with the MR based delineations. The registration accuracy between the MR images and H&E stained sections was estimated.
Results: A tumor coverage of 44-89% was reached by the MR based tumor delineations. The application of a margin of ∼5 mm to the MR based tumor delineations yielded a tumor coverage of 85-100% in all patients. Errors created during the registration procedure were 2-3 mm, which cannot completely explain the limited tumor coverage.
Conclusions: An accurate tissue processing and registration method was presented (registration error 2-3 mm), which enables the validation of MR based tumor delineations with pathology. Reasonable tumor coverage of about 85% and larger was found when applying a margin of ∼5 mm to the MR based tumor delineations.

4.1 Introduction

Increasing the radiation dose to the entire prostate reduces the probability of biochemical failure in prostate cancer patients [11, 12, 13, 14]. Evidence is emerging that recurrences are mostly located at the site of the primary tumor [15, 16]. This suggests that an additional boost dose to the gross tumor volume (GTV) in the prostate may further improve clinical outcome [17, 18, 40]. To obtain optimal benefit of such an approach, a proper delineation of the GTV is needed.

Magnetic Resonance (MR) techniques like T2 weighted (T2w) imaging, Diffusion Weighted Imaging (DWI), Dynamic Contrast-Enhanced (DCE) MRI and MR spectroscopy have been extensively studied for prostate cancer imaging. These techniques are validated and high sensitivity and specificity values are reported, when these techniques are used for tumor detection in the prostate [26, 27, 28, 19, 29, 30, 31, 43, 20, 21, 22, 23, 44]. Also in a radiotherapy context functional MRI techniques are beginning to be used for treatment and follow-up [68, 69, 70].

Accurate validation of these techniques on small volumes within the prostate is challenging, because processing and registration of the prostatectomy specimen need to be very precise. In a diagnostic setting the exact tumor location and extent are not relevant. Therefore, the validation of MR techniques has mainly been done on larger parts of the prostate, like octants [20, 19, 30]. Although methods have been proposed to obtain more accurate validation [56]. Sensitivity and specificity values found in these previous studies cannot be directly used for the purpose of tumor delineation, where decisions on a voxel level are required. In addition to the more complicated validation, the impact of noise and geometrical distortions induced by the MR scanner is larger when considering smaller prostate volumes. Relative to the diagnostic procedure, tissue heterogeneity might play a more important role in tumor delineations. The detection of a tumor with DCE-MRI and DWI is based on a high microvessel and cell density inside the tumor. Therefore, regions inside the tumor containing a low microvessel and cell density might be missed.

In this study we present a tissue processing and registration method, which enables the validation of MR based tumor delineations with their pathological reference delineations. This method was used to investigate the accuracy by which prostate tumors can be delineated using MR imaging techniques. We investigated what margin on the MR based GTV delineation is necessary to obtain good tumor coverage. The topological correspondence between the MR based GTV delineation and the tumor on the H&E stained section will be limited by errors created by the registration of the H&E stained sections with the MR images. We estimated these registration errors in order to estimate to which extent mismatches between the MR based GTV delineations and the pathological reference delineations are caused by these errors.

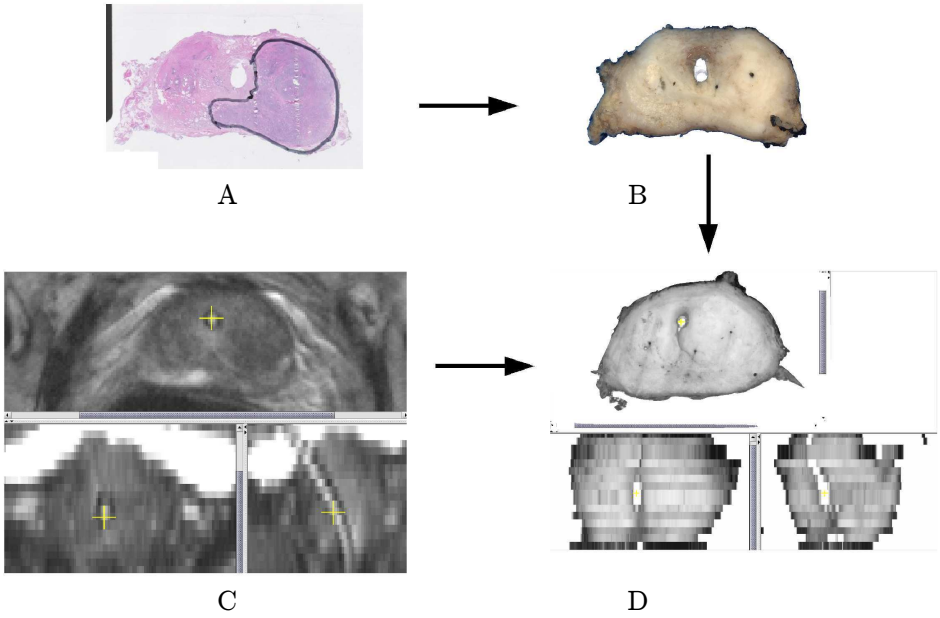

Figure 4.1: Different registration steps. First the H&E stained sections (A) were registered to the corresponding macroscopic slices (B) using the inserted carbon rods as landmarks. Then the macroscopic slices were stacked in order to obtain a 3D prostate reconstruction (C). Finally, the T2w MR image was registered to the 3D prostate reconstruction.

4.2 Methods and Materials

4.2.1 Imaging

Five patients with biopsy proven prostate cancer were included in this study (patient age 54-74 year, PSA 14-29 ng/ml, pathological Gleason 6-8, pathological T stage T2a-T3a). The study was approved by the institutional review board and informed consent was obtained from all patients. Prior to prostatectomy all patients underwent a T2w, DWI and DCE-MRI exam. In contrast to many prostate imaging validation studies, we decided not to use an endorectal coil to prevent deformations of the prostate, that complicate the treatment planning in a radiotherapy setting. Before the MR exam, a catheter was inserted into the urethra of the patients to facilitate registration afterwards.

T2w images were acquired with a fast spin-echo sequence, TR/TE = 8396/120 ms, echo train length 13, acquisition matrix 256x256, FOV = 20 cm, slice thickness 3 mm, intersection gap 1 mm.

DWI scans were performed using a multislice single shot SE-EPI sequence (TR/TE = 5000/54 ms, acquisition matrix = 152 x 107, FOV = 38 cm, 9 averages, EPI-factor = 47, slice thickness = 3 mm, intersection gap = 1 mm, b values = 500, 1000, 2000

s/mm^2). DW-MR images made with a b value of 1000 s/mm^2 or 2000 s/mm^2 (when available) were inverted and used for tumor detection during further analysis. Apparent Diffusion Coefficient (ADC) values were calculated, using the natural logarithm of the signal from scans made with b values of 500 and 1000 s/mm^2. Before calculating the ADC maps a moving average filter of 3x3 voxels in the x and y direction was used to smooth spatial fluctuations on the scans made with the different b values.

The DCE-MRI protocol consisted of a 3D spoiled gradient echo sequence (20 transverse partitions, 2.5 mm section thickness, TR/TE = 4/1 ms, acquisition matrix 160 x 160, FOV 40 cm, flip angle 8°). Scans were repeated 120 times at 2.4s intervals. A concentration of 0.1 ml/kg of Gadovist (Schering AG, Berlin, Germany) contrast was injected with 2 ml/s, followed by a saline flush. Concentration of the contrast agent was calculated from the MR signal using preceding small flip angle scans with three flip angles (6, 16 and 32°, TR/TE = 50/1.1 ms). Before applying a tracer kinetics model, a moving average filter of 3x3 in the x and y direction was used to smooth spatial fluctuations for each time point. Then, for each voxel the Generalized Kinetic Model [53] was fitted to the measured concentration time curves, using the linear least-squared method published by Murase [54]. A generic, patient averaged, arterial input function was used as an input for the model. This yielded 3D maps of the volume transfer constant K^{trans}.

Low signal intensity on the T2w image, the inverted DW-MR images and the ADC maps as well as high signal intensity on the K^{trans} can all be indications of tumor tissue. A radiation oncologist, experienced in reading these images delineated GTVs inside the prostate on the T2w image based on the information of all available MR images.

4.2.2 3D prostate reconstruction

After prostatectomy we inserted three carbon rods in the prostate specimen to facilitate the 3D reconstruction. Subsequently, we cut the prostate into slices of 4 mm and the precise thickness of these (macroscopic) slices was measured using a vernier caliper. Finally, whole mount microscopic sections were cut from the macroscopic paraffin embedded slices and stained with hematoxylin-eosin (H&E). The pathologist delineated tumor tissue on the H&E stained sections using a microscope. These delineations served as a reference to validate the MR based delineations. Both the macroscopic slices and the H&E stained sections including the delineations were digitized.

In order to compare the H&E stained sections with the MR images, the digitized images need to be registered. Direct registration between the MR images and H&E stained sections is difficult. Therefore the registration was performed in multiple steps. First the H&E stained sections were manually registered to the corresponding macroscopic slices, using the inserted carbon rods as landmarks. To register the H&E stained sections to the macroscopic slices rigid registration including scaling was used.

After this, the digitized macroscopic slices were stacked to create a 3D reconstruction of the prostate. Stacking was performed using manual rigid registration, where the previously inserted carbon rods served as landmarks.

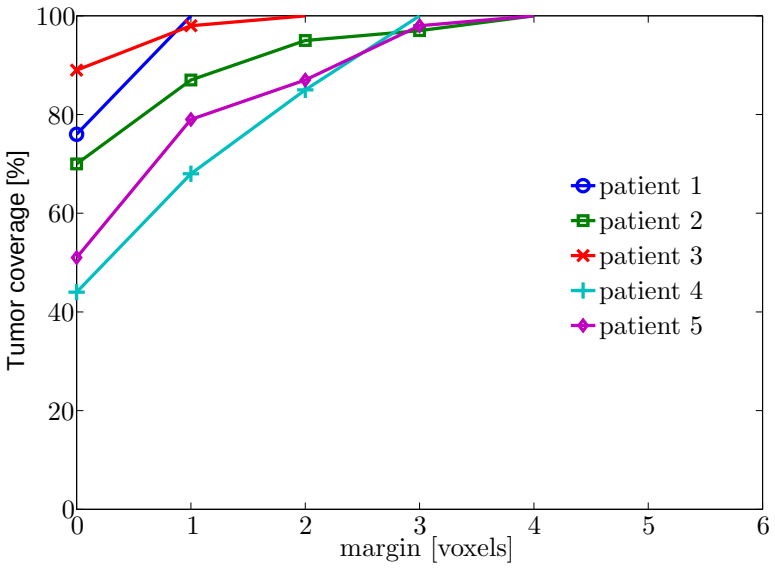

(a)

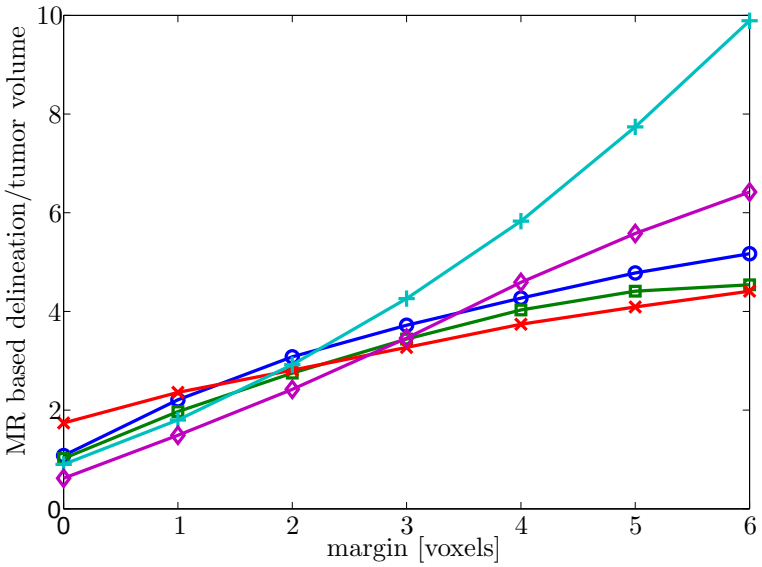

(b)

Figure 4.2: Effect of the application of margins around the delineated GTV in the MR images compared to the pathology based reference delineations.A. Tumor coverage [%] by GTV delineation for different margins B. Delineated volume divided by tumor volume found in histopathology for different margins. The voxel size used was 2.5x2.5x2.5 mm^3.

4.2.3 MRI - pathology registration

Finally the MR images were registered to the reconstructed prostate. Since the 3D prostate reconstruction shows poor contrast, fully automatic registration appeared not successful for the purpose of this study. Therefore, the prostate, peripheral zone (PZ) and the catheter were manually segmented on both the T2w image and the 3D reconstruction of the prostate specimen. The segmented structures were given a similar signal intensity on the T2w image and the reconstructed prostate. After this we registered the images, using rigid registration including scaling. We used normalized correlation as a measure to optimize the registration. Finally, we performed a non-rigid registration step, to account for deformations. The transformations found were applied to all MR images. The registration between the MR images and the H&E stained sections was performed using Elastix, a freely available image registration toolkit [51]. The 3D prostate reconstruction and registration steps are summarized in figure 4.1.

4.2.4 Comparison MR images and histopathology

After registration, the delineations on the H&E stained sections and the delineations on the MR images were compared in order to investigate the minimal size of tumors that could be detected. A tumor lesion was considered as detected when the reference delineation and the MR based delineation were (partly) overlapping.

For the investigation of MR based delineation accuracy, we focused on the dominant lesion in the prostate. The stacked H&E stained sections and the MR images were downsampled to a resolution of 2.5x2.5x2.5 mm^3. From the reference and MR based delineations of the dominant lesion masks were created. From these masks, the tumor coverage by the MR based delineation was calculated. After this, margins of one to six voxels where applied on the GTV delineation. Voxels outside the prostate where not included in this margin. It was chosen to apply the margin in voxels instead of millimeters, because this makes it more straightforward what voxels to include within the margin. For each applied margin, the tumor coverage was calculated and the delineated MR based GTV volume was compared with the real tumor volume.

4.2.5 Estimation of registration errors

In order to calculate the error of the registration between the H&E stained sections and the macroscopic slices, the carbon rods were used. In total three carbon rods were inserted into the prostate. Every time two carbon rods were used for the registration, and the third rod was used for the validation. This procedure was repeated three times for each prostate for different combinations of carbon rods.

The estimation of the error obtained during the stacking procedure was retrieved in a similar way. However, instead of comparing carbon rod positions slice by slice, the estimation of the registration errors of the stacking was performed by fitting a 3D line through the carbon rods, which had not been used during the registration procedure.

For the calculation of the error of the registration between the T2w image and the 3D prostate reconstruction, we used the delineations of the prostate in both images.

Table 4.1: Mean registration errors for the different registration steps

	H&E sections - macroscopic slices	**Stacking macroscopic slices**	**3D stack - T2w image (Rigid)**	**mean**
patient 1	0.18 mm	0.23 mm	1.67 mm	1.70 mm
patient 2	0.91 mm	0.38 mm	1.93 mm	2.17 mm
patient 3	0.78 mm	0.63 mm	1.65 mm	1.93 mm
patient 4	0.38 mm	0.59 mm	2.93 mm	3.01 mm
patient 5	0.27 mm	0.29 mm	2.32 mm	2.35 mm

The distance between the contours in both images was calculated using the method described by van der Put et al. and served as a measure for the registration error [71].

4.3 Results

In total, 22 lesions were delineated in five prostates by the pathologist. From these lesions, five were larger than 1 cc. All these five dominant lesions could be detected by the experienced radiation oncologist based on the MR images. From the remaining lesions 4/17 could be detected. The smallest tumor lesion detected was 0.56 cc. When looking in more detail to the tumors, that were missed by the experienced radiation oncologist, it appeared that they could not be distinguished based on contrast compared to the surrounding tissue. One volume was delineated, which appeared not to contain tumor tissue.

To investigate the accuracy of the delineations created by the experienced radiation oncologist we focused on the dominant tumor lesions. In figure 4.2(a), it can be seen the that tumor in patient 3 was almost completely covered by the delineation created by the experienced radiation oncologist. In figure 4.3 a good correspondence between the tumor on the H&E stained section and the regions that look suspicious on the MR images can be appreciated.

In all other patients, the tumor coverage by the MR based delineation was less (44-76%, figure 4.2(a)). The MR based delineations had a volume of 62-174% of the real tumor volume. Applying a margin to the MR based delineations resulted in a steep increase of tumor coverage. The application of a margin of two voxels (voxel size 2.5x2.5x2.5 mm^3) resulted in a reasonably good tumor coverage of 85-100% (figure 4.2(a)). When margins of two voxels were applied to the delineations, the final GTVs were 2.5-3 times the real tumor volumes (figure 4.2(b)).

The limited tumor coverage, especially found when no margin was applied, could be partly caused by errors created during the registration process. We estimated the registration errors for the different registration steps (table 4.1). For each patient, the registration errors for each different registration step are depicted. It is shown that the error created during the registration between the 3D prostate reconstruction and

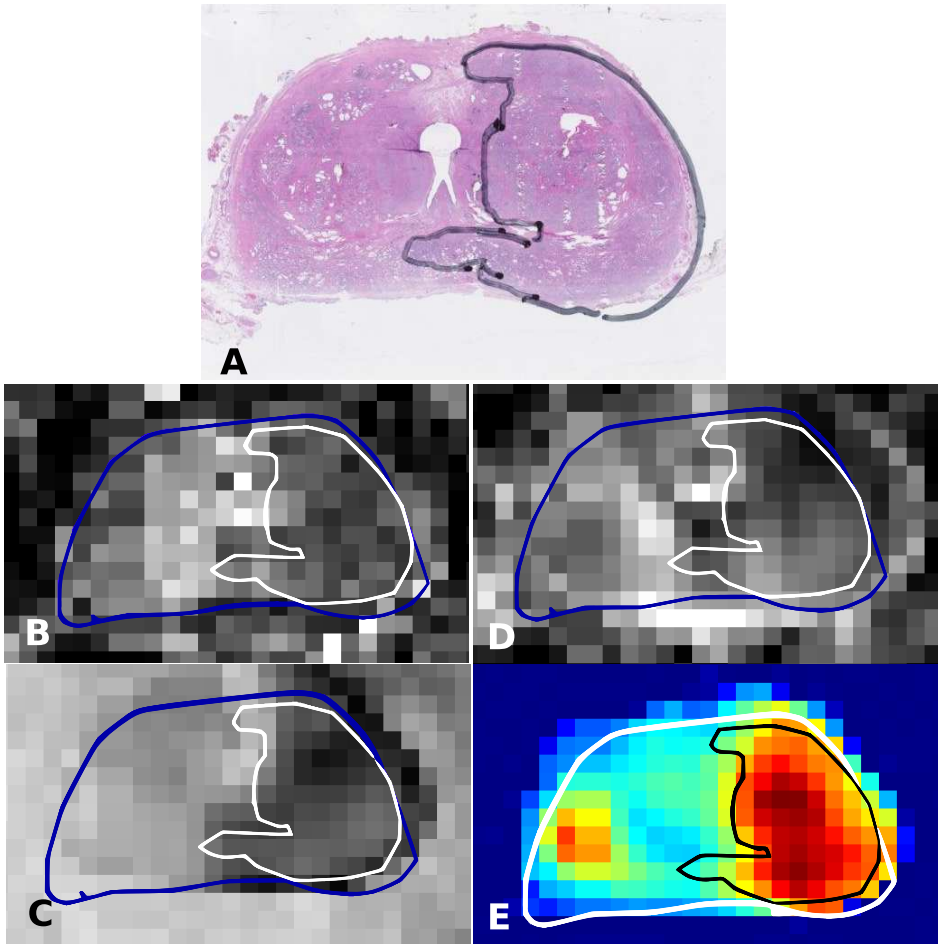

Figure 4.3: Comparison of the tumor delineated in an H&E stained section with the corresponding MR images A. H&E stained section with a delineation created by the pathologist. This delineation is copied to al the registered MR images B. T2w image C. DWI image D. ADC map E. K^{trans} map

the T2w MR image was the main source of error. Combining all sources of error in the table led to an overall average registration error of about 2-3 mm.

In table 4.1, the average error for the registration between the 3D prostate reconstruction and the T2w image is shown. In the color overlay in figure 4.4, the upper row shows the distance between the prostate contour on the T2w image and the 3D prostate reconstruction. The error induced by the registration between the 3D prostate reconstruction and the T2w image varied considerably over the prostate volume. Inside the prostate contours, the tumor volumes as delineated by the pathologist are shown (figure 4.4, lower row). The color overlay shows the distance between the delineation created by the pathologist and the MR based delineations. At some parts the MR based delineation was inside the pathology reference delineation. Here parts of the tumor were missed. At other locations the MR based delineation was outside the pathology reference delineation. On these locations, healthy tissue was misclassified as tumor tissue.

In all patients the MR based delineations show partly good correspondence with their pathology reference delineations. However, in other parts considerable deviations are found between the two types of delineations. When comparing the deviations between MR based and pathology based delineations with the registration errors shown in the upper row and the other errors in table 4.1, it is clear that the registration errors cannot fully explain the differences in delineations by the pathologist and the expert.

When we looked to the parts of the tumor, which were missed by the MR based delineations, three types of missed tumor regions could be distinguished. The first type were regions with a low ADC, but normal K^{trans} values compared to the surrounding tissue. This was found in patient 1 and 2, although the missed tumor regions in patient 2 showed a higher ADC than the region delineated on the MR image. The second type were regions with high K^{trans}, but normal ADC. This was found in patient 4, although the K^{trans} values in the missed regions were similar to K^{trans} values at the other site of the prostate were no tumor was located. In the third type no low ADC or high K^{trans} values were found (patient 5). The volume of the tumor in patient 3 was overestimated by the MR based delineations. This could be caused by the presence of a second tumor close to the primary tumor. This second tumor was not recognized by the expert as second tumor, but included as part of the primary tumor.

4.4 Discussion

In this study, we present a tissue processing and registration method, which enabled the validation of MR based tumor delineations with histopathology. Tumor lesions were delineated on the MR images by one observer. Lesions down to a size of 0.56 cc could be detected. Lesions that were not detected, appeared to show a similar signal intensity as the surrounding tissue on the MR images. Eight of the tumor lesions detected by the pathologist were smaller than two voxels on the ADC and K^{trans} images. Partial volume effects together with the application of the moving average filter make detection of these small tumors very unlikely. The dominant lesions, which are

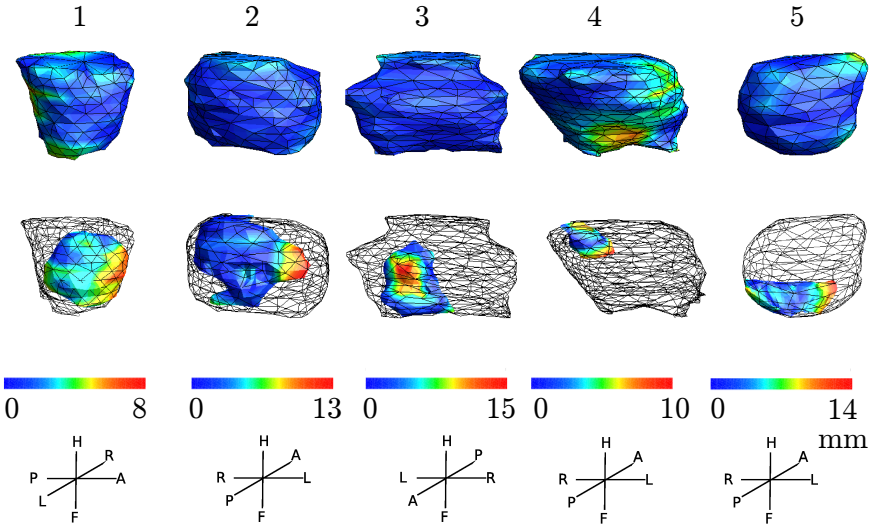

Figure 4.4: CTV contours of all included patients. The difference between the prostate contour on the T2w image and the contour of the prostate reconstruction after rigid registration is shown by the color overlay. In the lower images the tumor delineation created by the pathologist is shown inside the prostate. The distances between the tumor delineation created by the pathologist and the tumor delineation created by the experts are shown in the color overlay.

assumed to be clinically most relevant, were all detected. Delineation of these dominant suspicious regions on the MR images yielded a tumor coverage of 44-89%. The application of margins to these delineations increased the tumor coverage considerably. For a margin of two voxels (voxel size 2.5x2.5x2.5 mm^3) a tumor coverage of 85% or more was reached in all patients.

The limited tumor coverage by the initial MR based delineations could be partly caused by the errors created during the registration process. The error created during the registration of the T2w image with the 3D prostate reconstruction was the main source of error (table 4.1). Delineation errors of the prostate, catheter and PZ play a role in the registration and validation of this processing step. The registration error was calculated based on the prostate contour. This error might be smaller than the tumor registration error.

The overall registration error reported in table 4.1 might be decreased by the non-rigid registration step, performed after the rigid registration. Unfortunately, it was not possible to calculate the registration error for this non-rigid registration step,

since no landmarks were available. However, the deformations performed were small (maximum ∼1 mm) and were mostly found near the prostate and PZ contour.

In addition to errors in the registration process, also errors in the tissue processing procedure occurred. The slicing of the prostate resulted not always in slices of exactly the same thickness, but this difference was very small (mean standard deviation of slice thickness was 0.2 mm, when the most outer slice was not taken into account). Furthermore, the removal of the prostate out of the body and the fixation in formalin caused deformations. We expect that the registration procedure (partly) accounted for these processing errors.

Taking all this into account, we expect to end up with an average overall registration error of 2-3 mm for all the included patients. This error is very small and makes the comparison of delineations on histopathological data and delineations on MR images possible. However, this error will have influence on the tumor coverage by the MR based delineation. A margin on the expert delineations of 1-2 voxels (voxel size 2.5x2.5x2.5 mm^3) needs to be applied to correct for errors of this size.

Applying a margin of 2 voxels yields a much better tumor coverage (85% or more in all patients). However, only in two patients full tumor coverage was reached. The differences between the pathology reference delineations and MR based delineations cannot be fully explained by registration errors, as underlined in figure 4.4. Geometrical distortions, especially seen in the diffusion weighted scans, and noise induced by the scanner will affect the MR images and therefore the MR based delineations. Another reason for the deviations between the delineations created by the pathologist and the MR based delineations are the tissue characteristics reflected by the MR images. Increased cell density and microvessel density are expected to be associated with tumor tissue. However, these characteristics can be highly heterogeneous in prostate (tumor) tissue. Langer et al. showed the difference in detectability for sparse and dense tumors, where tumors where defined sparse if more than 50% of their cross-sectional areas contained primarily normal tissue. The dense (part of) tumors could be much easier detected by looking at T2w images and ADC maps [39]. Also in this study, ADC values associated with healthy tissue where found inside volumes defined as tumor tissue by the pathologist. Similar findings were done for K^{trans}.

The tumor coverage of 85-100%, when a margin of two voxels (voxel size 2.5x2.5x2.5 mm^3) was applied, suggests that functional prostate imaging is useful in a radiotherapy context. However, studies on larger patient groups are necessary to draw definitive conclusions about margins.

A tumor delineation error has a systematic impact on the treatment. Systematic sources of error in prostate radiotherapy are the interobserver variation in prostate delineation (∼1 mm) [72] and systematic positioning errors, which can be minimized to less than 1 mm with appropriate position verification [4]. While a margin of ∼5 mm around the delineated tumor would be sufficient to accomodate positioning uncertainties, we found that small parts of the tumors could be missed in comparison with pathology.

This might affect the tumor control probability. The tumor control probability depends on the volume of the underdosed part as well as the level of underdosage [73].

Assuming a boost dose of 10 to 20% of the regular prostate dose and a tumor coverage of 85-100%, we believe that the impact on tumor control probability remains small.

In conclusion, in this study a method was presented which enables the validation of MR based delineations with histopathological reference delineations. In this study a tumor coverage of 85-100% was found when a margin of $\sim$5 mm was applied to the MR based GTV delineations.

4.5 Acknowledgement

This research is financially supported by the Dutch Cancer Society Grant number UU2009-4310.

CHAPTER 5

Pathological validation of a multiparametric model for tumor delineation in the prostate peripheral zone

A version of this chapter has been accepted as
G. Groenendaal, A. Borren, M.R. Moman, P.J. van Diest, M.E.P. Philippens, M. van Vulpen and U.A. van der Heide 2011 Pathological validation of a Model based on Diffusion-Weighted imaging and Dynamic contrast-enhanced MRI for tumor delineation in the prostate peripheral zone, International Journal of Radiation Oncology Biology Physics

Abstract
Background and Purpose: For focal boost strategies in the prostate, the robustness of MR based tumor delineations needs to be improved. To this end we developed a statistical model, which predicts tumor presence on a voxel level inside the peripheral zone (PZ). Furthermore, we show how this model can be used to derive a valuable input for radiotherapy treatment planning.
Material and Methods: The model was created on based on expert tumor delineations of 87 radiotherapy patients. For the validation of the voxel-wise performance of the model an independent group of 12 prostatectomy patients was used. After model validation, the model was stratified to create three different risk levels for tumor presence: GTV, high-risk CTV, low-risk CTV.
Results: The model gave an area under the receiver operating characteristic curve (AUC) of 0.70 for the prediction of tumor presence in the prostatectomy group. When the registration error between MR images and pathology was taken into account, the AUC further improved to 0.89. We proposed that model outcome values with a high positive predictive value (PPV) can be used to define the GTV. Model outcome values with a high negative predictive value

(NPV) can be used to define low-risk CTV regions. The intermediate outcome values can be used to define a high-risk CTV.
Conclusions: We developed a logistic regression with a high diagnostic performance for voxel-wise prediction of tumor presence. The model output can be used to define different risk levels for tumor presence, which in turn could serve as an input for dose planning. In this way the robustness of tumor delineations for focal boost therapy can be greatly improved.

5.1 Introduction

Evidence is emerging that local recurrences of prostate cancer is often seen at the original tumor location inside the prostate [15, 16]. Consequently, an additional boost dose to this tumor potentially could improve the tumor control probability. By limiting the boost to the tumor volume, the toxicity to the organs at risk may be kept at a minimal level [17, 18, 40, 59]. Recently, a randomized phase III trial started to investigate the benefit of a focal lesion ablative microboost [74].

Functional magnetic resonance imaging (MRI) techniques, such as diffusion weighted imaging (DWI) and dynamic contrast enhanced (DCE) MRI may be used to guide tumor delineation inside the prostate. Both techniques can be used to distinguish tumor from healthy tissue [26, 27, 28, 22, 21, 19, 20, 30, 23]. Sensitivity levels range from 54-84% and from 59-87% for DWI and DCE-MRI respectively. Specificity values for DWI and DCE-MRI range from 74-100% and from 74-84% [27, 28, 20, 30].

In the current clinical practice, delineation of prostate tumors is a manual procedure, where a radiation oncologist and radiologist decide what to include in the target, based on the available images and clinical information. Interpretation of multiparametric images can be difficult in particular when apparently conflicting information is obtained from different MRI techniques. Indeed, in an earlier study, we found that the overlap between regions identified as suspicious by DWI and DCE-MRI is quite limited [61].

A very simple approach to deal with this inconsistency was to define the region indicated by both modalities as suspicious as GTV. Regions identified by only one of the modalities could be interpreted as a high-risk CTV. However, to improve the robustness of interpretation of the images, automated methods are required that translate multiparametric data into appropriate segmentations of the target volume. To improve the robustness of MR based prostate tumor delineations for radiotherapy we developed a statistical model, which predicts tumor presence on a voxel level inside the peripheral zone (PZ). To make the model outcome applicable in a radiotherapy treatment setting, the outcome of the tumor prediction model was translated into discrete risk levels for tumor presence, which can be used as target volumes for treatment planning.

5.2 Methods and Materials

5.2.1 Study design

To improve the robustness of MR based prostate tumor delineations for radiotherapy we first created a validated logistic regression model, which predicts tumor presence on a voxel level. After this we translated model outcome into discrete risk levels for tumor presence, which can be used as target volumes for treatment planning. In order to create a validated model, we performed two steps: 1. Model creation 2. Model validation. Creation of the model was performed on 87 radiotherapy patients. From radiotherapy patients, a ground truth for the tumor delineations is not available. Therefore, validation cannot be performed on this patient group. For the validation of

Table 5.1: Patient characteristics

	Number of patients Model creation: Radiotherapy patients	Model validation: Prostatectomy patients
Total	87	12
Primary tumor stage		
Tx	0 (0%)	1 (1%)
T1	38 (44%)	8 (75%)
T2	29 (33%)	3 (25%)
T3	20 (23%)	0 (0%)
Gleason score		
6	54 (62%)	4 (33%)
7	31 (36%)	4 (33%)
8	0 (0%)	3 (25%)
9	2 (2%)	1 (1%)
PSA level [ng/ml]	11 (3.1-70)	11.0 (4.3-29)
Age [years]	67 (48-79)	62 (48-74)

the voxel-wise performance of the model an independent group of 12 prostatectomy patients was used. To make the model applicable in a radiotherapy setting, after model validation, the model was stratified to create three different risk levels for tumor presence: GTV, high-risk CTV, low-risk CTV.

5.2.2 Patients

The 87 consecutive radiotherapy patients were treated between April 2009 and July 2010. All patients had biopsy proven prostate cancer and underwent DWI and DCE-MRI as part of standard clinical care. Patients using hormonal therapy were not included in this study, as this therapy affects DCE-MRI images [32]. The independent prostatectomy group consisted of 12 patients. The model validation on prostatectomy patients was approved by the institutional review board and informed consent was obtained from all patients. The prostatectomy patients were included in the study between May 2005 and August 2010. Patient characteristics of the model creation group (radiotherapy patients) and the model validation group (prostatectomy patients) are summarized in table 5.1.

5.2.3 Imaging

On all patients a T2 weighted (T2w), balanced TFE, DWI and DCE-MRI exam were performed using a 3T Philips Achieva MR scanner. A 6-element phased array coil (sense cardiac) was used as receive coil during the scans. T2w images were acquired

with a fast spin-echo sequence, TR/TE = 8396/120 ms, echo train length 13, acquisition matrix 256x256, FOV = 20 cm, slice thickness 3 mm, intersection gap 1 mm. balanced TFE: TR/TE = 2.85/1.43 ms, echo train length = 40, acquisition matrix 192x249, FOV = 25 cm, slice thickness = 2 mm.

DWI scans were performed using a multislice single shot SE-EPI sequence (FOV = 38 cm, slice thickness = 3 mm, EPI-factor = 47, intersection gap = 1 mm, TR/TE=5000/54 ms, acquisition matrix = 152 x 107, 9 averages, sense factor = 2 in AP direction, phase encoding direction = PA). b values 300, 500 and 1000 s/mm^2 were used to calculate the apparent diffusion coefficient (ADC).

The DCE-MRI protocol used, consisted of a 3D spoiled gradient echo sequence (20 transverse partitions, 2.5 mm section thickness, TR/TE=4/1 ms, flip angle 8°, FOV = 40 cm, acquisition matrix = 160 x 160). Scans were repeated 120 times at 2.4s interval. A concentration of 0.1 ml/kg of Gadubutrol (1.0M)(Gadovist, Schering AG, Berlin, Germany) contrast was injected with 2 ml/s, followed by a saline flush. Concentration of the contrast agent was calculated from the MR signal using preceding small flip angle scans with three flip angles (6, 16 and 32°, TR/TE = 50/1.1 ms). Before applying a tracer kinetics model, a moving average filter of 3x3x3 voxels in the x, y and z direction was used to increase the signal-to-noise ratio. Although, high spatial frequency components are removed, this filtering step results in parameter maps with small voxels which are useful for delineation and which allows incorporation of K^{trans} maps in the voxel-wise tumor prediction model. Then, for each voxel the Generalized Kinetic Model [53] was fitted to the measured concentration time curves, using the linear least-squared method published by Murase [54]. This yielded 3D maps of the volume transfer constant K^{trans}. Due to the extent of the measurement errors on the patient specific input functions, a generic arterial input function (AIF) was used for all patients. A similar approach is often used to circumvent problems with AIF measurements [75, 76, 77, 78].

5.2.4 Model creation

In the radiotherapy group, highly suspicious and highly non-suspicious regions were delineated. This was done by an observer with 4 years of experience with the interpretation of functional MR images of the prostate. The delineation of highly suspicious volumes was based on hypointense values on the T2w, low ADC, high signal intensity on the b1000 image and high K^{trans} values. Also regions were delineated, which were expected to be healthy, based on normal appearing tissue on the T2w image, ADC, b1000 and K^{trans} values associated with healthy tissue. The voxels in these regions were used to create a logistic regression model, which can be used for predicting the presence of tumor tissue. From each voxel inside the delineated volumes the ADC and K^{trans} were retrieved as well as minimum, median, mean and maximum value in the adjacent 26 voxels (table 5.2).

The absolute K^{trans} values depend largely on the arterial input function (AIF). Several factors make accurate measurement of the AIF challenging: the non-linear relationship between signal and contrast agent concentration, T2*-effects at higher concentrations, B1-field inhomogeneities and inflow-artifacts [79, 80, 81, 82, 83, 84].

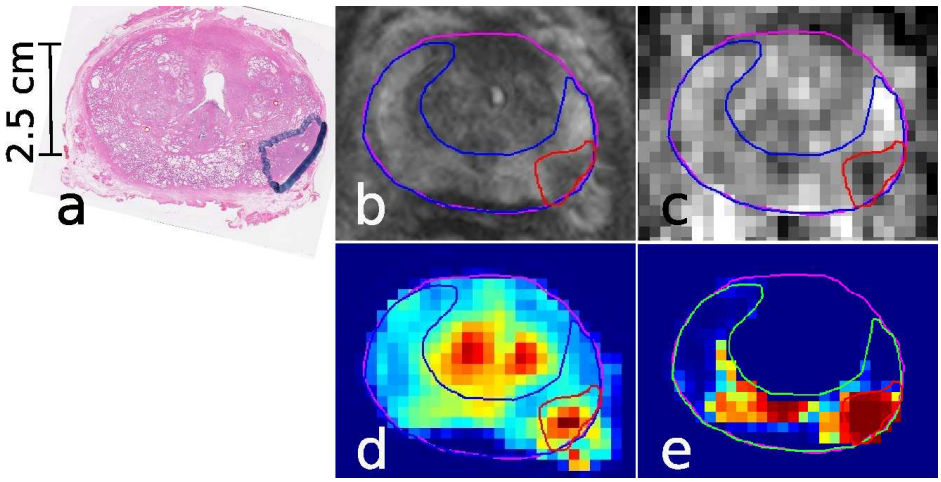

Figure 5.1: Patient example a. H&E stained section b. T2w image c. ADC map d. K^{trans} map e. model outcome

Therefore, K^{trans} values may vary largely between patients and institutes [19, 31, 30]. To overcome this, all K^{trans} maps were scaled to the median K^{trans} value in the total PZ, prior to inclusion in the model.

Furthermore, for each voxel, its relative position inside the prostate was retrieved from the MR scans. The relative z coordinate varied ranged from 0 for the most caudal slice to 1 for the most cranial slice. The relative x coordinate for each slice varied between 0 for the center of the prostate and 1 for the edge of the prostate. The relative y coordinate varied for each slide from 0 for the ventral side of prostate to 1 for the most dorsal side of prostate (table 5.2 for the definition of all parameters).

A logistic regression model was fitted to the data

$$f(z) = \frac{1}{1 + e^{-z}} \tag{5.1}$$

Where f is the probability that a voxel is part of a highly suspicious volume. z is a linear combination of all included variables. Before inclusion in the model, the correlation between all variables was calculated. If the absolute Pearson correlation coefficient between two variables was larger than 0.8, only one of the two parameters was included in the logistic regression model. We started with the inclusion of all remaining parameters in the model (full model). Step-wise elimination of variables was performed based on the significance of the change in -2 log likelihood. The threshold of the p value for removal was set to 0.15. Statistic analyses were performed using statistical package for social sciences, version 16.0 (SPSS, Chicago, IL, USA).

Table 5.2: Variables retrieved from MR scans

Parameter	Explanation
$\mathbf{ADC}_{voxel}$	ADC value in voxel i
$\mathbf{ADC}_{mean}$	Mean ADC value from voxel i and 26 surrounding voxels
$\mathbf{ADC}_{median}$	Median ADC value from voxel i and 26 surrounding voxels
$\mathbf{ADC}_{minimum}$	Minimum ADC value from voxel i and 26 surrounding voxels
$\mathbf{ADC}_{maximum}$	Maximum ADC value from voxel i and 26 surrounding voxels
Relative ${K^{\text{trans}}}_{voxel}$	Relative K^{trans} value in voxel i
Relative ${K^{\text{trans}}}_{mean}$	Mean relative K^{trans} value from voxel i and 26 surrounding voxels
Relative ${K^{\text{trans}}}_{median}$	Median relative K^{trans} value from voxel i and 26 surrounding voxels
Relative ${K^{\text{trans}}}_{minimum}$	Minimum relative K^{trans} value from voxel i and 26 surrounding voxels
Relative ${K^{\text{trans}}}_{maximum}$	Maximum relative K^{trans} value from voxel i and 26 surrounding voxels
Relative x coordinate	Value from 0 (center of prostate) to 1 (edge of prostate)
Relative y coordinate	Value from 0 (ventral side of prostate) to 1 (dorsal side of prostate)
Relative z coordinate	Value from 0 (most caudal slice) to 1 (most cranial slice)

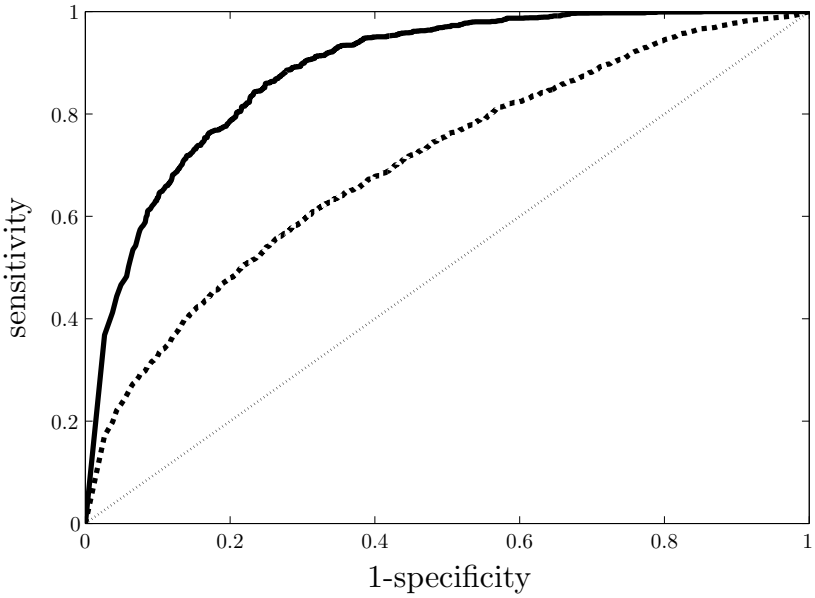

Figure 5.2: Average receiver operating curve for all patients. The average area under the curve was 0.89 when a method was applied to tissue deformation up to one voxel (black line). The average AUC was 0.70 when the compensation for tissue deformation was not applied (dashed line).

5.2.5 Model validation

To validate the model on prostatectomy patients, first the MR images of these patients needed to be registered to the corresponding hematoxylin and eosin (H&E) stained sections. For the first 5 patients, the prostatectomy specimens were processed and registered to the MR images as described in an earlier study [60]. The registration process was performed in three steps: 1. the reconstruction of the prostate from the macroscopic slices, 2. the registration of H&E stained slices to this reconstructed prostate, 3. the registration between the prostate reconstruction and the T2w MR image. On average the registration error of this method was 2-3 mm [60].

For patient 6-12, the protocol was further improved. Prior to slicing, the prostate was first embedded in agarose gel (5%). This made it possible to cut the prostates of these patients in 3-mm slices. Furthermore, it allowed to cut the prostate in an angle similar to the angle seen on the T2w image. These improvements in the protocol decreased the registration error to 1.5-2.5 mm.

For all patients, on average the registration error between the MR images and the histopathological data was about 1 voxel. This information needs to be taken into account, when validating the logistic regression model. Therefore, we used an ap-

proach that takes into account neighboring voxels when MR images and pathology are compared. The assumption was that any displacement of tumor voxels by prostate specimen deformation would only occur from the original voxel to a neighboring voxel (neighboring approach). With this method a tumor voxel is considered to correlate with suspicious imaging voxels even if it is present in a neighboring voxel. This method was not used for healthy voxels.

Using the neighboring approach, for each patient a receiver operating curve (ROC) was created and the area under the curve (AUC) was calculated. Furthermore, we calculated the positive predictive value (PPV) and negative predictive value (NPV) for different values of model outcome. To show the effect of the neighboring approach, we also calculated the AUC without application of this method.

5.2.6 Derivation of tumor delineations based on model outcome

A logistic regression model has a continuous outcome. For the delineation of treatment volumes, this outcome needs to be stratified. We chose to define three risk levels for tumor presence: gross tumor volume (GTV), high-risk CTV and low-risk CTV. For tumor boosting purposes, we chose to stratify the model outcome by choosing a threshold with a high tumor probability (high positive predictive value (PPV)) to define the GTV. In this way, only voxels with a high tumor probability will be boosted, keeping toxicity at minimal level. Voxels with a low tumor probability (high negative predictive value (NPV)) can be treated with the standard prostate dose. Voxels with an intermediate tumor probability are considered high-risk CTV. These voxels may also be boosted or safe margins could be applied around these prostate regions. Tumor probability depends on tumor voxel prevalence. Therefore, to calibrate the model outcome, an estimate of the tumor voxel prevalence in a patient group is needed. In order to choose sensible thresholds which can be used for the definition of the GTV, high-risk CTV and low-risk CTV, we plotted PPV and NPV curves for different model outcomes using the average tumor voxel prevalence in the prostatectomy patient group. Furthermore, to illustrate the sensitivity of PPV and NPV curves for tumor voxel prevalence, we plotted PPV and NPV curves for a range of tumor voxel prevalences between 10-40%.

5.3 Results

Patients in the prostatectomy and radiotherapy group were comparable in age and PSA levels. However, the percentage of patients with lower T stage and higher Gleason score was larger in the prostatectomy group. The delineated suspicious and non-suspicious regions had on average ADC values of $0.89{\cdot}10^{-3}{\pm}0.28{\cdot}10^{-3}$ and $1.47{\pm}0.32{\cdot}10^{-3}$ and average normalized K^{trans} values of 2.05±1.75 and 1.19±2.74, respectively.

When correlating all possible input variables for the model, we found that maximum ADC and K^{trans} values in a kernel around a voxel of interest correlated strongly to the median and mean ADC and K^{trans} values in this kernel (Pearson correlation $>$ 0.8). Therefore, mean and median ADC and K^{trans} values were not incorporated in

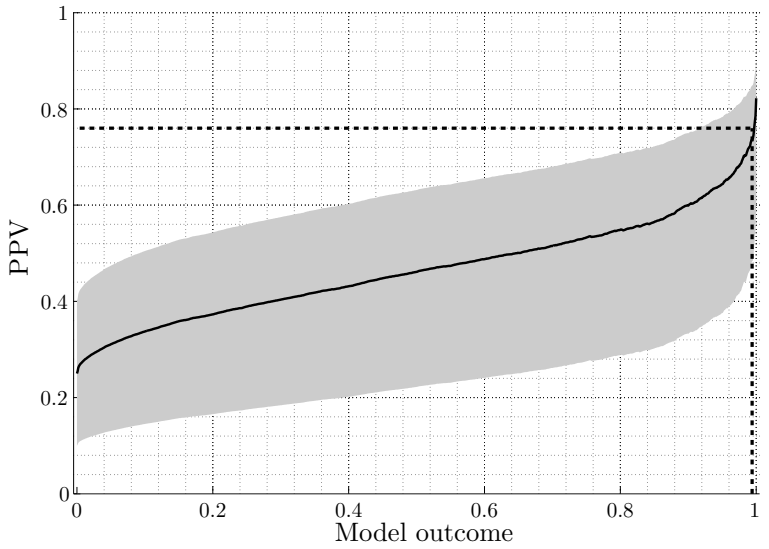

(a)

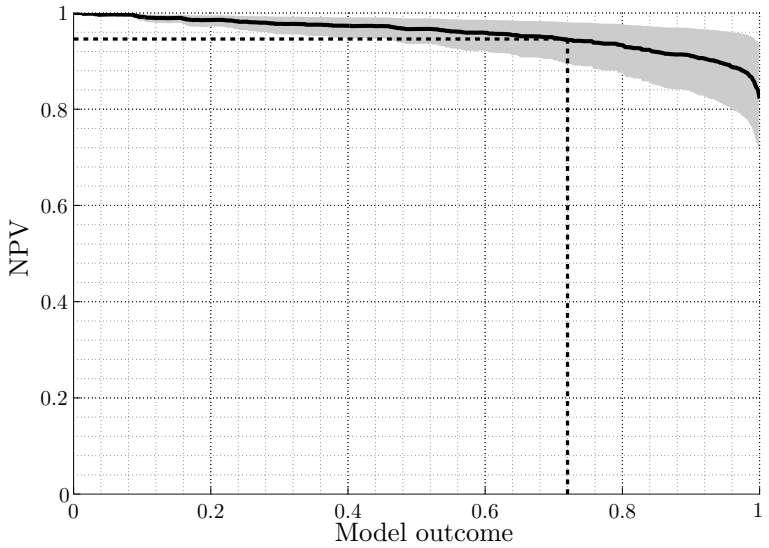

(b)

Figure 5.3: Positive and negative predictive value for different model outcomes. The black lines represent the PPV and NPV curves for the average tumor voxel prevalence found in the prostatectomy patient group (25%). The gray area represents the spread in these curves for tumor voxel prevalences ranging from 10-40% A model output with a high positive predictive value (>0.99) can be used to define a boost volume. Model outputs with a high negative predictive value (<0.72) can be used to define non-suspicious tissue. The intermediate values (0.72-0.99) can be treated as high-risk CTV.

Table 5.3: Parameter values in logistic regression model

Parameter	Regression coefficient
constant	0.72
ADC_{voxel}	-4002.3
$ADC_{minimum}$	-1009.1
$ADC_{maximum}$	-1860.4
Relative $K^{trans}{}_{voxel}$	1.9
Relative $K^{trans}{}_{minimum}$	-0.7
Relative $K^{trans}{}_{maximum}$	2.8
Relative x coordinate	0
Relative y coordinate	3.0
Relative z coordinate	-1.5

the model. From all other variables only the relative x coordinate (lateral direction, table 5.2) did not result in a significant change in the -2 log likelihood. The final model consisted of: the ADC and K^{trans} value in a voxel, the minimum and maximum of the ADC and K^{trans} in a kernel around this voxel and the relative y (ventral-dorsal direction) and z (caudal-cranial direction) coordinate. The regression coefficients of these variables are summarized in table 5.3.

The model was validated in the prostatectomy patient group. An example of the model outcome is shown in figure 5.1. The tumor, as delineated by the pathologist is also shown. A good correspondence can be appreciated between the voxels predicted as suspicious by the model and voxels indicated as tumor voxels by the pathologist. The AUC retrieved from the ROC curve for this patient was 0.79. When the neighboring approach was applied to compensate for registration errors up to one voxel the AUC was 0.96. The average ROC curve yielded an AUC value of 0.70. When compensating for tissue deformations up to one voxel the AUC increased to 0.89 (figure 5.2).

To obtain appropriate thresholds, which can be used to define volumes for dose planning, PPV and NPV curves were plotted (figure 3). The black lines represent the PPV and NPV curves for the average tumor voxel prevalence in the prostatectomy patient group (25%). A model output of 0.99 was chosen to define the GTV, based on its high PPV. Voxels exceeding a model output of 0.99 have a tumor probability of 74%.Voxels with a model output between 0.72 and 0.99 were considered high-risk CTV. Voxels below the threshold of 0.72 have a high NPV. The risk of tumor presence in these voxels is only 5%. The gray areas represent the spread in PPV and NPV curves for tumor voxel prevalences between 10-40%. Tumor voxel prevalence has only a minor effect on the NPV curve. The NPV for a threshold of 0.72 varies between 0.90-0.98. The PPV curve depends strongly on the tumor voxel prevalence (range 0.48-0.85 for a threshold of 0.99). Nevertheless, given the strong increase in PPV towards the end of the PPV curve, a model outcome threshold >0.99 to define the GTV seems appropriately independent of the exact tumor voxel prevalence Sensitivity, specificity, PPV and NPV values of GTV and high-risk CTV are summarized in table 5.4.

Table 5.4: Sensitivity, specificity, PPV and NPV values of GTV and high-risk CTV. Voxels with a model outcome >0.99 are considered GTV and have a tumor probability of 0.48-0.85. Voxels with a model outcome <0.99 have an NPV of 0.73-0.94

Region	**High-risk CTV**	**GTV**
Threshold model outcome	0.72	0.99
Sensitivity	0.89	0.48
Specificity	0.72	0.94
PPV*	0.26-0.68	0.48-0.85
NPV*	0.90-0.98	0.73-0.94

* For a tumor voxel prevalence of 25%.

Applying the GTV and high-risk CTV thresholds for the different prostatectomy patients yields the following images (figure 5.4). In these images can be seen that most of the voxels, which are considered as GTV based on model output, are confined to the tumor region. Furthermore, most of the tumor tissue is included in the high-risk CTV.

5.4 Discussion

To improve the robustness of MR based prostate tumor delineations we first developed a statistical model for the voxel-wise prediction of tumor presence. Validation of this model on an independent prostatectomy patient group showed a high diagnostic performance in all patients (mean AUC = 0.89). This enables objective interpretation of the functional MR images. To translate the model outcome to a useful input for radiotherapy dose planning, we thresholded the model to define three different risk levels for tumor presence: GTV, high-risk CTV and low-risk CTV. These risk-levels can be used for dose painting. Ideally, a tumor prediction model would be created on a large group of prostatectomy patients. Instead, we used a large group of radiotherapy patients. Given the good performance of our model on an independent group of prostatectomy patients, we believe that our approach is justified.

Prediction models have been developed before for regions inside the prostate [85] and on a voxel-wise basis [86, 87, 88, 89]. AUC values of the voxel-wise models ranged between 0.71-0.82. These AUC values are hard to compare with our study, since the validation of the previous models was only performed on one slice per prostate.

For the model creation we used the MR images to delineate highly suspicious and highly non-suspicious regions. In this way the model output is partly determined by the input and therefore we have an incorporation bias. However, since we validated our model on pathology patients, we believe that this approach is justified.

The average error of our registration procedure is about the size of one voxel [60]. To take this error into account, we used a neighboring method to calculate our sensitivity

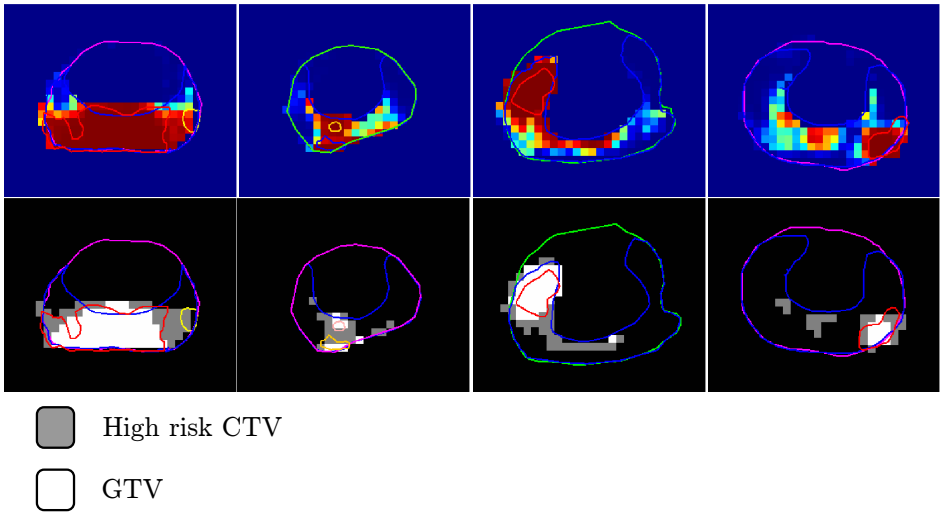

Figure 5.4: Model outcome translated to GTV and high-risk CTV regions. The tumors delineated by the pathologist are shown in the figures. For compensating for registration errors for displaying these figures the pathological tumor delineation was shifted with a maximum of 1 voxel.

and specificity values. Without this method less true positives and more false negatives would have been found. The method did not affect the number of true negatives and false positives. A similar method was applied by Turkbey et al. [90]. To take possible deformations into account, this group divided the prostate into 30 regions. A suspicious region was considered as true positive even when it occurred in one of the neighboring regions.

The registration process complicates the validation of MR images with pathology. Different strategies have been applied to work around this problem, varying from performing validation on larger parts of the prostate, taking into account neighboring regions, performing the validation only on selective regions and manually transferring contours from pathology to the MR images [90, 85, 86, 87, 88, 89]. Due to registration errors the exact location of the border between tumor and healthy tissue on the MR images cannot be validated with complete certainty. The large improvement in AUC (from 0.70 to 0.89) when taking into account the neighboring voxels, strongly suggests that the mismatch between MR and pathology is caused by errors in the registration process. However, even if the mismatch of one voxel between model outcome and pathology, is not caused by registration errors, this does not have a large effect in radiotherapy practice. Due to the limited steepness in dose fall off, in radiotherapy practice a voxel next to a suspicious voxel would still receive a substantial dose.

At present our model is developed for PZ tissue only. The majority ($\sim$70%) of tumors is located in the PZ, which was confirmed by our own data. In only two patients the dominant tumor lesion was located primarily in the central gland. The consequence is

that the majority of dominant tumor lesions will be found by our model. The extension of the model to the central gland is necessary for 30% of the patients. Due to the presence of benign hyperplasia, tumor detection is more challenging in the central gland. Therefore, most studies focus on the PZ, although promising sensitivity and specificity values for tumor detection in the central gland have been reported [25].

We found a relatively high number of false positives close to the central gland. This can be partly explained by registration errors. Furthermore, our training set did not consist of many voxels located directly near the central gland. We may be able to decrease the number of false positives in this location, when we include more of these voxels in our training set.

In this study we used relative instead of absolute K^{trans} values, since K^{trans} values vary greatly between patients and institutes [19, 31, 30]. Using relative K^{trans} values gave more consistent results for the patients in our study. Another advantage of using relative values is that the method can be used more easily in other clinics. Using relative K^{trans} values based on median values in the PZ is a disadvantage when the percentage tumor tissue inside the PZ is larger than 50%. In this situation the median is no longer representative for healthy tissue. Using lower percentiles to scale the K^{trans} is an option. However, a better consensus between measurement protocols in different institutes and a more accurate measurement of the arterial input function would be more advantageous. ADC values can be more easily compared between different institutes [21, 22, 26]

The patients in the radiotherapy and prostatectomy group differed in Gleason score and T stage. In our clinic, the model cannot be validated on clinical T3 tumors, since patients suffering from clinical T3 tumors are generally not scheduled for prostatectomy.

To translate model outcome to a useful input for radiotherapy treatment planning, we created three different risk levels for tumor presence based on PPV and NPV. PPV and NPV depend on the tumor voxel prevalence in a patient. To show the sensitivity of PPV and NPV for tumor voxel prevalence, we plotted PPV and NPV curves for a range of tumor voxel prevalences. Independent from tumor voxel prevalence a model outcome of >0.99 seems appropriate to define the GTV. Since the NPV curve does not depend much on tumor voxel prevalence for the range studied, a model outcome between 0.72 and 0.99 seems appropriate to define a high-risk CTV. Nevertheless, in the future, stratification thresholds values may be adapted for different patients groups based on T stage, Gleason score and PSA. In contrast to PPV and NPV, sensitivity and specificity values do not depend on tumor voxel prevalence. We therefore expect that similar model AUC values will be found in different patients independent of T stage, Gleason score and PSA. In conclusion, we developed a logistic regression model for the prediction of tumor presence on a voxel level in the PZ of the prostate. This model has a high diagnostic performance and enables objective interpretation of the functional MR images. The model output can be used to define different risk levels for tumor presence, which in turn could serve as an input for dose planning. In this way the robustness of tumor delineations for focal boost therapy of the prostate can be greatly improved.

5.5 Acknowledgement

This research is financially supported by the Dutch Cancer Society Grant No. UU-2009-4310.

CHAPTER 6

Histological properties of prostate tumors detected and non-detected with Magnetic Resonance Imaging

This chapter has been submitted as:
A. Borren[1], G. Groenendaal[1], M.R. Moman, A. Boeken-Kruger, P.J. van Diest, M. van Vulpen, M.E.P. Philippens and U.A. van der Heide Histological properties of prostate tumors detected and non-detected with Magnetic Resonance Imaging

Abstract
Background and Purpose: DWI and DCE-MRI can predict tumor presence on the voxel level. The diagnostic performance of these techniques is high. Nevertheless, some tumor voxels are not detected. In this study, the detectability of those voxels was related to the cell density (CD) and microvessel density (MVD) of the prostate tissue.
Material and Methods: Nine prostatectomy patients were included. All patients underwent a DWI and DCE-MRI exam. Based on these scans tumor probability was calculated. From H&E and CD31 stained slices, the CD and MVD for each voxel were calculated. The spread in MR and histopathological parameters was investigated. Furthermore, CD and MVD for detected and non-detected tumor voxels were compared using a Mann-Whitney U test.
Results: A large spread in MR and histopathological parameters was found within tumor tissue. Tumor voxels which could be detected with our logistic regression model had a significantly higher CD and MVD.
Conclusions: Tumor regions with a CD<3000 cells/mm^2 and a MVD<100 vessels/mm^2 are currently hard to detect. Tumor regions with high CD and MVD, which are likely to be the most aggressive parts, are likely to be detected and can be treated with higher dose.

1. These authors contributed equally to this work

6.1 Introduction

Evidence is emerging that local recurrences of prostate tumors are often seen at the original tumor site [15]. Therefore, an additional boost dose to this tumor could improve the tumor control probability. By limiting the boost to the visible tumor, toxicity to the organs at risk may be minimized [17, 40]. Recently, a randomized phase III trial was started to investigate the benefit of a focal lesion ablative microboost (FLAME trial) [4]. For such an approach, accurate delineation of the prostate tumor is required. Diffusion weighted imaging (DWI) and dynamic contrast-enhanced MRI (DCE-MRI) have a high sensitivity and specificity for tumor detection [20, 21]. However, two main challenges exist when using DWI and DCE-MRI in the radiotherapy clinic. First, due to heterogeneity of the tumor tissue, the performance of simple thresholding is insufficient. Second, on the voxel level the two modalities appear to provide inconsistent information about the presence of tumor [61]. To deal with these challenges, in a previous study, we created a logistic regression model based on DWI and DCE-MRI (chapter 5). This model had a high diagnostic performance (AUC = 0.89), but small tumor parts remained non-detectable with this model. Consequently, in a therapy setting, these tumor parts would not be included in a boost volume. The explanation for this may be found in the MR techniques DWI and DCE-MRI, which are believed to reflect the tissues cell density and microvasculature [34, 36, 37, 38]. Tumor tissue can be highly heterogeneous with regard to these characteristics, affecting detectability [39]. In this study, the detectability of the non-detected voxels was related to the cell density (CD) and microvessel density (MVD) of the prostate tissue.

6.2 Methods and Materials

6.2.1 Patients

Nine prostatectomy patients were included in this study (Table 6.1). This study was approved by the institutional review board and informed consent was obtained from all patients. Prior to prostatectomy all patients underwent a T2w, balanced TFE, DWI and DCE-MRI exam using a 3T Philips Achieva MR scanner. To prevent deformations of the prostate, we did not use an endorectal coil. Before the MR exam, a catheter was inserted into the urethra of the patients to facilitate registration of MR-images and histological slices.

6.2.2 Imaging

T2w images were acquired with a fast spin-echo sequence, TR/TE = 8396/120 ms, echo train length 13, acquisition matrix 256x256, FOV = 20 cm, slice thickness 3 mm, intersection gap 1 mm, number of slices 25. balanced TFE: TR/TE = 2.85/1.43 ms, acquisition matrix 192x249, FOV = 25 cm, slice thickness = 2 mm, number of slices 90. A 6-element phased array coil (sense cardiac) was used as receive coil during the scans. DWI scans were performed using a multislice single shot SE-EPI sequence (FOV = 38 cm, slice thickness = 3 mm, intersection gap = 1 mm, TR/TE=5000/54 ms, acquisition matrix = 152 x 107, EPI-factor = 47, 9 averages, phase encoding

Table 6.1: Patient characteristics

	Number of patients
Total	9
Primary tumor stage	
T1	0 (0%)
T2	4 (44%)
T3	5 (56%)
Gleason score	
6	3 (33%)
7	3 (33%)
8	3 (33%)
PSA level [ng/ml]	9.9 (6.3-29)
Age [years]	61 (48-74)

direction = PA, SENSE factor = 2, b values 300, 500, 1000 s/mm^2). The DCE-MRI protocol consisted of a 3D spoiled gradient echo sequence (20 transverse slices, 2.5 mm slice thickness, TR/TE=4/1 ms, flip angle 8, FOV = 40 cm, acquisition matrix = 160 x 160). Scans were repeated 120 times at 2.4s interval. A concentration of 0.1 ml/kg of Gadubutrol (1.0M) (Gadovist, Schering AG, Berlin, Germany) contrast was injected with 2 ml/s, followed by a saline flush. The tracer kinetics data were analyzed with the Tofts model, as described in [60] and yielded 3D K^{trans} parameter maps. The absolute values of K^{trans} depend on the arterial input function (AIF). Due to the extent of the measurement errors on the patient specific input functions, a generic arterial input function (AIF) was used for all patients. However, as a result, absolute K^{trans} values may not be comparable between patients. To overcome this, all K^{trans} maps were scaled to the median K^{trans} value in the peripheral zone (PZ), prior to inclusion in the model.

6.2.3 Registration between histopathology and MR images

After prostatectomy, we inserted three carbon rods in the prostate specimen to facilitate the registration process. Subsequently, we cut the prostate into slices of 3-4 mm. Finally, whole mount microscopic sections were cut from the macroscopic paraffin embedded slices. To compare the MR data with histopathology, the MR images were registered to the hematoxylin and eosin (H&E) stained sections. For the first 4 patients, the registration process was performed in three steps: 1. the registration of H&E stained slices to the macroscopic slices, 2. the reconstruction of the prostate from macroscopic slices, and 3. the registration between the prostate reconstruction and the T2w MR image. On average the registration error of this method was 2-3 mm [60]. For patients 5-9, the protocol was improved. The prostate was first embedded in agarose gel (5%). This allowed slicing the prostate in the same plane as on the T2w image. This improvement decreased the registration error with ∼0.5 mm. For

all patients, the registration error between the MR images and histopathology was on average about 1 voxel (2.5x2.5x2.5 mm^3).

6.2.4 Immunohistochemical vessel staining

Tissue sections were deparaffinized, endogenous peroxidase activity was blocked and antigen retrieval was performed. Sections were then incubated with an anti-CD31 monoclonal antibody (mouse-anti-human CD31, Novocastra). Subsequently, sections were incubated with HRP-conjugated secondary antibody (Novolink Polymer Detection System, Leica Microsystems) and diaminobenzidin (DAB) and then counterstained with hematoxylin. Throughout, appropriate positive and negative controls were used.

6.2.5 Cell and vessel segmentation

Digital whole slide images of three microscopic slices per patient were created as before [91]. Analysis of CD and MVD was performed in a grid of 2.5x2.5 mm^2. H&E stained sections were used for the determination of the CD by using the IHC Nuclear Algorithm v8 in ImageScope v10.0 (Aperio Technologies). Minimum detectable nuclear size was set at 20 μm. To identify CD31-stained blood vessels the Microvessel Analysis Algorithm v1 was used. The minimum vessel area threshold was set at 50 μm to ignore aspecific background staining. To compensate for variation in staining intensity, the settings of the algorithms were evaluated qualitatively and optimized for every batch by adjusting them on test regions.

6.2.6 Data analysis

Due to registration errors, voxels on the boundary between two groups (tumor vs. healthy or detected vs. non-detected tumor) are more likely to be misclassified. Therefore, for the visualization of the data in the scatter plots, we excluded voxels at the boundary to minimize the impact of registration errors. However, for data analysis all voxels were used. To illustrate the spread in the MR parameter maps, we plotted the ADC and K^{trans} values found in the pathological tumor voxels. By stratifying the logistic model outcome, three risk levels for tumor tissue were created in a previous study: non-suspicious, high-risk CTV and GTV (chapter 5). To test if the detectability of the tumor tissue depends on CD and MVD, we compared these histological parameters for the three different risk groups with a Mann-Whitney U test. P-values <0.05 were considered significant. For statistical analysis we used SPSS, version 16.0 (Chicago, IL, USA).

6.3 Results

Using the logistic regression model on our patient group about 87% of the tumor voxels was detected and 74% of the healthy tissue was correctly assigned as healthy tissue. A small part of the tumor tissue was incorrectly assigned as healthy tissue

Table 6.2: Cell density and microvessel density in tumor and healthy peripheral zone tissue

	mean [mm^{-2}]	standard deviation [mm^{-2}]
Tumor		
Cell density	3387	1194
Microvessel density	119	61
Healthy		
Cell density	2640	990
Microvessel density	89	43

(13%) (chapter 5). In tumor tissue the average ADC value was 1.1·10 mm^2/s and the average K^{trans} was 0.21 min^{-1}. The average ADC and K^{trans} values in healthy tissue were 1.2·10 mm^2/s and 0.15 min^{-1}, respectively. For a better comparison of K^{trans} values between patients, we normalized the K^{trans} on the median K^{trans} inside the PZ. On average, the median PZ K^{trans} is 0.15 min^{-1} (range 0.09-0.24 min^{-1}). This resulted in an average normalized K^{trans} of 1.5 in tumor and 1 in healthy tissue. The spread in ADC and normalized K^{trans} values in the pathological tumor voxels is shown in figure 6.1. Even if the boundary voxels are not taken into account, the spread on the data is large. In healthy tissue ADC and normalized K^{trans} values ranged between 4.0·10-1.9·10 mm^2/s and 0-3.69, respectively.

Figure 6.2A shows an H&E stained section of a prostate slice with two PZ tumor regions delineated in it. Figure 6.2B and 6.2C show the corresponding ADC and K^{trans} maps. The left tumor has on average a low ADC (0.93·10 mm^2/s) and a high normalized K^{trans} (3.2). However, some spread on these data was found. The right tumor consists of high ADC values (mean 1.2·10 mm^2/s) and low K^{trans} values (mean 1.1), associated with healthy tissue. Due to its low ADC and high K^{trans}, the left tumor was detected and even overestimated by the logistic regression model (figure 6.2D). In contrast, a large part of the right tumor was not detected by the logistic regression model. The two PZ tumors also differed on CD and MVD (2E and F). The left tumor consists of voxels with a high CD and MVD (mean CD: 5437 cells/mm^2, mean MVD: 241 vessels/mm^2), whereas the CD and MVD in the left tumor are low (mean CD: 2657 cells/mm^2, mean MVD: 99 vessels/mm^2). Similar results were found in all patients. In figure 6.3, all tumor voxels are divided based on the model predictions. The GTV and high-risk CTV group represent the tumor voxels that are detected by the model. The non-suspicious group represents the tumor voxels that are not detected by the model. The tumor voxels defined as GTV by the model have on average the highest CD and the tumor voxels that are not detected have the lowest CD (mean CD GTV: 4008, high-risk CTV: 3422, non-suspicious: 2922 cells/mm^2, figure 6.3a). These differences were all significant. The three groups differ also significantly on MVD. Mean MVDs are 143, 125 and 97 vessels/mm^2, for the GTV, high-risk CTV and non-suspicious regions respectively. In figure 6.4, we plotted the tumor

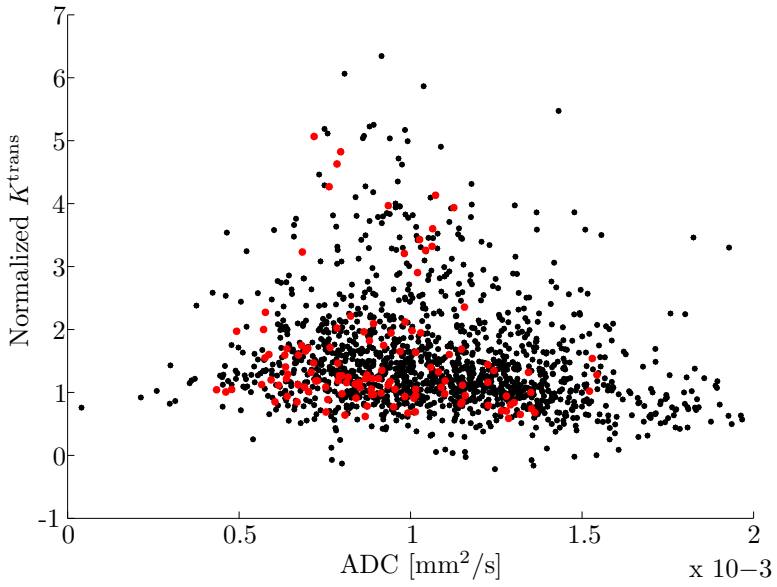

Figure 6.1: ADC and K^{trans} values inside the pathological tumor. To show the effect of the registration error, the voxels that are completely surrounded by tumor voxels in the transverse plane are plotted in red. These voxels are less likely to be incorrectly classified as tumor tissue.

voxels based on both CD and MVD. Most of the non-detected tumor voxels have low CD and MVD. These correspond to CDs and MVDs found in healthy tissue (Table 6.2). From the voxels with CDs and MVDs associated with healthy tissue (CD<3000 cells/mm^2 and MVD<100 vessels/mm^2) only 35% was detected by the model. These voxels contribute largely to the sensitivity limit of the model. From the voxels with a CD>3000 cells/mm^2, 81% was detected and from the voxels with a MVD >100 vessels/mm^2, 86% was detected. For higher CDs and MVDs the detection rate is even larger, up to 91% and 90% for a CD>4000 cells/mm^2 or a MVD>150 vessels/mm^2, respectively.

6.4 Discussion

Prostate tumor delineation is complicated by the large spread in ADC and K^{trans} values inside the tumor (figure 6.1). In a previous study we presented a model with a high diagnostic performance. However, when used for tumor delineation, parts of the tumor are not detected by the model. In the present study we show a significant difference in CD and MVD between detected and non-detected tumor parts. Non-detected tumor voxels contain on average a lower density of cells or microvessels (figures 6.3 and 6.4). These CDs and MVDs are similar to values associated with

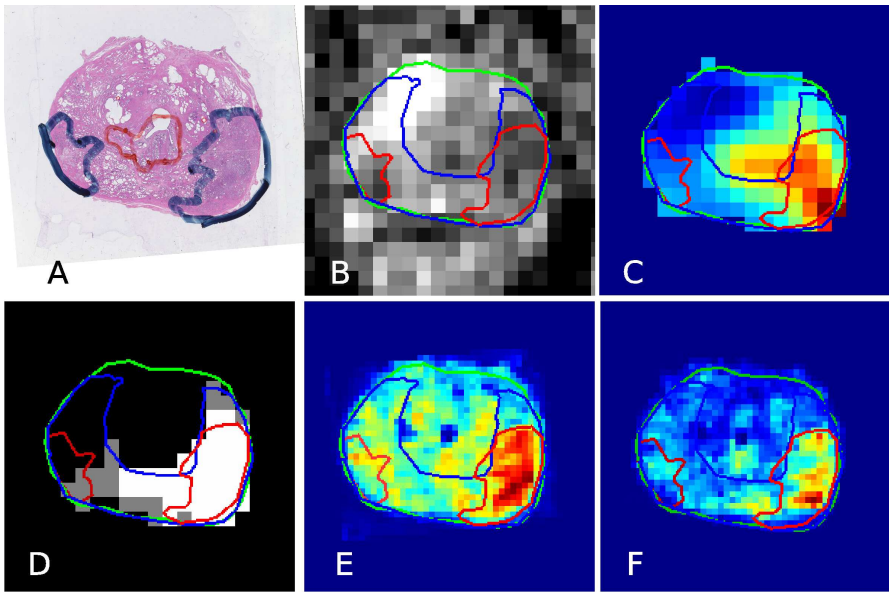

Figure 6.2: A. H&E stained section B. ADC map C. K^{trans} map D. stratified model outcome, where white is assigned to be GTV, gray is high-risk CTV and black is assigned to be non-suspicious E. cell density (for the image sampled on resolution of 1 x 1 mm^2) F. microvessel density. The tumor on the right side of the image is detected by the model and has a high cell and microvessel density. In contrast, the tumor on the left side of the image is not detected and has a low cell density and microvessel density. The tumor inside the central gland is not taken into account, since the model was created for peripheral zone cancers only.

healthy tissue (Table 6.2). From a radiobiological point of view, one could argue that tumor regions with a higher CD require higher radiation dose levels [92] and are therefore the most aggressive parts. This is in line with the association between ADC value and Gleason score [66, 67]. This suggests that the most aggressive tumor parts are preferentially detected by the model. The relation between MVD and required dose is more complicated. MVD appears to be a prognostic factor in many cancers. This property is associated with tumor growth and metastases. Furthermore, high-grade prostate tumors show a significantly larger MVD than low-grade tumors [58, 93]. However, the relation between tumor MVD and local blood flow depends largely on the structural abnormalities of the vascular network [94]. It is therefore unclear how MVD is related to radiosensitivity. Future studies are necessary to investigate dose-response in relation to imaging parameters.

In this study, histological properties are related to MR parameter maps on a voxel level. Such high resolution information about the relation between MR imaging and histology is important for dose painting. Previous studies have been performed, which

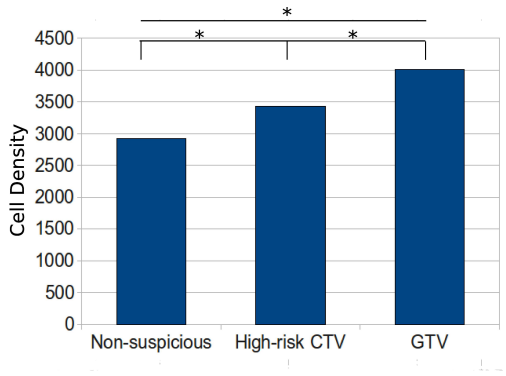

(a)

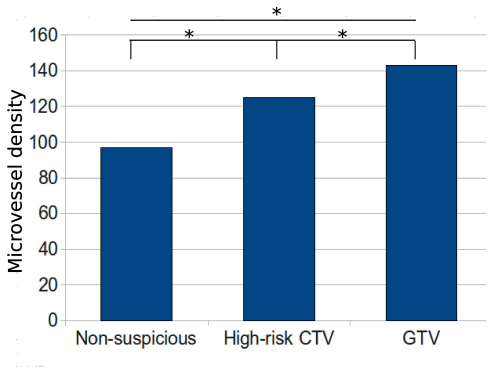

(b)

Figure 6.3: Cell density and microvessel density for different risk levels inside the pathological tumor (figure 6.3(a) and 6.3(b). Significant differences are marked with an '*'.

related histology with MR parameter maps on a regional or tumor level. Regions with a higher CD are correlated with low ADC and high K^{trans} values [34, 36, 95]. The relation between tumor CD and detectability based on ADC images was shown before on a regional level [39]. Qualitative parameters retrieved from the analysis of DCE-MRI signal-enhancement curves have been related with microvasculature of prostate tumor tissue [37, 38]. This research shows that tumor voxels with a CD<3000 cells/mm^2 and a MVD<100 vessels/mm^2 are hard to detect with our method (figure 6.4). Therefore, with the current MR and model protocol these regions could be considered as CTV. Given the high similarity in CD and MVD between tumor and healthy tissue (Table 6.2) it seems unlikely that all tumor voxels can be detected using the imaging techniques DWI and DCE-MRI. This study has some limitations. Our registration method is accurate and allowed comparison of MR images and H&E stained sections on a high resolution. However, the registration error between MR images and pathology of about one voxel, limits the number of tumor voxels that can be studied. Voxels on the boundary between detected tumor and non-detected

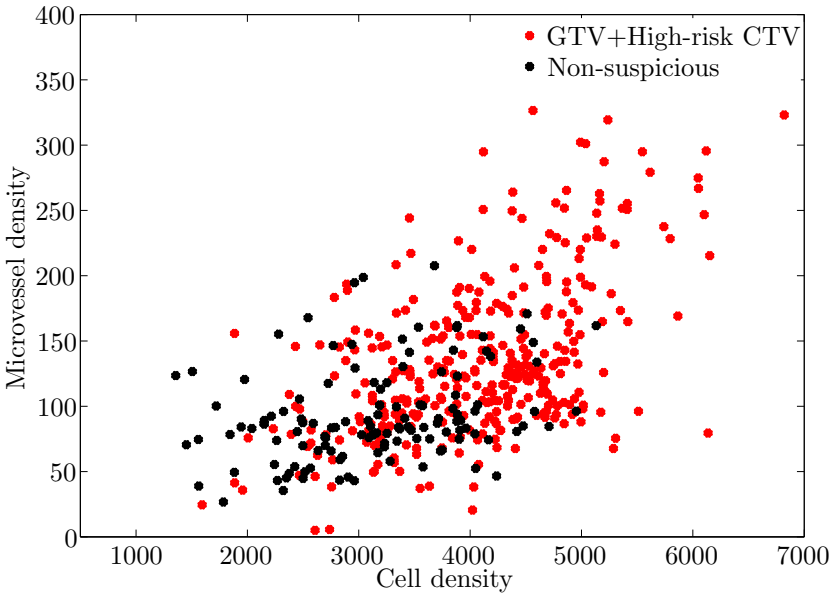

Figure 6.4: Cell density and microvessel density in the pathological tumor voxels. In black the voxels that are defined as non-suspicious by the model and in red the voxels that are defined as GTV or high-risk CTV. Voxels with a cell density >4000 cells/mm^2 are almost all assigned as GTV or high-risk CTV by the model. Similarly, voxels with a microvessel density of >150 vessels/mm^2 are almost all assigned as GTV or high-risk CTV by the model. Voxels with a low cell density or low microvessel density or both have a large chance not to be assigned as non-suspicious by the MR based logistic regression model. To circumvent that the registration error is reflected in the spread of the plotted data, we only plotted voxels from which all the neighboring voxels in the transverse plane are defined as the same group as the voxel itself (detected tumor tissue or non-detected tumor tissue).

tumor cannot reliably be compared with tissue characteristics. Furthermore, in this study, we compared model outcome with the tissue characteristics CD and MVD. However, these tissue characteristics do not fully explain the large spread in the data. An explanation for this might be the limited measurement precision of ADC and K^{trans}. Moreover, future research should focus on what tissue characteristics explain ADC and Ktrans values inside tumor tissue best.

In conclusion, we found a large heterogeneity inside prostate tumors on the histological level. This heterogeneity is reflected by the MR images. In this study we showed that tumor regions, with a CD<3000 cells/mm^2 and a MVD<100 vessels/mm^2 are hard to detect with the current MR protocol. Tumor regions with high CD (>4000 cells/mm^2)

and MVD (>150 vessels/mm^2), that are likely to be the most aggressive parts, are likely to be detected and can be treated with higher dose.

6.5 Acknowledgement

This research is financially supported by the Dutch Cancer Society Grant No. UU-2009-4310.

CHAPTER 7

Summary and General discussion

The introduction of IMRT, IGRT, fiducial markers and arc therapy have all contributed to an improvement of prostate radiotherapy [1, 96, 4, 6, 7, 97, 98]. These techniques allow the delivery of a high dose to the prostate, while limiting the dose to the organs at risk. A lot of research has been performed on how to accurately reach a proper dose distribution in the prostate [99, 100, 101, 102, 103]. However, much less is known about how dose distributions should be optimized for each different patient, based on tumor characteristics. Escalation of the prostate dose appears to have a beneficial effect on the biochemical outcome [11, 12, 13, 14]. However, this comes at the cost of an increased toxicity [14, 104, 12]. In the current clinical practice, the whole prostate is treated with a homogeneous dose. As a result the gross tumor volume (GTV), the microscopic tumor spread and the healthy prostate tissue all receive the same dose. At the same time, evidence is emerging that intraprostatic failures are mostly found at the location of the primary tumor [15, 16]. Further increase of the dose to the total prostate is in conflict with dose constraints to the organs at risk. To minimize the irradiation of healthy tissue, a focal boost to the GTV inside the prostate has been proposed [17, 18, 40]. This approach requires a proper delineation of the tumor inside the prostate.

The goal of this thesis was to investigate how functional MR imaging techniques can be used in a radiotherapy treatment setting in order to obtain robust tumor delineations inside the prostate. This thesis focused on the challenges which appear when these techniques are used prior to radiotherapy. We looked into the heterogeneity in ADC and K^{trans} values within and between patients. Different causes of these heterogeneities were identified and strategies were presented on how to deal with and benefit from these heterogeneities.

The voxel-wise consistency between DWI and DCE-MRI was the topic of chapter 2. In some patients this consistency was high. However, in most patients the overlap between suspicious lesions identified by both techniques, was limited, due to the large heterogeneity in ADC and K^{trans} values. The consequence of this is that a thresholding approach is too simple to derive prostate tumor delineations. It seems logical that both measurement errors and tissue heterogeneity contribute to the heterogeneity in ADC and K^{trans} values found in chapter 2. Although, heterogeneities in ADC and K^{trans} caused by measurement imprecision is unwanted, heterogeneity in these parameters caused by heterogeneity in tissue characteristics may be very advantageous in a radiotherapy setting. In this case, DWI and DCE-MRI may provide additional information about the underlying tissue characteristics and the dose required to kill all tumor cells in each individual voxel.

Although, at present studies are lacking that investigate the measurement precision of DWI and DCE-MRI on a voxel level, research has been done on the repeatability of the techniques. DWI repeatability on 3 Tesla was determined by Gibbs et al. This repeatability was ∼15% and 30% for the central gland and the peripheral zone, respectively [105]. The repeatability of DCE-MRI in the CG and PZ was studied by Kershaw et al [106]. A repeatability of 31% was found for K^{trans} in the PZ. Korporaal et al. found a slightly better repeatability on a voxel level (∼25% for a voxel volume of 0.15 cc) with DCE measurements on CT [107]. The voxel-wise repeatability of both DWI and DCE-MRI need to be further studied to investigate to what extent measurement errors contribute to the lack in overlap between the two techniques.

For prostate tumor delineation it is important how to deal with the heterogeneity in ADC and K^{trans} values. This heterogeneity may be decreased by future improvements of the DWI and DCE-MRI measurement protocols. A large challenge in DWI is its sensitivity to motion, which requires fast imaging. Echo-planar imaging (EPI) allows fast imaging and is the gold standard for clinical DWI. Unfortunately, this technique itself is prone to several artifacts [108]. The continuous phase-encoding scheme used in EPI results in a relatively low bandwidth in the phase encoding direction. As a result this technique is sensitive to B0 inhomogeneities, which may distort the image. Furthermore, diffusion gradient pulses can generate eddy currents, which result in ghosting and image distortion. Although large geometrical distortions were not found in the patients included in chapter 2, such deformations may occur in clinical practice, especially in the presence of rectal air. Measurement protocol improvements and post-processing to correct for B0 inhomogeneities and eddy currents may help to decrease image distortion in DWI and in this way the repeatability of the technique on a voxel level.

AIF measurement problems largely contribute to repeatabiltiy of DCE-MRI. Korporaal et al used CT measurements to show that day-to-day intrapatient variations in both AIF and tissue-enhancement are limited [109]. However, accurate measurement of the AIF is complicated on MR by the non-linear relationship between signal and contrast agent concentration, T2*-effects at higher concentrations, B1-field inhomogeneities and inflow-artifacts [79, 80, 81, 82, 83, 84]. Since the inter- and intrapatient variations in AIF characteristics range between 9.5-15.1% the use of a population-averaged AIF is advantageous when the measurement precision of an exam-specific

AIF is considerably worse than 15% [109]. In these situations the repeatability of K^{trans} maps is improved by using a population-averaged AIF.

An important step in the quantification process of DCE data may be in the derivation of the AIF from MR phase images [110, 111]. Korporaal et al. showed that CT based AIFs are similar to MR phase based AIFs. No significant differences were found in the CT based and MR based K^{trans} maps, when the corresponding AIFs were used as an input [112]. This indicates that quantitative DCE measurements on MR are possible.

The perceived consistency between the imaging modalities may be increased by optimization of measurement protocols. However, the tissue characteristics underlying DWI and DCE-MRI are very different. Therefore, as mentioned before, another explanation for the limited constistency between ADC and K^{trans} images is the tumor and normal tissue heterogeneity on cell and microvessel density. Prostate tissue is heterogeneous on these tissue characteristics, as shown in chapter 6. This heterogeneity was reflected by DWI and DCE-MRI parameters maps. This finding is in agreement, with what was found in other studies [34, 36, 37, 38, 39]. Due to heterogeneities in these tissue characteristics the two imaging modalities DWI and DCE-MRI will never provide completely consistent information about the presence of a target on a voxel level. Although, this may be seen as a disadvantage, the combination of the two techniques provide more extensive information about the tissue's aggressiveness [66, 67, 58, 93]. This may pave the road for a dose-painting by numbers approach. Nevertheless, for more classical radiation approaches, methods are necessary on how to deal with the perceived inconsistencies in a radiotherapy setting.

In this thesis, the use of different risk levels for tumor tissue is proposed to deal with heterogeneity in ADC and K^{trans} values. Using this approach, regions which are defined as suspicious by both ADC and K^{trans} are considered GTV. Regions where the two imaging modalities disagree are considered high-risk CTV. Different dose constraints can be given to the GTV, high-risk CTV and low-risk CTV. This pragmatic approach was further improved in chapter 5.

In addition to the perceived inconsistencies in the imaging modalities, the tumor delineation process is complicated by the use of prolonged androgen deprivation in many patients. In chapter 3 was shown that the diffusion in suspicious prostate tissue is significantly higher and perfusion is significantly lower after prolonged hormonal treatment. This resulted in lower tumor conspicuity. Nevertheless, in majority of patients (18/21), a suspicious lesion could be defined based on the MR images after prolonged androgen deprivation. However, due to the tissue changes after prolonged androgen deprivation, different imaging thresholds should be set in this situation to distinguish tumor from healthy tissue. A large percentage of the radiotherapy patients is treated with hormonal therapy. Therefore, it is important that even after prolonged androgen deprivation, suspicious lesions can be defined in the prostate, by adjusting threshold values.

For the validation of any delineation strategy, whole-mount histopathology is the gold standard. The registration accuracy needed to validate tumor delineations is much higher than the accuracy, which is needed when imaging is used for tumor detection purposes only. In chapter 4, a multi-step registration method was presented. Using

this approach the mean registration error between the MR images and histopathology was 2-3 mm. This is similar to the voxel sizes used in the DWI and DCE-MRI images. The achievement of this small registration error is important, since it allows for the voxel-wise validation of tumor delineations and prostate tissue characterization, which are the topics of chapters 5 and 6

So far tumor delineation in the prostate is a mainly manual procedure. However, to facilitate widespread application of DWI and DCE-MRI in the radiotherapy clinic, more robust and less observer dependent methods are required. Therefore, the approach presented in chapter 2 was further improved. In chapter 5 a logistic regression model was developed based on 87 radiotherapy patients. This model predicts the presence of tumor tissue on a voxel level inside the PZ. This model was validated in 12 prostatectomy patients. The model performance was consistent for the different patients and yielded an AUC of 0.89 when registration errors were compensated for. The model outcome was stratified to create different discrete levels for tumor presence: GTV, high-risk CTV and non-suspicious. These different risk levels could serve as an input for dose planning.

The stratification thresholds in chapter 5 are chosen for the purpose of focal boost strategies. In other treatment situations, other decisions may be made. In case of low-risk prostate cancer, one may consider not to treat the entire prostate. Also for salvage treatment, focal therapy may be a good option. Since in these two situations the prostate as a whole will not be treated, a threshold with a high NPV could be considered for the determination of the GTV.

The logistic regression model appears to be very promising in our own institute. For more widespread use an important next step would be to validate its performance in other radiotherapy clinics to investigate if the model performs consistently for other patients and measurement settings. The threshold values chosen to stratify the model are based on the tumor voxel prevalence in our prostatectomy patient group. It should be determined if different patient risk groups (e.g. based on PSA, Gleason score and T stage) require different threshold settings. Furthermore, further extension of the model seems valuable to make it applicable for a larger patient group.

First of all the model could be extended to the CG. At present the logistic regression model is only developed for PZ tumors, which account for 70% of all prostate tumors. Tumor delineation in the CG remains more challenging than tumor delineation in the PZ. BPH, commonly present in the CG of the prostate complicates the use of DCE-MRI in this area. Nevertheless, the combination of DWI and DCE-MRI may improve tumor detection in the CG [25]. Given the different tissue conditions in the CG compared to the PZ, the model cannot be directly used in the CG. Therefore, different parameter values will be necessary for tumor segmentation in this region.

Another important extension is hormonal treatment. At present the model is not applicable for patients undergoing hormonal therapy, which represent a large part of the prostate cancer patient population. From chapter 3, we know that prolonged androgen deprivation affects the prostate tumor conspicuity and that in this case different DWI and DCE-MRI thresholds are needed. Validation of delineation strategies in patients treated with hormonal therapy is complicated, since patients using hormonal therapy

are generally not considered good candidates for prostatectomy. However, when slow tumor growth is assumed, the tumor prediction model presented in chapter 5 could serve as a gold standard. One could compare pre-hormonal treatment MR scans with scans made at several time points during this treatment to adjust tumor prediction models for different durations of hormonal treatment.

The AUC of the logistic regression model presented in chapter 5 is high and therefore the model has a high diagnostic performance. However, when used for tumor delineation, parts of the tumor are not detected by the model. In chapter 6 was shown that detected tumor tissue had a significantly higher cell density and microvessel density than non-detected tumor parts. The cell densities and microvessel densities in non-detected tumor tissue are similar to values associated with healthy tissue (table 6.2). In this chapter we argued that tumor regions, that are likely the most aggressive parts, have a large chance to be detected and included in the boost volume.

This finding may be seen as a support to prescribe different dose levels depending on model outcome. Instead of looking in a binary way to the tissue as either being healthy or tumor, it is also possible to consider it as a continuum from healthy tissue to poorly differentiated tumor tissue. In addition, rather than interpreted as different tumor probabilities, the model outcome may be seen as a reflection of the heterogeneity in tumor tissue. Therefore, ADC and K^{trans} maps may serve as an input for a dose painting by numbers approach. At present accurate data is lacking on how to translate imaging parameters or tissue characteristics to required dose. Models exist, which relate tissue characteristics as clonogenic cell density and hypoxia, to tumor control probability [92, 113]. However, although cell density and microvessel density may be seen as derivatives from clonogenic cell density and hypoxia, the relation between these latter tissue characteristics and ADC and K^{trans} is uncertain. In combination with other parameter uncertainties existing in tumor control probability models, these models are not applicable in the current clinical practice.

To obtain optimal benefit from the tissue information reflected by DWI and DCE-MRI, more data needs to be required about the dose-effect relationship in different tumor regions. At present the Focal Lesion Ablative Microboost in Prostate Cancer (FLAME) trial has started. In the study arm of this trial an additional boost dose of 95 Gy is given to the macroscopic tumor within the prostate. The combination of previously acquired functional MR images, dose distributions and the location of recurrences will potentially provide insight in the dose-effect relationships for different types of tumor. This may help to create tumor aggressiveness maps, which may eventually serve as an input for dose painting by numbers.

In conclusion, in this thesis some of the important questions regarding the use of functional MR imaging for focal boost strategies in the prostate have been answered. Furthermore, approaches were presented to face challenges which arise when using DWI and DCE-MRI in a radiotherapy setting. In this way, this work may help to shift from the more classical homogeneous prostate dose distributions towards personalized approaches in which each prostate is treated based on its individual tumor characteristics.

CHAPTER 8

Nederlandse samenvatting

Introductie

Prostaatkanker is de meest voorkomende vorm van kanker bij mannen in Nederland. Door de vergrijzing en het toegenomen gebruik van prostaat specifiek antigen (PSA) als bloedmarker voor het opsporen van prostaatkanker zal het aantal mannen dat gediagnostiseerd wordt met prostaatkanker alleen maar verder toenemen. Een van de meest toegepaste behandelmethoden tegen prostaatkanker is radiotherapie. Bij radiotherapie wordt gebruik gemaakt van ioniserende straling. Patiënten worden in dagelijkse bestralingsfracties gedurende enkele opeenvolgende weken bestraald. Binnen de radiotherapie hebben de afgelopen jaren een aantal belangrijke ontwikkelingen plaatsgevonden. Door deze technische ontwikkelingen is het nu mogelijk heel gericht de vorm en de intensiteit van de stralingsbundel aan te passen aan het te bestralen gebied. Hierdoor kan een hogere stralingsdosis aan de prostaat gegeven worden terwijl de omliggende organen toch zo goed mogelijk gespaard kunnen blijven.
Ondanks dat de behandeling van prostaatkanker de afgelopen jaren sterk is verbeterd, sterven er nog altijd mannen aan de ziekte. Hoewel prostaattumoren doorgaans niet de hele prostaat beslaan, wordt gedurende de standaard therapie toch de hele prostaat met een homogene dosis bestraald. Prostaattumoren komen vaak terug op de plek waar de oorspronkelijke tumor heeft gezeten. Dit zou een reden zijn om de stralingsdosis op de prostaat nog verder te verhogen. Dit is echter niet mogelijk zonder ernstige bijwerkingen aan bijvoorbeeld het rectum te veroorzaken. Om deze reden is er door verschillende onderzoeksgroepen voorgesteld om naast de standaard stralingsdosis de dosis alleen nog verder te verhogen op het dominante tumorgebied in de prostaat (focal boost strategies).
Met de eerder genoemde nieuwe bestralingstechnieken is het goed mogelijk om lokaal

binnen de prostaat een hogere stralingsdosis af te geven. De uitdaging van focal boost strategies zit hem echter in het precies detecteren van de positie en vorm van de tumor. In dit proefschrift worden twee MRI technieken behandeld, die in aanmerking komen voor het bepalen van de positie en vorm van prostaattumoren: 1. diffusie gewogen MRI (DWI) en 2. dynamische contrastmiddel-versterkte MRI (DCE-MRI).
Met de eerste techniek kan de beweging van water in weefsel in beeld gebracht worden. Doordat tumorcellen veel dichter op elkaar gepakt zitten dan gezonde cellen kan water tussen tumorcellen veel minder vrij bewegen. Dit biedt de mogelijkheid om tumorgebieden op te sporen met behulp van DWI.
Met DCE-MRI kan informatie verkregen worden over de doorbloeding van weefsel. Doordat tumorweefsel snel groeit en hierbij veel voedingsstoffen nodig heeft, worden er door het lichaam veel nieuwe bloedvaten aangelegd naar de tumor toe. Deze bloedvaten zijn vaak van een mindere kwaliteit dan gewone bloedvaten. Dit resulteert in verschillen in doorbloeding tussen gezond en tumorweefsel. DCE-MRI biedt de mogelijkheid om deze verschillen op te sporen.
DWI en DCE-MRI worden al langer in de diagnostiek gebruikt. Het gebruik van deze technieken in een radiotherapie omgeving zorgt echter voor uitdagingen, die voor de diagnostiek veel minder relevant zijn. In de diagnostische setting moet de vraag beantwoord worden of een patiënt al dan niet prostaatkanker heeft. Op het moment dat een patiënt naar de radiotherapie afdeling komt is deze vraag al beantwoord. Bij toepassing van radiotherapie is het echter niet alleen belangrijk om te weten dat een patiënt prostaatkanker heeft, de precieze locatie en vorm van de tumor is voor de behandeling ook erg belangrijk. Dit houdt in dat voor ieder klein subvolume in de prostaat bekeken moet worden of er wel of geen tumor aanwezig. Hiervoor is informatie met een veel hogere resolutie vereist dan in de diagnostische setting.
Een ander belangrijk verschil is dat veel patiënten die op een radiotherapie afdeling komen al behandeld worden met hormonen. Deze hormonen beïnvloeden mogelijkerwijs de zichtbaarheid van tumorweefsel in de prostaat. Hierdoor is er waarschijnlijk een andere strategie nodig om bij deze patiënten tumoren te omlijnen/intekenen dan bij patiënten zonder hormonale therapie.
In dit proefschrift wordt behandeld hoe DWI en DCE-MRI kunnen worden gebruikt in een radiotherapie omgeving om tot robuuste tumorintekeningen te komen, welke kunnen worden gebruikt als input voor het plannen van een bestralingsbehandeling.

Hoofdstuk 2 - Het gelijktijdig gebruik van DWI en DCE-MRI voor het intekenen van prostaattumoren

Uit de literatuur is gebleken dat DWI en DCE-MRI veel tumoren kunnen detecteren. Het is alleen niet duidelijk welke drempelwaarde voor beide technieken gebruikt zou moeten worden om tumor van gezond weefsel te onderscheiden. Verder is het zo dat DWI is gerelateerd aan celdichtheid en DCE-MRI aan doorbloeding. Ondanks dat tumorweefsel over het algemeen een hogere celdichtheid heeft dan gezond weefsel, is het niet zo dat elk weefsel met een hoge celdichtheid tumor is en dat weefsel met een lage celdichtheid geen tumor kan bevatten. Hetzelfde geldt voor bloedvaten. Het

gevolg hiervan is, dat als DWI en DCE-MRI gecombineerd worden om tot een tumorintekening te komen, dit kan leiden tot conflicterende informatie over de aanwezigheid van tumor. In hoofdstuk 2 is onderzocht in welke mate DWI en DCE-MRI op detailniveau dezelfde voorspelling geven over de aanwezigheid van tumor.
Bij sommige patiënten is de overeenkomst tussen beiden technieken groot. Echter bij de meeste patënten is de overeenkomst tussen beide technieken gering. Het ligt voor de hand dat zowel MRI meetfouten als verschillen in cel- en vaatdichtheden in het prostaatweefsel bijdragen in de verschillen in voorspellingen tussen DWI en DCE-MRI. Uiteraard zijn verschillen tussen DWI en DCE-MRI, die voortkomen uit meetfouten niet wenselijk. Als de verschillen tussen DWI en DCE-MRI een reflectie zijn van cel- en vaateigenschappen in prostaatweefsel, betekent het gebruik van beide technieken een groot voordeel voor de radiotherapiebehandeling. Zowel tumorceldichtheid als doorbloeding bepalen namelijk de dosis die nodig is om alle tumorcellen te doden.

Hoofdstuk 3 - Het effect van hormonale therapie op de zichtbaarheid van prostaattumoren

Veel patiënten krijgen naast radiotherapie ook hormonale therapie ter behandeling van prostaatkanker. Deze therapie heeft echter mogelijk invloed op de zichtbaarheid van de tumoren op MRI beelden. Met betrekking tot de radiotherapiebehandeling zijn drie vragen belangrijk ten aanzien van het gebruik van hormonale therapie voor het maken van DWI en DCE-MRI beelden. 1. Heeft het langdurig gebruik van hormonen invloed op de zichtbaarheid van tumoren op DWI en DCE-MRI beelden? 2. Kunnen tumoren nog ingetekend worden na langdurig gebruik van hormonale therapie? 3. Zijn er andere drempelwaardes nodig bij hormonale therapie patiënten dan bij andere patiënten om met behulp van DWI en DCE-MRI tumor van gezond weefsel te onderscheiden?
In hoofdstuk 3 blijkt dat bij patiënten, die langdurig hormonale therapie hebben gebruikt de diffusie van water in tumoren hoger is en de doorbloeding lager is. Hierdoor lijkt het tumorweefsel meer op gezond prostaatweefsel. Dit zorgt er weer voor dat tumoren bij patiënten die langdurig hormonale therapie gebruikt hebben moeilijker te onderscheiden zijn. Gelukkig is het nog wel steeds mogelijk om tumoren in te tekenen bij de meeste patiënten die langdurig hormonale therapie hebben ondergaan. Hiervoor moet echter wel gekozen worden voor andere drempelwaardes voor DWI en DCE-MRI om tumor van gezond weefsel te onderscheiden.

Hoofdstuk 4 - Vergelijking van DWI en DCE-MRI beelden met histopathologie

De enige manier om echt te weten wat DWI en DCE-MRI beelden laten zien, is door deze te vergelijken met wat er in het prostaatweefsel (histopathologiedata) te zien is. Bij radiotherapie patiënten is dit niet mogelijk, omdat deze patiënten niet geopereerd worden. Het is echter wel mogelijk om de vergelijking tussen MRI beelden en

prostaatweefsel bij een andere patiëntgroep uit te voeren: de prostatectomy patiëntgroep, ofwel de patiënten bij wie de prostaat verwijderd wordt. Omdat het voor radiotherapie belangrijk is om van elk klein subvolume te weten of er wel of geen tumor zit, moet het matchen tussen MRI beelden en prostaatweefsel nauwkeurig gebeuren. In hoofdstuk 4 wordt een manier gepresenteerd waarbij met tussenstappen MRI beelden en prostaatweefsel met een nauwkeurigheid van 2.5 mm op elkaar gematcht kunnen worden. Deze hoge nauwkeurigheid maakt het mogelijk om tumorintekeningen op MRI beelden te vergelijken met tumorintekeningen, die na de operatie zijn gemaakt door de patholoog op het prostaatweefsel. Op deze manier kan onderzocht worden hoe nauwkeurig prostaattumoren nu eigenlijk ingetekend kunnen worden met behulp van MRI. Ook kan het helpen om bestaande methodes voor het intekenen van prostaattumoren verder te verbeteren.

Hoofdstuk 5 - Wiskundig model voor het intekenen van prostaattumoren

In de huidige klinische praktijk worden prostaattumoren handmatig ingetekend door de radiotherapeut en radioloog aan de hand van alle beschikbare beelden en klinische informatie. Voor een meer wijdverbreid gebruik van DWI en DCE-MRI in de radiotherapie zijn objectievere en robuustere methodes om tot een tumorintekening te komen wenselijk. In hoofdstuk 5 wordt een wiskundig model gepresenteerd waarmee er per subvolume in de prostaat bepaald kan worden of er al dan niet tumor aanwezig is. Dit model is gevalideerd met eerder beschreven histopathologiedata van de prostaat. Dit model presteert consistent voor alle 12 geteste patiënten en heeft bij deze patiënten een hoge voorspellende waarde. De uitkomst van het model ligt tussen 0 en 1, waarbij 0 een lage kans op tumor en 1 een hoge kans op tumor betekent. Om het model geschikt te maken als input voor bestralingsplannen worden alle prostaatsubvolumes ingedeeld in drie categorieën: 1. zeer waarschijnlijk geen tumor 2. redelijke kans op tumor 3. zeer waarschijnlijk wel tumor.

Hoofdstuk 6 - Weefseleigenschappen van tumoren die wel en niet door het wiskundig model gedetecteerd worden

Het model beschreven in hoofdstuk 5 heeft een hoge voorspellende waarde. Er worden met dit model echter nog altijd delen van de tumor gemist. Een verklaring hiervoor zou kunnen zitten in de MRI technieken waar het model gebruik van maakt. Zoals eerder beschreven laten DWI en DCE-MRI niet direct de aanwezigheid van tumor zien, maar wordt er aangenomen dat zij een beeld geven van de celdichtheid en doorbloeding van weefsel. Deze weefseleigenschappen kunnen heel erg variëren binnen een tumor, wat invloed heeft op de zichtbaarheid van het tumorweefsel. In hoofdstuk 6 wordt gekeken of tumorweefsel, dat gemist wordt door het model op weefselniveau verschilt van tumorweefsel dat wel gevonden wordt met het model. Dit blijkt inderdaad het geval te zijn. Tumorgebieden die gevonden kunnen worden met het model hebben een hogere cel- en bloedvatdichtheid dan tumorgebieden, die niet gevonden kunnen

worden. Een duidelijk voorbeeld hiervan is te zien in figuur 6.2. Deze figuur toont in A. de histopathologieinformatie, waarop de tumoren door de patholoog zijn ingetekend. B. laat een DWI beeld zien, C. een DCE-MRI beeld. Hieruit volgt de modeluitkomst in plaatje D. De tumor aan de rechterkant van het beeld is duidelijk wel gevonden, terwijl de linkertumor vrijwel volledig gemist is. Figuur E. geeft de bijbehorende celdichtheid en F de bloedvatdichtheid. Hierin is duidelijk een groot verschil in cel- en bloedvatdichtheid tussen de linker- en rechtertumor te zien. Dit is een belangrijke bevinding voor radiotherapie. Er zijn namelijk aanwijzingen dat tumoren met een hogere cel- en bloedvatdichtheid agressiever zijn en meer stralingsdosis nodig hebben. Omdat deze stukken tumor ook gevonden worden met het model, zouden zij bij focal boost strategies in het extra hoge dosisgebied vallen.

Conclusie

In dit proefschrift worden een aantal belangrijke vragen omtrent het gebruik van DWI en DCE-MRI in de radiotherapie behandeld. Er worden methodes gepresenteerd om om te gaan met verschillende uitdagingen van het gebruik van deze technieken voor radiotherapie. Hiermee kan dit werk bijdragen aan een verschuiving van de klassiekere radiotherapie waarin iedere prostaat wordt bestraald met een homogene stralingsdosis naar een meer gepersonaliseerde benadering waarin iedere prostaat wordt bestraald op basis van de specifieke tumorkarakteristieken.

References

[1] E Vigneault, J Pouliot, J Laverdière, J Roy, and M Dorion. Electronic portal imaging device detection of radioopaque markers for the evaluation of prostate position during megavoltage irradiation: a clinical study. *Int. J. Radiat. Oncol. Biol. Phys.*, 37(1):205–212, 1997.

[2] A J Nederveen, H Dehnad, U A Van der Heide, R J A Van Moorselaar, P Hofman, and J J W Lagendijk. Comparison of megavoltage position verification for prostate irradiation based on bony anatomy and implanted fiducials. *Int. J. Radiat. Oncol. Biol. Phys.*, 2002. (submitted).

[3] A N T J Kotte, P Hofman, J J W Lagendijk, M Van Vulpen, and U A Van der Heide. Intrafraction motion of the prostate during external-beam radiation therapy: analysis of 427 patients with implanted fiducial markers. *Int. J. Radiat. Oncol. Biol. Phys.*, 69(2):419–425, 2007.

[4] U A Van der Heide, A N T J Kotte, H Dehnad, P Hofman, J J W Lagendijk, and M Van Vulpen. Analysis of fiducial marker-based position verification in the external beam radiotherapy of patients with prostate cancer. *Radiotherapy and Oncology*, 82(1):38–45, 2007.

[5] T F Mutanga, H C J De Boer, G J Van der Wielen, D Wentzler, J Barnhoorn, L Incrocci, and B J M Heijmen. Stereographic targeting in prostate radiotherapy: Speed and precision by daily automatic positioning corrections using kilovoltage/megavoltage image pairs. *Int. J. Radiat. Oncol. Biol. Phys.*, 71:1074–1083, 2008.

[6] C Burman, C S Chui, G Kutcher, S Leibel, M Zelefsky, T LoSasso, S Spirou, Q Wu, J Yang, J Stein, R Mohan, Z Fuks, and C C Ling. Planning, delivery, and quality assurance of intensity-modulated radiotherapy using dynamic multileaf collimator: a strategy for large-scale implementation for the treatment of carcinoma of the prostate. *Int. J. Radiat. Oncol. Biol. Phys.*, 39(4):863–873, 1997.

[7] M J Zelefsky, Z Fuks, M Hunt, Y Yamada, Marion, C C Ling, H Amols, E S Venkatraman, and S A Leibel. High-dose intensity modulated radiation therapy for prostate cancer: early toxicity and biochemical outcome in 772 patients. *Int. J. Radiat. Oncol. Biol. Phys.*, 53(5):1111–1116, 2002.

[8] I Lips, H Dehnad, A Boeken Kruger, J van Moorselaar, U van der Heide, J Battermann, and M van Vulpen. Health-related quality of life in patients with locally advanced prostate cancer after 76 gy intensity-modulated radiotherapy vs. 70 gy conformal radiotherapy in a prospective and longitudinal study. *Int. J. Radiat. Oncol. Biol. Phys.*, 69(3):656–661, 2007.

[9] I M Lips, C H van Gils, U A van der Heide, A E Boeken Kruger, and M van Vulpen. Health-related quality of life 3 years after high-dose intensity-modulated radiotherapy with gold fiducial marker-based position verification. *BJU Int.*, 103(6):762–767, 2009.

[10] *www.ikcnet.nl*.

[11] S T H Peeters, W D Heemsbergen, P C M Koper, W L J Van Putten, A Slot, M F H Dielwart, J M G Bonfrer, L Incrocci, and J V Lebesque. Dose-response in radiotherapy for localized prostate cancer: results of the Dutch multicenter randomized phase III trial comparing 68 Gy of radiotherapy with 78 Gy. *J. Clin. Oncol.*, 24(13):1990–1996, 2006.

[12] A Pollack, G K Zagars, G Starkschall, J A Antolak, J J Lee, E Huang, A C von Eschenbach, D A Kuban, and I Rosen. Prostate cancer radiation dose response: results of the M. D. Anderson phase III randomized trial. *Int. J. Radiat. Oncol. Biol. Phys.*, 53(5):1097–1105, 2002.

[13] A L Zietman, M L DeSilvio, J D Slater, C J Rossi, D W Miller, J A Adams, and W U Shipley. Comparison of conventional-dose vs high-dose conformal radiation therapy in clinically localized adenocarcinoma of the prostate: a randomized controlled trial. *JAMA*, 294(10):1233–1239, 2005.

[14] A Al-Mamgani, W L J Van Putten, W D Heemsbergen, G J L H Van Leenders, A Slot, M F H Dielwart, L Incrocci, and J V Lebesque. Update of dutch multicenter dose-escalation trial of radiotherapy for localized prostate cancer. *Int. J. Radiat. Oncol. Biol. Phys.*, 72(4):980–988, 2008.

[15] N Cellini, A G Morganti, G C Mattiucci, V Valentini, M Leone, S Luzi, R Manfredi, N Dinapoli, C Digesu', and D Smaniotto. Analysis of intraprostatic failures in patients treated with hormonal therapy and radiotherapy: implications for conformal therapy planning. *Int. J. Radiat. Oncol. Biol. Phys.*, 53(3):595–599, 2002.

[16] D Pucar, H Hricak, A Shukla-Dave, K Kuroiwa, M Drobnjak, J Eastham, P T Scardino, and Zelefsky M J. Clinically significant prostate cancer local recurrence after radiation therapy occurs at the site of primary tumor: magnetic resonance imaging and step-section pathology evidence. *Int. J. Radiat. Oncol. Biol. Phys.*, 69(1):62–9, 2007.

[17] B Pickett, E Vigneault, J Kurhanewicz, L Verhey, and M Roach. Static field intensity modulation to treat a dominant intra-prostatic lesion to 90 Gy compared to seven field 3-dimensional radiotherapy. *Int. J. Radiat. Oncol. Biol. Phys.*, 43(4):921–929, 1999.

[18] E N J T Van Lin, J J Fütterer, S W T P J Heijmink, L P Van der Vight, A L Hoffmann, P Van Kollenburg, H J Huisman, T W J Scheenen, J A Witjes, J W Leer, J O Barentsz, and A G Visser. IMRT boost dose planning on dominant intraprostatic lesions: gold marker-based three-dimensional fusion of CT with dynamic contrast-enhanced and 1H-spectroscopic MRI. *Int. J. Radiat. Oncol. Biol. Phys.*, 65(1):291–303, 2006.

[19] F A Van Dorsten, M van der Graaf, M R W Engelbrecht, G J L H van Leenders, A Verhofstad, M Rijpkema, J J M C H de la Rosette, J O Barentsz, and A Heerschap. Combined quantitative dynamic contrast-enhanced MR imaging an 1H MR spectroscopic imaging of human prostate cancer. *J. Magn. Reson. Imaging*, 20:279–287, 2004.

[20] J J Fütterer, S W T P J Heijmink, T W J Scheenen, J Veltman, H J Huisman, P Vos, C A Hulsbergen-Van de Kaa, J A Witjes, P F M Krabbe, A Heerschap, and J O Barentsz. Prostate cancer localization with dynamic contrast-enhanced MR imaging and proton MR spectroscopic imaging. *Radiology*, 241(2):449–458, 2006.

[21] K Hosseinzadeh and S D Schwarz. Endorectal diffusion-weighted imaging in prostate cancer to differentiate malignant and benign peripheral zone tissue. *J. Magn. Reson. Imaging*, 20(4):654–661, 2004.

[22] C Sato, S Naganawa, T Nakamura, H Kumada, S Miura, O Takizawa, and T Ishigaki. Differentiation of noncancerous tissue and cancer lesions by apparent diffusion coefficient values in transition and peripheral zones of the prostate. *J. Magn. Reson. Imaging*, 21(3):258–262, 2005.

[23] H Miao, H Fukatsu, and T Ishigaki. Prostate cancer detection with 3-T MRI: comparison of diffusion-weighted and T2-weighted imaging. *Eur. J. Radiol.*, 61(2):297–302, 2007.

[24] P K Agarwal, N Sadetsky, B R Konety, M I Resnick, P R Carroll, and Cancer of the Prostate Strategic Urological Research Endeavor (CaPSURE). Treatment failure after primary and salvage therapy for prostate cancer: likelihood, patterns of care, and outcomes. *Cancer*, 112(2):307–314, 2008.

[25] A Oto, A Kayhan, Y Jiang, M Tretiakova, C Yang, T Antic, F Dahi, A L Shalhav, G Karczmar, and W M Stadler. Prostate cancer: differentiation of central gland cancer from benign prostatic hyperplasia by using diffusion-weighted and dynamic contrast-enhanced mr imaging. *Radiology*, 257(3):715–723, 2010.

[26] M D Pickles, P Gibbs, M Sreenivas, and L W Turnbull. Diffusion-weighted imaging of normal and malignant prostate tissue at 3.0T. *J. Magn. Reson. Imaging*, 23(2):130–134, 2006.

[27] P Gibbs, M D Pickles, and L W Turnbull. Diffusion imaging of the prostate at 3.0 tesla. *Invest. Radiol.*, 41(2):185–188, 2006.

[28] V Kumar, N R Jagannathan, Kumar R, Thulkar S, S D Gupta, S N Dwivedi, A K Hemal, and N P Gupta. Apparent diffusion coefficient of the prostate in men prior to biopsy: determination of a cut-off value to predict malignancy of the peripheral zone. *NMR Biomed.*, 20(5):505–511, 2007.

[29] T Franiel, L Lüdemann, B Rudolph, H Rehbein, A Staack, M Taupitz, D Prochnow, and B Beyersdorff. Evaluation of normal prostate tissue, chronic prostatitis, and prostate cancer by quantitative perfusion analysis using a dynamic contrast-enhanced inversion-prepared dual-contrast gradient echo sequence. *Invest. Radiol.*, 43(7):481–487, 2008.

[30] P Kozlowski, S D Chang, E C Jones, K W Berean, H Chen, and S L Goldenberg. Combined diffusion-weighted and dynamic contrast-enhanced MRI for prostate cancer diagnosis–correlation with biopsy and histopathology. *J. Magn. Reson. Imaging*, 24(1):108–113, 2006.

[31] I Ocak, M Bernardo, G Metzger, T Barrett, P Pinto, P S Albert, and P L Choyke. Dynamic contrast-enhanced MRI of prostate cancer at 3 T: a study of pharmacokinetic parameters. *Am. J. Roentgenol.*, 189(4):849, 2007.

[32] R Alonzi, A R Padhani, N J Taylor, D J Collins, J A D'Arcy, J J Stirling, M I Saunders, and P J Hoskin. Antivascular effects of neoadjuvant androgen deprivation for prostate cancer: An in vivo human study using susceptibility and relaxivity dynamic mri. *Int. J. Radiat. Oncol. Biol. Phys.*, 2010.

[33] A R Padhani, A D MacVicar, C J Gapinski, D P Dearnaley, G J Parker, J Suckling, M O Leach, and J E Husband. Effects of androgen deprivation on prostatic morphology and vascular permeability evaluated with mr imaging. *Radiology*, 218(2):365–374, 2001.

[34] J Xu, P A Humphrey, A S Kibel, A Z Snyder, V R Narra, J J H Ackerman, and S Song. Magnetic resonance diffusion characteristics of histologically defined prostate cancer in humans. *Magn. Reson. Med.*, 2009.

[35] P Gibbs, G P Liney, M D Pickles, B Zelhof, G Rodrigues, and L W Turnbull. Correlation of adc and t2 measurements with cell density in prostate cancer at 3.0 tesla. *IR*, 44(9):572–576, 2009.

[36] B Zelhof, M Pickles, G Liney, P Gibbs, G Rodrigues, S Kraus, and L Turnbull. Correlation of diffusion-weighted magnetic resonance data with cellularity in prostate cancer. *BJUI*, 103(7):883–888, 2009.

[37] H P Schlemmer, J Merkle, R Grobholz, T Jaeger, M S Michel, A Werner, J Rabe, and G van Kaick. Can pre-operative contrast-enhanced dynamic mr imaging for prostate cancer predict microvessel density in prostatectomy specimens? *Eur. Radiol.*, 14(2):309–317, 2004.

[38] J Ren, Y Huan, H Wang, Y J Chang, H T Zhao, Y L Ge, Y Liu, and Y Yang. Dynamic contrast-enhanced mri of benign prostatic hyperplasia and prostatic carcinoma: correlation with angiogenesis. *Clin. Radiol.*, 63(2):153–159, Feb 2008.

[39] D L Langer, T H Van der Kwast, A J Evans, L Sun, M J Yaffe, J Trachtenberg, and M A Haider. Intermixed normal tissue within prostate cancer: effect on MR imaging measurements of apparent diffusion coefficient and T2–sparse versus dense cancers. *Radiology*, 249(3):900–908, 2008.

[40] A K Singh, P Guion, N Sears-Crouse, K Ullman, S Smith, P S Albert, G Fichtinger, P L Choyke, S Xu, J Kruecker, B J Wood, A Krieger, and H Ning. Simultaneous integrated boost of biopsy proven, MRI defined dominant intra-prostatic lesions to 95 Gray with IMRT: early results of a phase I NCI study. *Radiat. Oncol.*, 2:36, 2007.

[41] A R Padhani, C J Gapinski, D A Macvicar, G J Parker, J Suckling, P B Revell, M O Leach, D P Dearnaley, and J E Husband. Dynamic contrast enhanced MRI of prostate cancer: correlation with morphology and tumour stage, histological grade and PSA. *Clin Radiol*, 55(2):99–109, 2000.

[42] S White, H Hricak, R Forstner, J Kurhanewicz, D B Vigneron, C J Zaloudek, J M Weiss, P Narayan, and P R Carroll. Prostate cancer: effect of postbiopsy hemorrhage on interpretation of MR images. *Radiology*, 195:385–390, 1995.

[43] J Scheidler, H Hricak, D B Vigneron, K K Yu, D L Sokolov, L R Huang, C J Zaloudek, S J Nelson, P R Carroll, and J Kurhanewicz. Prostate cancer: localization with three-dimensional proton MR spectroscopic imaging - clinicopathologic study. *Radiology*, 213:473–480, 1999.

[44] M A Haider, T H van der Kwast, J Tanguay, A J Evans, A-T Hashmi, G Lockwood, and

J Trachtenberg. Combined t2-weighted and diffusion-weighted MRI for localization of prostate cancer. *American Journal of Roentgenology*, 189:323–328, 2007.

[45] A R Padhani. Dynamic contrast-enhanced mr in clinical oncology: current status and future directions. *J. Magn. Reson. Imaging*, 16:407–422, 2002.

[46] D L Buckley, C Roberts, G J M Parker, J P Logue, and C E Hutchinson. Prostate cancer: evaluation of vascular characteristics with dynamic contrast-enhanced T1-weighted MR imaging – initial experience. *Radiology*, 233:709–715, 2004.

[47] A R Padhani, G Liu, D M Koh, T L Chenevert, H C Thoeny, T Takahara, A Dzik-Jurasz, B D Ross, M Van Cauteren, D Collins, D A Hammoud, G J S Rustin, B Taouli, and P L Choyke. Diffusion-weighted magnetic resonance imaging as a cancer biomarker: consensus and recommendations. *Neoplasia*, 11(2):102–125, Feb 2009.

[48] S Pauls, F M Mottaghy, S A Schmidt, S Krger, P Mller, H Brambs, and A Wunderlich. Evaluation of lung tumor perfusion by dynamic contrast-enhanced mri. *MRI*, 26(10):1334–1341, Dec 2008.

[49] M Palmowski, I Schifferdecker, S Zwick, S Macher-Goeppinger, H Laue, A Haferkamp, H Kauczor, F Kiessling, and P Hallscheidt. Tumor perfusion assessed by dynamic contrast-enhanced mri correlates to the grading of renal cell carcinoma: Initial results. *EJR*, Jun 2009.

[50] E K Fram, R J Herfkens, G A Johnson, G H Glover, J P Karis, A Shimakawa, T G Perkins, and N J Pelc. Rapid calculation of T1 using variable flip angle gradient refocused imaging. *Magn. Reson. Med.*, 5(3):201–208, 1987.

[51] S Klein, M Staring, K Murphy, M A Viergever, and J P W Pluim. Elastix: a toolbox for intensity-based medical image registration. *IEEE Trans. Med. Imaging*, 29(1):196–205, 2010.

[52] M Rohrer, H Bauer, J Mintorovitch, M Requardt, and H J Weinmann. Comparison of magnetic properties of mri contrast media solutions at different magnetic field strengths. *IR*, 40(11):715–724, Nov 2005.

[53] P S Tofts, G Brix, D L Buckley, J L Evelhoch, E Henderson, M V Knopp, H B W Larsson, T-Y Lee, N A Mayr, G J M Parker, R E Port, J Taylor, and R M Weisskoff. Estimating kinetic parameters from dynamic contrast-enhanced T1-weighted MRI of a diffusable tracer: standardized quantities and symbols. *J. Magn. Reson. Imaging*, 10:223–232, 1999.

[54] K Murase. Efficient method for calculating kinetic parameters using T1-weighted dynamic contrast-enhanced magnetic resonance imaging. *Magn. Reson. Med.*, 51(4):858–862, 2004.

[55] D G Norris and T Niendorf. Interpretation of dw-nmr data: dependence on experimental conditions. *NMRBio*, 8(7-8):280–288, 1995.

[56] H Park, M R Piert, A Khan, R Shah, H Hussain, J Siddiqui, T L Chenevert, and C R Meyer. Registration methodology for histological sections and in vivo imaging of human prostate. *AR*, 15(8):1027–1039, Aug 2008.

[57] S M Bentzen. Theragnostic imaging for radiation oncology: dose-painting by numbers. *Lancet Oncol.*, 6:112–117, 2005.

[58] N Weidner. Intratumor microvessel density as a prognostic factor in cancer. *Am. J. Physiol.*, 147(1):9–19, 1995.

[59] R Miralbell, M Moll, M Rouzaud, A Hidalgo, J Ignacio Toscas, J Lozano, S Sanz, C Ares, S Jorcano, D Linero, and L Escud. Hypofractionated boost to the dominant tumor region with intensity modulated stereotactic radiotherapy for prostate cancer: a sequential dose escalation pilot study. *Int. J. Radiat. Oncol. Biol. Phys.*, 78(1):50–57, 2010.

[60] G Groenendaal, M R Moman, J G Korporaal, P J Van Diest, M Van Vulpen, M E P Philippens, and U A Van der Heide. Validation of functional imaging with pathology for tumor delineation in the prostate. *Radiother. Oncol.*, 94:145–150, 2010.

[61] G Groenendaal, C A T van den Berg, J G Korporaal, M E P Philippens, P R Luijten, M van Vulpen, and U A van der Heide. Simultaneous mri diffusion and perfusion imaging for tumor delineation in prostate cancer patients. *Radiother. Oncol.*, 95(2):185–190, 2010.

[62] J G Korporaal, C A T van den Berg, G Groenendaal, M R Moman, M van Vulpen, and U A van der Heide. The use of probability maps to deal with the uncertainties in prostate cancer delineation. *Radiother. Oncol.*, 94(2):168–172, Feb 2010.

[63] S R Denmeade, X S Lin, and J T Isaacs. Role of programmed (apoptotic) cell death during the progression and therapy for prostate cancer. *Prostate*, 28(4):251–265, Apr 1996.

[64] M Bolla, L Collette, L Blank, P Warde, J B Dubois, R-O Mirimanoff, G Storme, J Bernier, A Kuten, C Sternberg, J Mattelaer, J L Torecilla, J R Pfeffer, C L Cutajar, A Zurlo, and M Pierart. Long-term results with immediate androgen suppression and external irradiation

in patients with locally advanced prostate cancer (an EORTC study): a phase III randomised trial. *The Lancet*, 360:103–108, 2002.

[65] C A Woodfield, G A Tung, D J Grand, J A Pezzullo, J T Machan, and J F Renzulli. Diffusion-weighted mri of peripheral zone prostate cancer: comparison of tumor apparent diffusion coefficient with gleason score and percentage of tumor on core biopsy. *Am. J. Roentgenol.*, 194(4):W316–W322, Apr 2010.

[66] T Tamada, T Sone, Y Jo, S Toshimitsu, T Yamashita, A Yamamoto, D Tanimoto, and K Ito. Apparent diffusion coefficient values in peripheral and transition zones of the prostate: comparison between normal and malignant prostatic tissues and correlation with histologic grade. *J. Magn. Reson. Imaging*, 28(3):720–726, 2008.

[67] K Yoshimitsu, K Kiyoshima, H Irie, T Tajima, Y Asayama, Hirakawa, K Ishigami, S Naito, and H Honda. Usefulness of apparent diffusion coefficient map in diagnosing prostate carcinoma: correlation with stepwise histopathology. *J. Magn. Reson. Imaging*, 27(1):132–139, 2008.

[68] M van Vulpen, C A T van den Berg, M R Moman, and U A van der Heide. Difficulties and potential of correlating local recurrences in prostate cancer with the delivered local dose. *Radiother. Oncol.*, 93(2):180–184, Nov 2009.

[69] T Franiel, L Ldemann, Taupitz, D Bhmer, and D D Beyersdorff. Mri before and after external beam intensity-modulated radiotherapy of patients with prostate cancer: the feasibility of monitoring of radiation-induced tissue changes using a dynamic contrast-enhanced inversion-prepared dual-contrast gradient echo sequence. *Radiother. Oncol.*, 93(2):241–245, Nov 2009.

[70] L E Kershaw, J P Logue, C E Hutchinson, N W Clarke, and D L Buckley. Late tissue effects following radiotherapy and neoadjuvant hormone therapy of the prostate measured with quantitative magnetic resonance imaging. *Radiother. Oncol.*, 88(1):127–134, Jul 2008.

[71] R W Van der Put, B W Raaymakers, E M Kerkhof, M Van Vulpen, and J J W Lagendijk. A novel method for comparing 3D target volume delineations in radiotherapy. *Phys. Med. Biol.*, 53(8):2149–2159, 2008.

[72] S Klein, U A van der Heide, I M Lips, M van Vulpen, M Staring, and J P W Pluim. Automatic segmentation of the prostate in 3d mr images by atlas matching using localized mutual information. *Med. Phys.*, 35(4):1407–1417, Apr 2008.

[73] M Goitein and A Niemierko. Intensity modulated therapy and inhomogeneous dose to the tumor: a note of caution. *Int. J. Radiat. Oncol. Biol. Phys.*, 36:519–522, 1996.

[74] *ClinicalTrials.gov: FLAME: investigate the benefit of a focal lesion ablative microboost in prostate cancer.* www.ClinicalTrials.gov.

[75] A Shukla-Dave, N Lee, H Stambuk, Y Wang, W Huang, H T Thaler, S G Patel, J P Shah, and J A Koutcher. Average arterial input function for quantitative dynamic contrast enhanced magnetic resonance imaging of neck nodal metastases. *BMC Med. Phys.*, 9:4, 2009.

[76] R Meng, S D Chang, E C Jones, S L Goldenberg, and P Kozlowski. Comparison between population average and experimentally measured arterial input function in predicting biopsy results in prostate cancer. *Acad. Radiol.*, 17(4):520–525, 2010.

[77] G J M Parker, C Roberts, A Macdonald, G A Buonaccorsi, S Cheung, D L Buckley, A Jackson, Y Watson, K Davies, and G C Jayson. Experimentally-derived functional form for a population-averaged high-temporal-resolution arterial input function for dynamic contrast-enhanced mri. *Magn. Reson. Med.*, 56(5):993–1000, 2006.

[78] Y Wang, W Huang, D M Panicek, L H Schwartz, and J A Koutcher. Feasibility of using limited-population-based arterial input function for pharmacokinetic modeling of osteosarcoma dynamic contrast-enhanced mri data. *Magn. Reson. Med.*, 59(5):1183–1189, 2008.

[79] M C Schabel and D L Parker. Uncertainty and bias in contrast concentration measurements using spoiled gradient echo pulse sequences. *Phys. Med. Biol.*, 53(9):2345–2373, 2008.

[80] C de Bazelaire, N M Rofsky, G Duhamel, J Zhang, M D Michaelson, D George, and D C Alsop. Combined t2* and t1 measurements for improved perfusion and permeability studies in high field using dynamic contrast enhancement. *Eur. Radiol.*, 16(9):2083–2091, 2006.

[81] H M Cheng and G A Wright. Rapid high-resolution T_1 mapping by variable flip angles: accurate and precise measurements in the presence of radiofrequency field inhomogeneity. *Magn. Reson. Med.*, 55:566–574, 2006.

[82] C Roberts, R Little, Y Watson, S Zhao, D L Buckley, and G J M Parker. The effect of blood inflow and b(1)-field inhomogeneity on measurement of the arterial input function in axial 3d spoiled gradient echo dynamic contrast-enhanced mri. *Magn. Reson. Med.*, 2011.

[83] H M Cheng. T1 measurement of flowing blood and arterial input function determination for quantitative 3d t1-weighted dce-mri. *J. Magn. Reson. Imaging*, 25(5):1073–1078, 2007.
[84] M K Ivancevic, I Zimine, X Montet, J Hyacinthe, F Lazeyras, D Foxall, and J Valle. Inflow effect correction in fast gradient-echo perfusion imaging. *Magn. Reson. Med.*, 50(5):885–891, 2003.
[85] P C Vos, T Hambrock, C A Hulsbergen-van de Kaa, J J Fütterer, J O Barentsz, and H J Huisman. Computerized analysis of prostate lesions in the peripheral zone using dynamic contrast enhanced MRI. *Med. Phys.*, 35(3):888–899, 2008.
[86] S Ozer, D L Langer, X Liu, M A Haider, T H van der Kwast, A J Evans, Y Yang, M N Wernick, and I S Yetik. Supervised and unsupervised methods for prostate cancer segmentation with multispectral mri. *Med. Phys.*, 37(4):1873–1883, 2010.
[87] X Liu, D L Langer, M A Haider, Y Yang, M N Wernick, and I S Yetik. Prostate cancer segmentation with simultaneous estimation of markov random field parameters and class. *TMI*, 28(6):906–915, 2009.
[88] D L Langer, T H van der Kwast, A J Evans, J Trachtenberg, B C Wilson, and M A Haider. Prostate cancer detection with multi-parametric mri: logistic regression analysis of quantitative t2, diffusion-weighted imaging, and dynamic contrast-enhanced mri. *J. Magn. Reson. Imaging*, 30(2):327–334, 2009.
[89] Y Artan, M A Haider, D L Langer, T H van der Kwast, A J Evans, Y Yang, M N Wernick, J Trachtenberg, and I S Yetik. Prostate cancer localization with multispectral mri using cost-sensitive support vector machines and conditional random fields. *IEEE Trans Image Process*, 19(9):2444–2455, 2010.
[90] B Turkbey, P A Pinto, H Mani, M Bernardo, Y Pang, Y L McKinney, K Khurana, G C Ravizzini, P S Albert, M J Merino, and P L Choyke. Prostate cancer: value of multiparametric mr imaging at 3 t for detection–histopathologic correlation. *Radiology*, 255(1):89–99, 2010.
[91] A Huisman, A Looijen, S M Van den Brink, and P J Van Diest. Creation of a fully digital pathology slide archive by high-volume tissue inside slide scanning. *Hum Pathol*, 41:751–757, 2010.
[92] S Webb and A E Nahum. A model for calculating tumour control probability in radiotherapy including the effects of inhomogeneous distributions of dose and clonogenic cell density. *Phys. Med. Biol.*, 38:653–666, 1993.
[93] L A Mucci, A Powolny, E Giovannucci, Z Liao, S A Kenfield, R Shen, M J Stampfer, and S K Clinton. Prospective study of prostate tumor angiogenesis and cancer-specific mortality in the health professionals follow-up study. *J. Clin. Oncol.*, 27(33):5627–5633, 2009.
[94] P Vaupel, F Kallinowski, and P Okunieff. Blood flow, oxygen and nutrient supply, and metabolic microenvironment of human tumors: a review. *Cancer Res.*, 49:6449–6465, 1989.
[95] D L Langer, T H van der Kwast, A J Evans, A Plotkin, J Trachtenberg, B C Wilson, and M A Haider. Prostate tissue composition and mr measurements: investigating the relationships between adc, t2, k(trans), v(e), and corresponding histologic features. *Radiology*, 255(2):485–494, 2010.
[96] H Dehnad, A J Nederveen, U A Van der Heide, R J A Van Moorselaar, P Hofman, and J J W Lagendijk. Clinical feasibility study for the use of implanted gold seeds in the prostate as reliable positioning markers during megavoltage irradiation. *Radiother. Oncol.*, 67(3):295–302, 2003.
[97] D Palma, E Vollans, K James, S Nakano, V Moiseenko, R Shaffer, M McKenzie, J Morris, and K Otto. Volumetric modulated arc therapy for delivery of prostate radiotherapy: comparison with intensity-modulated radiotherapy and three-dimensional conformal radiotherapy. *Int. J. Radiat. Oncol. Biol. Phys.*, 72(4):996–1001, 2008.
[98] K Otto. Volumetric modulated arc therapy: IMRT in a single gantry arc. *Med. Phys.*, 35(1):310–317, 2008.
[99] J C Stroom, H C de Boer, H Huizenga, and A G Visser. Inclusion of geometrical uncertainties in radiotherapy treatment planning by means of coverage probability. *Int. J. Radiat. Oncol. Biol. Phys.*, 43(4):905–919, 1999.
[100] M van Herk. Errors and margins in radiotherapy. *Semin. Radiat. Oncol.*, 14(1):52–64, 2004.
[101] H C J de Boer, M J H van Os, P P Jansen, and B J M Heijmen. Application of the no action level (nal) protocol to correct for prostate motion based on electronic portal imaging of implanted markers. *Int. J. Radiat. Oncol. Biol. Phys.*, 61(4):969–983, 2005.

[102] D Ltourneau, A A Martinez, D Lockman, D Yan, C Vargas, G Ivaldi, and J Wong. Assessment of residual error for online cone-beam ct-guided treatment of prostate cancer patients. *Int. J. Radiat. Oncol. Biol. Phys.*, 62(4):1239–1246, 2005.

[103] P A Kupelian, K M Langen, O A Zeidan, S L Meeks, T R Willoughby, T H Wagner, S Jeswani, K J Ruchala, J Haimerl, and G H Olivera. Daily variations in delivered doses in patients treated with radiotherapy for localized prostate cancer. *Int. J. Radiat. Oncol. Biol. Phys.*, 66(3):876–882, Nov 2006.

[104] D P Dearnaley, M R Sydes, J D Graham, E G Aird, D Bottomley, R A Cowan, R A Huddart, C C Jose, J H Matthews, J Millar, A R Moore, R C Morgan, J Martin Russell, C D Scrase, R J Stephens, I Syndikus, M K B Parmar, and R. T01 collaborators. Escalated-dose versus standard-dose conformal radiotherapy in prostate cancer: first results from the mrc rt01 randomised controlled trial. *Lancet Oncol.*, 8(6):475–487, 2007.

[105] P Gibbs, M D Pickles, and L W Turnbull. Repeatability of echo-planar-based diffusion measurements of the human prostate at 3 t. *Magn. Res. Imaging*, 25(10):1423–1429, 2007.

[106] L E Kershaw, C E Hutchinson, and D L Buckley. Benign prostatic hyperplasia: evaluation of t1, t2, and microvascular characteristics with t1-weighted dynamic contrast-enhanced mri. *J. Magn. Reson. Imaging*, 29(3):641–648, 2009.

[107] J G Korporaal, C A T van den Berg, G Groenendaal, M R Moman, M van Vulpen, and U A van der Heide. The use of probability maps to deal with the uncertainties in prostate cancer delineation. *Radiother. Oncol.*, 94(2):168–172, 2010.

[108] D Le Bihan, C Poupon, A Amadon, and F Lethimonnier. Artifacts and pitfalls in diffusion mri. *J. Magn. Reson. Imaging*, 24(3):478–488, 2006.

[109] J G Korporaal, C A T Van den Berg, M. J. P Van Osch, M Van Vulpen, and U A Van der Heide. Uncertainties in the arterial input function (aif) in dynamic contrast-enhanced (dce) imaging of the pelvis: when to use a population-averaged or an exam-specific aif?

[110] E Akbudak and T E Conturo. Arterial input functions from MR phase imaging. *Magn. Reson. Med.*, 36(6):809–815, 1996.

[111] E Akbudak, R E Norberg, and T E Conturo. Contrast-agent phase effects: an experimental system for analysis of susceptibility, concentration, and bolus input function kinetics. *Magn. Reson. Med.*, 38(6):990–1002, 1997.

[112] J G Korporaal, C A T Van den Berg, M. J. P Van Osch, G Groenendaal, M Van Vulpen, and U A Van der Heide. Phase-based arterial input function measurements in the femoral arteries for quantification of dynamic contrast-enhanced (dce) mri and comparison with dce-ct. *Magn. Reson. Med.*, in press, 2011.

[113] A E Nahum, B Movsas, E M Horwitz, C C Stobbe, and J D Chapman. Incorporating clinical measurements of hypoxia into tumor local control modeling of prostate cancer: implications for the α/β ratio. *Int. J. Radiat. Oncol. Biol. Phys.*, 57:391–401, 2003.

Publications

Papers

Validation of functional imaging with pathology for tumor delineation in the prostate G. Groenendaal, M.R. Moman, J.G. Korporaal, P.J. van Diest, M. van Vulpen, M.E.P. Philippens and U.A. van der Heide *Radiotherapy and Oncology 94:145-150, 2010*

The use of probability maps to deal with the uncertainties in prostate cancer delineation J.G. Korporaal, C.A.T. van den Berg, G. Groenendaal, M.R. Moman, M. van Vulpen and U.A. van der Heide *Radiotherapy and Oncology 94:168-172, 2010*

Simultaneous MRI diffusion and perfusion imaging for tumor delineation in prostate cancer patients G. Groenendaal, C.A.T. van den Berg, J.G. Korporaal, M.E.P. Philippens, P.R. Luijten, M. van Vulpen and U.A. van der Heide *Radiotherapy and Oncology 95:185-190, 2010*

Dynamic Contrast-enhanced CT for Prostate Cancer: Relationship between Image Noise, Voxel Size, and Repeatability J.G. Korporaal, C.A.T. van den Berg, C.R.L.P.N. Jeukens, G. Groenendaal, M.R. Moman, P.R. Luijten, M. van Vulpen and U.A. van der Heide *Radiology 256:976-984, 2010*

Functional MRI for tumor delineation in prostate radiation therapy U.A. van der Heide, J.G. Korporaal, G. Groenendaal, S. Franken and M. van Vulpen *Imaging in Medicine 2011 3:219-231*

Phase-based arterial input function measurements in the femoral arteries for quantification of dynamic contrast-enhanced (DCE) MRI and comparison with DCE-CT J.G. korporaal, C.A.T. van den Berg, M.J.P. van Osch, G. Groenendaal, M. van Vulpen and U.A. van der Heide *Magnetic in Medicine 2011; in press: DOI 10.1002/mrm.22905*

The effect of hormonal therapy on conspicuity of prostate cancer: implications for focal boosting radiotherapy G. Groenendaal, M. van Vulpen, S.R. Pereboom, D. Poelma-Tap, J.G. Korporaal, E. Monninkhof and U.A. van der Heide *submitted*

Pathological validation of a Model based on Diffusion-Weighted imaging and Dynamic contrast-enhanced MRI for tumor delineation in the prostate peripheral zone G. Groenendaal, A. Borren, M.R. Moman, P.J. van Diest, M.E.P. Philippens, M. van Vulpen and U.A. van der Heide *International Journal of Radiation Oncology Biology Physics, accepted for publication*

Histological properties of prostate tumors detected and non-detected with Magnetic Resonance Imaging A. Borren*, G. Groenendaal*, M.R. Moman, A. Boeken-Kruger, P.J. van Diest, M. van Vulpen, M.E.P. Philippens and U.A .van der Heide *submitted*

Proceedings and abstracts

Simultaneous diffusion and perfusion imaging provides complementary functional data that can be used in the pre- and post therapeutic disease management in prostate cancer patients - [oral]
G. Groenendaal, C.A.T. van den Berg, E.M.A. Roeloffzen, J.G. Korporaal, P.R. Luijten, M van Vulpen, U.A. van der Heide *First Benelux In Vivo MR Methods Symposium, Berg en Dal, the Netherlands*

Simultaneous MRI diffusion and perfusion imaging for tumor delineation in prostate cancer patients - [oral]
G. Groenendaal, C.A.T. van den Berg, E.M.A. Roeloffzen, J.G. Korporaal, M. Philippens, P.R. Luijten, M. van Vulpen, U.A. van der Heide *ESTRO 2008, 27th Annual Meeting, Göteborg, Sweden*

Simultaneous diffusion and perfusion imaging provides complementary functional data that can be used in the pre- and post therapeutic disease management in prostate cancer patients - [poster]
G. Groenendaal, C.A.T. van den Berg, E.M.A. Roeloffzen, J.G. Korporaal, P.R. Luijten, M van Vulpen, U.A. van der Heide *ISMRM 16th Annual Scientific Meeting and Exhibition 2008, Toronto, Canada*

Validation of functional imaging with pathology for tumor delineation in the prostate - [oral]
G. Groenendaal, M.R. Moman, J.G. Korporaal, P.J. van Diest, M. van Vulpen, E.P. Philippens, U.A. van der Heide *ESTRO 2009, 10th Biennial Meeting, Maastricht, the Netherlands*

Magnetic resonance imaging for prostate cancer: From diagnostics to therapeutic decisions - [oral] G. Groenendaal, M.R. Moman, J.G. Korporaal, P. van Diest , M van Vulpen, M.E.P. Philippens, U.A. van der Heide *ISMRM 18th Annual Scientific Meeting and Exhibition 2010, Stockholm, Sweden*

The role of medication in the interpretation of functional MR images of the prostate - [oral]
G. Groenendaal, S. Pereboom, Poelma-Tap, D., Korporaal, J.G., M van Vulpen, U.A. Van der Heide *ESTRO 2010, 29th Annual Meeting, Barcelona, Spain*

Invited presentations

Functional MR imaging for delineation and characterization of prostate tumors
ESTRO 2011, 11th Biennial Meeting, London, United Kingdom

Dankwoord

De afgelopen 4 jaar zijn voorbij gevlogen. Ik heb een leuke tijd gehad in het UMC en hiervoor wil ik al mijn collega's graag bedanken. Hiernaast zou ik nog graag een aantal mensen persoonlijk willen bedanken.

Jan Lagendijk, ik vond het erg fijn om op jouw afdeling te mogen werken. Doordat je het houden van gezamelijke koffiepauzes erg stimuleert, heerst er een goede en informele sfeer, waarbij iedereen altijd makkelijk te benaderen is. Ik ben erg blij met het vertrouwen dat je in me hebt gesteld.

Uulke, bedankt dat je altijd ontzetted betrokken bent geweest bij mijn werk. Je bent erg kritisch. Hier heb ik aan moeten wennen, maar het heeft er wel voor gezorgd, dat ik meer uit mezelf heb weten te halen, dan ik zelf dacht dat er in zat. Ik heb veel van je geleerd, vakinhoudelijk, maar ook daarbuiten. Ik kon altijd bij je terecht. De prostaat is maar een klein orgaan, maar alles bij elkaar hebben we hier uren over zitten praten en steeds weer ging ik met nieuwe inzichten naar buiten.

Marco, samen met Uulke heb je de prostaatgroep opgezet. Jouw enthousiasme was hierin altijd een belangrijke factor. Dit enthousiasme en jouw positieve commentaar op mijn werk hebben bij mij altijd heel motiverend gewerkt. Bovendien zorgde jij er steeds voor, dat we het klinische nut niet uit het oog verloren. Dit heeft zeker een positief effect op mijn artikelen gehad.

Mariëlle, ook jij was een belangrijke factor in de prostaatgroep. Door jouw uitgebreide kennis van zowel MRI als histopathologie, heb je veel kunnen bijdragen aan mijn werk.

Alexis, toen jij jezelf een aantal jaren geleden bij een borrel aanbood als mijn coach had ik niet verwacht dat ik daar zo blij mee zou zijn. Bedankt voor de gezelligheid, de vele dropjes, het redden van mijn data, maar vooral voor de vele fietsmomenten.

Alexis, Gijs, Ric, Rob en Kees, bedankt voor alle PC- en programmeerhulp.

De medewerkers van de **urologie- en pathologieafdeling** bedankt voor alle medewerking met de prostaat MRI-histopathologie vergelijkingstudie.

De afgelopen jaren waren met name heel erg leuk door alle dingen, die ik heb gedaan met collega AIO's, klifio's en studenten. Dan denk ik aan de vele etentjes en congressen, maar ook aan het fietsen, zwemmen, de kookworkshops, het klimmen, onze filmavonden en het vliegeren. Dank jullie wel, hiervoor. Het was super!

Met een aantal collega's heb ik nog iets nauwer samengewerkt. Allereerst natuurlijk met prostaatbroertje **Jan**. Jan, wij zijn tegelijk begonnen als AIO's bij Uulke. Ik vond het erg prettig het hele traject met jou te doorlopen. Vanaf ons eerste artikel tot en met de promotiestress en het bedenken van wat we hierna zouden gaan doen. Ik wens je het allerbeste voor de rest van je carriere.

Maaike, met jou heb ik veel samengewerkt aan het begin van de pathologiestudie. Ik heb het leuk gevonden hier samen mee bezig te zijn. Jij hebt hier veel werk voor verzet, waar we nog altijd de vruchten van plukken.

Alie, jij kwam later bij het histopathologieproject en hebt je onder andere veel bezig gehouden met kleuringen. Jij en Mariëlle hebben me veel over pathologie geleerd. Het was fijn om met je samen te werken.

Susanne Pereboom, als student heb jij een belangrijke bijdrage geleverd aan hoofdstuk 3 van dit proefschrift. Jij hebt veel van de data verzameld, die de basis vormt van dit hoofdstuk. Ook **Davey Poelma-Tap** wil ik bedanken voor het bijdragen aan het verzamelen van data.

Richard, jou zou ik willen bedanken voor de hulp bij hoofdstuk 4. Je hebt me erg geholpen met Mathematica en de door jou geschreven software.

Evelyn Monninkhof zou ik graag willen bedanken voor de bijdrages aan de statistiek. Evelyn, je was altijd bereid om mij te helpen en mee te denken over mijn werk. Hier heb ik dankbaar gebruik van gemaakt.

Michiel, bedankt dat je me overtuigd hebt om naar Utrecht te gaan!

Yaël, ik vind het erg leuk dat ik je na jaren weer in de bus tegenkwam. Via jou leerde ik ook **Linda en Sophie** kennen. Ik heb de afgelopen jaren erg genoten van onze wekelijke lunches en onze sportieve en artistieke activiteiten. Zo af en toe heb ik deze activiteiten gebruikt om mijn frustraties te spuien, maar ze waren vooral erg gezellig. Bedankt hiervoor!

Simon, zonder jou was dit proefschrift er niet geweest :). Ik ben erg blij met al onze gesprekken, die vaak gaan over de wetenschap, maar nog vaker over helemaal niks.

Pap, mam, Willemijn, Noortje en Nelis, bedankt dat het jullie is gelukt om de laatste jaren zoveel interesse voor de prostaat op te brengen. Maar vooral bedankt dat jullie er altijd voor me zijn.

Bart, met jouw relativerende houding en betrokkenheid heb je me ontzettend geholpen. Mede dankzij jou heb ik een relaxed promotietraject gehad. Nog altijd ben ik blij, dat het toen in januari zo hard vroor.

Greetje

Curriculum Vitae

Greetje Groenendaal was born on October 19, 1981, in Son en Breugel. After finishing her secondary education in 2000 at the Eckart College in Eindhoven, she started the study psychology at the Radboud University Nijmegen. After the first year, she changed to study Biomedical Engineering at the Eindhoven University of Technology. During her studies she carried out an internship at the University of Canterbury, New Zealand, where she investigated the blood flow in the circle of Willis. She performed her Master's project on rheumatoid arthritis at N.V. Organon, Oss. She obtained her Master of Science degree in 2007, after which she started a PhD project at the radiotherapy department of the University Medical Center Utrecht. This resulted in this dissertation entitled "Functional MR Imaging for focal radiotherapy of prostate cancer". In August 2011, she started on a post-doc project at the NKI-AVL in Amsterdam.